

Energy & Environmental Science

Accepted Manuscript



This is an *Accepted Manuscript*, which has been through the Royal Society of Chemistry peer review process and has been accepted for publication.

Accepted Manuscripts are published online shortly after acceptance, before technical editing, formatting and proof reading. Using this free service, authors can make their results available to the community, in citable form, before we publish the edited article. We will replace this *Accepted Manuscript* with the edited and formatted *Advance Article* as soon as it is available.

You can find more information about *Accepted Manuscripts* in the [Information for Authors](#).

Please note that technical editing may introduce minor changes to the text and/or graphics, which may alter content. The journal's standard [Terms & Conditions](#) and the [Ethical guidelines](#) still apply. In no event shall the Royal Society of Chemistry be held responsible for any errors or omissions in this *Accepted Manuscript* or any consequences arising from the use of any information it contains.

A Review of Cathode Materials and Structures for Rechargeable Lithium-Air Batteries

Zhong Ma¹, Xianxia Yuan^{1,*}, Lin Li¹, Zi-Feng Ma¹, David P. Wilkinson², Lei Zhang², Jiujuun Zhang^{2,*}

¹ Department of Chemical Engineering, Shanghai Jiao Tong University, Shanghai, 200240, China

² Department of Chemical and Biochemical Engineering, University of British Columbia, Vancouver, Canada

Abstract: Rechargeable lithium air (Li-air) batteries, especially the non-aqueous type, are considered the most promising energy storage and conversion device candidates for use in future electric vehicle applications due to their ultrahigh energy density. The air cathode has been identified as a key factor affecting the overall performance of Li-air batteries. The current low level performance of air cathodes is the major challenge hindering commercial applications of Li-air batteries. In the past decade, a great many cathode materials, structures and fabrication processes have been developed and investigated with the goal of enhancing cathode performance. This paper reviews, the role of the cathode in non-aqueous Li-air batteries including the cathode reaction mechanisms and the properties and morphologies of cathode materials, followed by approaches to optimize cathode performance. The most recently published global progress and the main achievements in the field of Li-air batteries are also systematically and critically reviewed in terms of cathode materials, structures and fabrication processes, with the objective of providing some state-of-the-art information. Technical challenges are analyzed, and insights into future research directions for overcoming these development challenges of rechargeable non-aqueous Li-air battery cathodes are also identified in this review paper.

*Corresponding author: Tel: 86-21-54742827; Fax: 86-21-54741297; Email: yuanxx@sjtu.edu.cn (X. Yuan);
jiujuun.zhang@nrc.gc.ca (J. Zhang)

Keywords: Non-aqueous lithium air batteries; Cathode materials/structures/fabrications; Oxygen reduction/evolution reactions

1 Introduction

With increased demand from mobile (wireless) energy applications, the global effort to improve the lifetime, energy and power densities, and energy efficiency of electrochemical energy storage and conversion technologies, such as batteries, fuel cells, and supercapacitors, has become dramatically more extensive in recent years.¹⁻⁶ Among these electrochemical energy devices, rechargeable lithium air batteries (Li-air batteries) are considered one of the most attractive energy storage and conversion devices due to their extremely high potential energy density as discussed below.⁷⁻¹⁰

Li-air batteries, sometimes called Li-O₂ batteries, realize the reversible transport between chemical and electric energy by electrochemical reactions of lithium at the anode and air (O₂) at the cathode, respectively.^{4,7,9,11-16} As early as 1976, Littauer and Tsai^{17,18} proposed the concept of Li-air chemistry in an aqueous system. After that, Abraham et al.^{19,20} reported in 1996 the first study on a non-aqueous Li-air battery system based on an organic polymer electrolyte. However, Li-air batteries failed to attract significant attention during the next decade because of the technical difficulties involved in achieving high amounts of energy density and extended cycle-life. Li-air batteries recaptured scientific interest in the last ten years owing to its ultrahigh potential specific energy densities from 1000 to 2000 Wh kg⁻¹ depending on the types of electrolyte, membrane, and cathode design and materials used.²¹ In general, the specific potential energy density of a Li-air battery is several times higher than that of state-of-the-art Li-ion battery technology^{7,22-26} and can even match that of 1700 Wh kg⁻¹ for a gasoline energy system (Fig. 1).^{23,27-29} Therefore, Li-air batteries are considered to

be the most promising of rechargeable battery technology,^{30,31} which may be capable of providing enough energy storage capability for electric vehicles to drive more than 500 miles (per charge), which is comparable to the range of gasoline vehicles.²³

In respect to the different types of Li-air batteries, there are four major architected systems: 1) aprotic,^{19,32-36} 2) aqueous,³⁷⁻⁵⁴ 3) all-solid-state⁵⁵⁻⁶⁵ and 4) hybrid⁶⁶⁻⁸² systems, each classified by the electrolyte used, as shown in Fig. 2. Among them, the non-aqueous system has attracted considerably more attention due to its potentially higher energy density and rechargeability.^{21,83} Several representative research groups on non-aqueous Li-air batteries include: a) the USA Army Research Laboratory who are focussing on the discharge mechanism, electrode materials and electrolyte composition;^{11,84-93} b) the University of St. Andrews (UK) who are focussing on the catalyst, electrolyte, charge-discharge reversibility and cycling-ability,^{7,13,34,83,94-104} and, c) Massachusetts Institute of Technology (MIT) (USA) who are focussing on development of catalysts to enhance both the oxygen reduction reaction (ORR) and the oxygen evolution reaction (OER).^{15,105-111} Recently, several exciting advances in respect to non-aqueous Li-air batteries have been made and widely communicated to the worldwide research and development community. For example:

a) Peng et al.⁹⁷ prepared a reversible and high-rate Li-air battery using nanoporous gold electrode (NPG) as the cathode and dimethyl sulfoxide (DMSO) as the electrolyte, which were able to achieve an capacity retention of 95% after 100 cycles.

b) Jung et al.¹¹² fabricated a Lithium/tetraethylene glycol dimethyl ether (TEGDME)-LiCF₃SO₃/O₂ battery with enhanced performance. Their battery was operated under a capacity of 5000 mAh g_{carbon}⁻¹ for 30 cycles with a sustained discharge voltage of 2.7 V at a current density of 500 mA g_{carbon}⁻¹. Furthermore, their battery could also operate efficiently with limited charge-discharge polarization even at high current density of 3000 mA g_{carbon}⁻¹.

c) Lu et al.¹¹³ reduced the charge overpotential to 0.2 V by using nanoscale components in the cathode which was assembled using atomic layer deposition of palladium nanoparticles on a carbon surface with an alumina coating for passivation of carbon defect sites (Fig. 3).

d) Lim et al.¹¹⁴ employed LiI as a soluble catalyst, the resulting battery exhibited a charge overpotential of 0.25 V and ran stably for more than 900 cycles with a discharge depth of 1000 mAh g_{carbon}⁻¹ at a current density of 2000 mA g_{carbon}⁻¹.

e) Thotiyl et al.¹¹⁵ found that TiC could exhibit a better reversible formation/decomposition of Li₂O₂ with more than 98% capacity retention after 100 cycles, owing to the prevention of side reactions from electrolyte decomposition and electrode degradation with carbon materials.

Despite the above achievements, Li-air battery technology is still at an early stage of development at this time. Although the theoretical energy density of Li-air batteries is impressively high, in practice, there still remain many challenges to realize this advantage of high energy performance. For example, the achieved capacity and energy density of Li-air batteries are still relatively low. In addition, other challenges such as a lack of high-rate dischargability, insufficient capacity sustainability and low round-trip efficiency,^{7,24,116-119} have also been observed, all of which hinder practical applications of Li-air battery technology. Among various issues affecting Li-air battery performance generally, the low level of performance of the air cathode has been identified as the dominating factor.¹²⁰ At the same time, improvements to any or all of the Li anode,¹²¹⁻¹³² operating atmosphere,¹³³⁻¹⁴⁵ binder,^{146,147} solvents,¹⁴⁸⁻¹⁵⁵ and lithium salts,¹⁵⁶⁻¹⁶⁶ would also make meaningful contributions to enhanced overall battery performance.

The cathode oxygen reduction reaction (ORR) in a Li-air battery is much slower than that of the anode Li oxidation reaction (the cathode reaction overpotential is much higher

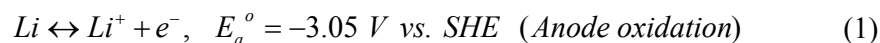
than that of the anode reaction, as shown in Fig. 4),⁹¹ thus dominating the overall rate of charge/discharge of the battery.^{167,168} As a result, the cathode in Li-air batteries has captured much more attention than the anode, resulting in numerous worldwide research and development projects. Great progress has been made in recent years even though no significant breakthroughs have yet been achieved.¹⁶⁹ To facilitate the continuing effort on this important subject, this article will review, identify and discuss:

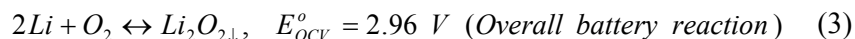
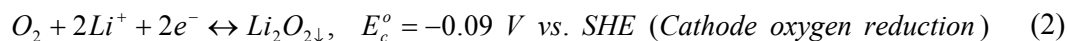
- a) Working principle of the cathode in a non-aqueous Li-air battery including the cathode reaction mechanisms;
- b) Nature and morphology of the cathode reaction products and their effect on battery performance;
- c) Approaches to design and fabricate a high-performing cathode using advanced materials; and
- d) Pending challenges and future research directions to overcome the technical hurdles.

2 Overview of non-aqueous Li-air batteries and their associated cathodes

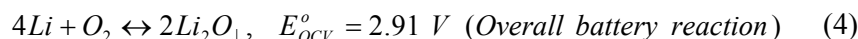
2.1 Electrochemical reactions in non-aqueous Li-air batteries

In general, the performance of a Li-air battery is greatly affected by the actual products generated at the cathode during charge-discharge processes. The major discharge product at the cathode is lithium peroxide (Li_2O_2) with a small portion of lithium oxide (Li_2O). The discharge reactions of Li-air batteries with Li_2O_2 as the product can be described as Equations (1), (2) and (3) in a non-aqueous electrolyte, respectively:^{21,170-175}





where E_a° , E_c° and E_{OCV}° are the thermodynamic anode potential, cathode potential and Li-air battery open circuit voltage (OCV) at standard conditions (25 °C, 1.0 atm) if Li_2O_2 is the product, respectively. For discharge product of Li_2O , the overall reaction can be expressed as Reaction (4):



where E_{OCV}° is the thermodynamic open circuit voltage (OCV) of Li-air battery at standard conditions (25 °C, 1.0 atm) if Li_2O is the product. It seems that Reaction (4) is not desirable because it is not very reversible, being not be fully rechargeable back to Li and O_2 .^{102,116,176} Therefore, Li_2O_2 is considered the ideal discharge product at the cathode. However, this half-cell reaction (Reaction (2)) is actually not a simple reaction, it contains several elemental reactions which will be discussed later. For example, some researchers found an oxygen-rich superoxide-like component in Li_2O_2 ¹⁷⁷⁻¹⁸¹ which exhibited a disproportionation to Li_2O_2 during the discharge process and could give a much lower overpotential during the charge process than Li_2O_2 .

2.2 Theoretical specific energy density of Li-air batteries

Regarding the theoretical specific energy density of Li-air batteries without considering the electrode structure/mass, electrolyte/membrane, current collectors and other accessories, thereby meaning considering only the weight of reactants, there are several expressions as follows:

- (1) Theoretical specific electrochemical capacity of Lithium (C_{Li}^W , Ah kg⁻¹). C_{Li}^W is used

to express the amount of electrons which can be released when one kilogram of Li metal is oxidized according to Reaction (1) (for anode). For theoretical specific electrochemical capacity, it can be normally calculated using Equation (5):

$$C_{Li}^w = \frac{n_{Li} F}{w_{Li}} \quad (5)$$

where n_{Li} is the electron number per Li atom when it is oxidized ($n_{Li}=1$), F is the Faraday's constant ($96487 \text{ As mol}^{-1}$ or $26.802 \text{ Ah mol}^{-1}$), and w_{Li} is the weight of one mole of Li metal ($6.941 \times 10^{-3} \text{ kg mol}^{-1}$). The obtained theoretical specific electrochemical capacity for Li metal is 3861 Ah kg^{-1} .

(2) Theoretical specific electrochemical capacity of oxygen ($C_{O_2}^w$, Ah kg^{-1}). $C_{O_2}^w$ is used to express the amount of electrons which can be adsorbed when one kilogram of O_2 is reduced according to Reaction (2) (for Cathode). For theoretical specific electrochemical capacity of O_2 , it can be calculated using Equation (6):

$$C_{O_2}^w = \frac{n_{O_2} F}{w_{O_2}} \quad (6)$$

where n_{O_2} is the electron number per O_2 molecule when it is reduced ($n_{O_2}=2$), F has the same meaning as in Equation (5), and w_{O_2} is the weight of one mole of O_2 ($3.2 \times 10^{-2} \text{ kg mol}^{-1}$). The obtained theoretical specific electrochemical capacity for O_2 is 1675 Ah kg^{-1} .

(3) Theoretical specific energy density of Lithium, O_2 , and a Li-air battery (E_{Li}^w , $E_{O_2}^w$, and E_{L-air}^w , Wh kg^{-1}). Regarding the theoretical specific energy density of Lithium, it is only meaningful and calculated when it is combined with a cathode reaction such as Reaction (2). This means that when using different cathode reactions for Li batteries, the theoretical specific energy density of Lithium are different. When Reactions (1) and (2) are combined to

form a battery with a theoretical open circuit voltage ($E_{OCV}^{\circ} = 2.96 \text{ V}$), the theoretical specific energy density of Lithium can be expressed as Equation (7):

$$E_{Li}^W = C_{Li}^W E_{OCV}^{\circ} = \frac{n_{Li} F}{w_{Li}} E_{OCV}^{\circ} \quad (7)$$

Using Equation (7), the theoretical specific energy density of Lithium can be calculated to be 11776 Wh kg^{-1} when O_2 is used as the cathode reactant. In a similar way, the theoretical

specific energy density of O_2 ($E_{O_2}^W = C_{O_2}^W E_{OCV}^{\circ} = \frac{n_{O_2} F}{w_{O_2}} E_{OCV}^{\circ}$) when Li is used as the anode reactant can be calculated to be 4958 Wh kg^{-1} .

The theoretical specific energy density of a Li-air battery (E_{Li-air}^W) can be calculated with the theoretical open circuit voltage of Reaction (3) using Equation (8):

$$E_{Li-air}^W = \frac{|n F E_{OCV}^{\circ}|}{2w_{Li} + w_{O_2}} \quad (8)$$

Where n is the battery reaction electron number ($n=2$). The calculated theoretical specific energy density for a Li-air battery is 3458 Wh kg^{-1} . Sometimes, due to the O_2 coming from outside the battery device, the battery's theoretical specific energy density excluding O_2 mass ($w_{O_2} = 0$ in Equation (8)) can be calculated to be 11428 Wh kg^{-1} which is much higher than the majority of metal-air batteries. Note that the theoretical specific energies calculated above are for non-aqueous electrolyte solution. If the Li-air battery uses an aqueous electrolyte solution, the resulting electrode reactions and products are different and likewise the theoretical specific energy densities of non-aqueous Li-air batteries have different values from those of aqueous ones. Furthermore, the other expression for energy density is to use volume of the reactant/device and the unit of the energy density would be Wh L^{-1} rather than Wh kg^{-1} . Both units can be converted if the densities of reactant/device masses (kg L^{-1}) are

known. It should be noted that Equation (8) only considers the masses of reactants, but does not count the contribution from the actual device's masses including electrode (cathode) reaction layer, electrolyte/membrane, current collector and other accessories. When one considers these masses, the specific energy density of a Li-air battery is much less than the values mentioned above.²¹

(4) Practical specific energy density ($E_{Li-air}^{W, P}$, Wh kg⁻¹). The value of $E_{Li-air}^{W, P}$ can be estimated by counting the masses of reactants, device, discharging overpotentials, and voltage drop caused by the battery's internal resistance. The value of $E_{Li-air}^{W, P}$ is normally lower than the theoretical E_{Li-air}^W . The expression may be written as Equation (9):

$$E_{Li-air}^{W, P} = \frac{|nFE_{Cell}|}{w_{Cell}} = \frac{|nF(E_{OCV}^{\circ} - \eta_a - \eta_c - iR)|}{w_a + w_c + w_{cc} + w_{el/m} + w_{ac}} \quad (9)$$

Where E_{cell} is the battery cell voltage during discharge, w_{Cell} , w_a , w_c , w_{cc} , $w_{el/m}$ and w_{ac} are the weight of the battery, anode, cathode, current collector, electrolyte/membrane, and accessory, respectively, η_a , η_c , i and R are the anode overpotential, cathode overpotential, load current, and battery internal resistance, respectively. It can be seen that in order to improve the Li-air battery's energy density, one has to accelerate the battery's reaction kinetics to reduce the anode and cathode overpotentials, decrease the voltage loss induced by the internal resistance, as well as decrease the battery weight by reducing the material weights of anode, cathode, electrolyte/membrane, current collector, and accessory. Regarding the electrode overpotentials, cathode overpotential is the dominating one because the cathode oxygen reduction reaction is much slower than anode lithium oxidation. Therefore, cathode research is a major focus of Li-air battery development.

2.3 Li-air battery cathode reaction mechanisms and the effect of possible side reactions on battery performance

2.3.1 Cathode reaction mechanism

As mentioned above, the cathode reaction in non-aqueous Li-air battery can produce a mixture of Li oxides although lithium peroxide, Li_2O_2 , is considered to be the desired one. In the specific formation and decomposition of Li_2O_2 during charge-discharge processes, several different mechanisms have been proposed in the literature based on theoretical calculation as well as experiments.^{36,99,111,173,182-188} Two major discharge reaction mechanisms for the ORR on cathode material surface have been proposed as follows:

Discharge reaction Mechanism I:

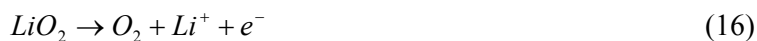


Discharge reaction Mechanism II:



For the charge process, there are two major reaction mechanisms:

Charge reaction Mechanism I:



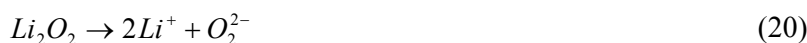
Charge reaction Mechanism II:



There are also some other proposals for the reaction mechanism in the literature. For example, Hummelshøj et al.¹⁷² proposed the discharging reactions at the cathode might involve Reactions (18) and (19) where “*” denotes a surface site on Li_2O_2 where the growth proceeds:



For the charging reaction on a pyrochlore catalyst surface, Oh et al.¹⁸⁹ believed the cathode mechanism could be:



In addition, Laoire et al.¹⁷³ showed the reduction and subsequent oxidation of O_2 in acetonitrile-based electrolytes was strongly influenced by the cation type of the conducting salts used.

In fact, no commonly accepted consensus on the cathode mechanism for non-aqueous Li-air batteries has been achieved to date. The reported mechanisms are mainly acquired by theoretical conjecture or calculation, and most of the characterizations used to study the mechanism are ex-situ, which can not reveal the exact reaction paths in the charge-discharge process. Therefore, more in-situ characterizing technologies should be well developed in the future to clarify the exact cathode mechanisms for non-aqueous Li-air batteries.

2.3.2 Effect of possible side reactions on battery performance

It is worthwhile to note that for non-aqueous Li-air batteries, organic carbonate-based

electrolytes such as LiPF_6 in propylene carbonate (PC) or ethylene carbonate (EC) and (dimethyl carbonate) DMC (1:1, v/v) have been widely used.^{19,190} In these cases, the electrolyte decomposition between oxygen and electrolyte forming irreversible organic and inorganic carbonate species (i.e. lithium alkylcarbonates and Li_2CO_3) during discharge, rather than the desired Li_2O_2 , could limit the cycle life of the battery. More specifically, the Li_2CO_3 produced at the cathode could be regarded as a “destroyer” of the Li-air battery.^{191,192} Support for this view comes from extensive research which has revealed the high polarization in charge-discharge process of Li-air batteries can be attributed to the formation and decomposition of Li_2CO_3 rather than Li_2O_2 , and the fast degradation of battery capacity with cycles can also be caused by the generation of Li_2CO_3 , since the decomposition potential of Li_2CO_3 (~4.2 V) is obviously higher than both those of Li_2O and Li_2O_2 (~3.3-3.4 V) as shown in Fig. 5.¹⁹³

In order to more fully understand the cathode processes in non-aqueous Li-air batteries and their effect on the overall battery performance, a variety of in-situ and/or ex-situ characterization techniques have been widely employed in recent years. These techniques have included: X-ray Diffraction (XRD),^{189,194-197} Raman,^{19,94,198,199} Differential Electrochemical Mass Spectrometry (DEMS),^{83,191} Scanning Electron Microscope (SEM),^{189,194,196} Transmission Electron Microscope (TEM),²⁰⁰ X-ray Photoelectron Spectroscopy (XPS),²⁰¹ Fourier Transform Infrared Spectroscopy (FTIR),²⁰²⁻²⁰⁵, Nuclear Magnetic Resonance (NMR),²⁰⁶ and Atomic Force Microscopy (AFM).^{60,207-209} The results revealed the cathode products are closely related to the type of electrolytes used, including the solvents and lithium salts as well as the carbon materials and other components from the cathode reaction layer.

(1) Effect of the type of solvent on battery performance

The solvents used in the electrolytes for non-aqueous Li-air batteries can be classified into carbonates, ethers, sulfones, amides and ionic liquids as listed in Table 1 along with their physical properties. In general, the solvent with low vapor pressure has low vaporization during the cycling of a battery. The solvents with high donor number (DN) such as DMSO could help the stability of intermediate discharge product such as LiO_2 while those with low DN such as TEGDME could promote the formation of Li_2O_2 and Li_2O . Generally, light solvents are preferred for Li-air batteries due to the promotion of energy density for the whole battery device.

As mentioned above, carbonate based solvents, mainly including PC,^{93,98,210,211} EC,^{33,212} DMC,²¹³ ethyl methyl carbonate (EMC)²¹⁴ and diethyl carbonate (DEC),^{84,215,216} were the earliest solvents used for non-aqueous Li-air battery.¹⁵⁴ In general, the solvents are mixtures of several single carbonate solvents with specific proportions to achieve good electrochemical performance.²¹⁷ However, this kind of solvent is not stable to the superoxide radicals and could be decomposed during the charge-discharge process, leading to fast degradation and termination of the battery.^{218,219} Several researchers detected the carbonate species, such as Li_2CO_3 , lithium alkyl carbonate ($\text{RO}-(\text{C}=\text{O})-\text{OLi}$), lithium propyl bicarbonate ($\text{C}_3\text{H}_6(\text{OCO}_2\text{Li})_2$), Li formate (HCO_2Li), Li acetate ($\text{CH}_3\text{CO}_2\text{Li}$) and alkoxides, at the cathode after cycle-life tests, confirming the decomposition of carbonate-based electrolytes due to the superoxide radicals as discharge reaction intermediates.^{191,192,211,220-223} Furthermore, during recharging, evolved CO_2 gas was also detected at the cathode as a consequence of the decomposition of carbonate species.²²⁴ It has therefore been confirmed that the decomposition of solvents can lead to large overpotentials and poor cycling performance for Li-air batteries using electrolytes with carbonate based solvents.²¹⁰ As a result, it seems carbonate based solvents have been essentially abandoned by scientists

worldwide, and many efforts have been conducted to find alternatives.

Currently, the most common solvents used in non-aqueous Li-air batteries are ethers and sulfones based solvents, which have been proven to have long-term chemical stability even in the presence of the superoxide radicals.^{199,225,226} These ethers and sulfones based solvents mainly contain TEGDME,^{36,161,227} triethylene glycol dimethyl ether,²²⁸ 1,2-dimethoxyethane (DME),^{36,100,229-232} DMSO²³³⁻²³⁵ and tetramethylene sulfone (TMS).²³⁶ With these solvents, Li_2O_2 has been found to be the predominant discharge product at the cathode. For example, Huff et al.,²⁰⁶ Tsiouvaras et al.,²¹⁰ Leskes et al.,²³⁷ Lim et al.,²³⁸ and Wen et al.²⁰⁷ confirmed the Li_2O_2 being the essential discharge products at the cathode by using NMR, XRD, XPS technology as well as on-line mass spectrometer, respectively. However, many articles have also observed by-products other than Li_2O_2 in Li-air batteries using ethers and sulfones based solvents. For example, Huff et al.²⁰⁶ found the polymer with a chemical formula of $[\text{OCH}_2\text{OCO}_2\text{CH}_2\text{CH}_2\text{OCO}_2\text{CH}_2\text{CH}_2\text{OCO}_2\text{CH}_2\text{O}]_n$. Tsiouvaras et al.²¹⁰ detected the formation of other oxygen-containing discharge products which could only be oxidized at high potential to form CO_2 . Assary et al.²³⁹ reported the interface between Li_2O_2 having Li-O-Li sites with high spin on the surface and ether solvents might have a hydrogen abstraction, leading to the production of oxidized species, such as aldehydes, carboxylates and LiOH. Ryan et al.²⁴⁰ observed that TEGDME could participate in the charging process, even at moderate voltages in the absence of O_2 . Barile et al.¹⁹¹ studied the stability of the ether electrolytes using DEMS technology, and revealed that the amount of O_2 evolved during the charging process was significantly less than that expected for complete Li_2O_2 formation and decomposition, regardless of the catalyst employed. The investigations of Trahan et al.²³³ and Xu et al.²³⁶ on Li-air batteries with sulfone based solvents detected LiOH formation through a chemical reaction of the superoxide with the electrolytes. Younesi et al.²⁴¹ found some lower

oxidation state oxygen and S compounds at the cathode, such as LiOH (compared to Li₂O₂) and lithium sulfides (compared to DMSO), respectively, which are attributed to the reaction between DMSO and Li₂O₂. Xu et al.²⁴² studied sulfoxide based Li-air batteries and found the predominant product was Li₂CO₃ but not Li₂O₂. Gallant et al.²²² found the accumulation of Li₂CO₃ in the cathode of Li-air batteries with DME as solvent during the discharge process.

Amide based solvents are another type of solvents with long-term chemical stability in the presence of superoxide radicals. The most thoroughly studied ones in non-aqueous Li-air batteries are N,N-dimethylformamide (DMF),^{34,243} N,N-dimethylacetamide (DMA)¹⁶⁰ and N,N-dimethyltrifluoroacetamide (DMTFA)²⁴⁴. For example, Walker et al.¹⁶⁰ studied the cycle life of a Li-air battery with DMA as the solvent in the electrolyte, and did not observe significant CO₂ production over even 80 cycles of charge-discharge cycling. With a DMA:DMTFA (98:2, v/v) electrolyte, Bryantsev et al.²⁴⁴ found O₂ is a dominant recharge product within the normal oxidation potential window of 3.6-4.2 V, and the small spike in CO₂ could only be observed at potentials above 4.0 V and didn't increase on cycling, thus indicating negligible accumulation of HCO₂Li and CH₃CO₂Li at the cathode. However, Chen et al.³⁴ found some electrolyte decomposition into Li₂O₂, Li₂CO₃, HCO₂Li, CH₃CO₂Li, NO, H₂O and CO₂ and the accumulation of Li₂CO₃ at the cathode during the cycling process of Li-air batteries utilizing dimethylformamide as the solvent in the electrolyte.

In addition, the application of ionic liquids as solvents in non-aqueous Li-air batteries is attracting more and more attention due to their high boiling point and saturated steam pressure.²⁴⁵⁻²⁴⁹ The main ionic liquids that have been investigated includes: 1-ethyl-3-methylimidazolium bis(trifluoromethylsulfonyl)imide (EMITFSI),²⁵⁰ N-methyl-N-propylpiperidinium bis(trifluoromethanesulfonyl)amide (PP13TFSA),²⁵¹ N-methyl-N-propylpiperidinium-bis(trifluoromethanesulfonyl)imide (PP13TFSI),¹²⁶ N-methyl-(n-butyl)

pyrrolidinium bis(trifluoromethane sulfonyl) imide (PYR14TFSI),^{219,252} 1-butyl-1-methylpyrrolidinium bis(trifluoromethylsulfonyl) imide ([C₄mpyrr][NTf₂]),¹³⁸ 1-butyl-3-methylimidazolium bis(trifluoromethylsulfonyl) imide ([C₄mim][NTf₂]),¹³⁸ and 1-butyl-3-methylimidazolium tetrafluoroborate [C₄mim][BF₄]).¹³⁸ For example, with PP13TFSA as the solvent, Mizuno et al.²⁵¹ identified the cathode discharge product as Li₂O₂, and only a minor by-product of Li₂CO₃ was observed on the cathode surface near O₂ gas. Herranz et al.²¹⁹ showed that PYR14TFSI was more stable than PC with rotating ring-disk electrode transient measurements, and Elia et al.²⁵³ found that the discharge product was amorphous Li₂O₂ when PYR14TFSI was used as the solvent. However, Xu et al.²⁴² observed a large amount of Li₂CO₃ produced from the oxidation and decomposition of PYR14TFSI.

(2) Effect of the type of lithium salts on battery performance

Besides the solvents, lithium salts in the electrolyte also have significant influence on the cathode performance of non-aqueous Li-air batteries. In early studies, lithium hexafluorophosphate (LiPF₆) was employed as the lithium salt along with a mixture solvent containing PC, EC and polyacrylonitrile (PAN) to serve as the electrolyte in Li-air batteries,^{19,20} and the cathode products were determined to be Li₂O₂ using Roman spectroscopy. However, many researchers in the studies which followed found LiPF₆ in this electrolyte was unstable during charge-discharge cycles of the batteries, leading to deteriorated performance and fast shutdown of the battery.²⁵⁴⁻²⁵⁶ More recently, extensive research has shifted to explore reasonable couples of lithium salts and the solvents in order to improve the overall battery performance. To date, the lithium salts that have been studied in non-aqueous Li-air batteries mainly include: LiPF₆,²⁵⁷ lithium bis(trifluoromethanesulfonyl)imide (LiTFSI),^{258,259} lithium triflate (LiCF₃SO₃),¹⁹¹ lithium tetrafluoroborate (LiBF₄),¹⁵⁹ lithium perchlorate (LiClO₄),^{260,260} lithium nitrate (LiNO₃),^{260,261}

and lithium bis(oxalate) borate (LiBOB).⁶¹ However, decomposition of lithium salts during the charge-discharge process has been observed to be a major challenge. For example, Nasybulin et al.¹⁵⁹ showed that LiBF₄ and LiBOB could decompose to form LiF, lithium oxalate, and lithium borates, whereas LiTFSI, LiCF₃SO₃ and LiPF₆ had minor decomposition in the solvent of tetraglyme. They also found that LiBr and LiClO₄ exhibited the best stability during the discharge process. Chalasani et al.²⁶² found that LiPF₆ could react rapidly with Li₂O₂ to generate OPF₂OLi and LiF in EC/DEC/DMC (1:1:1, v/v/v), PC, tetraglyme and acetonitrile (ACN), whereas LiBF₄, LiBOB and LiTFSI had excellent stability in the presence of Li₂O₂ in both PC and DME. Therefore, they suggested that LiPF₆ is a poor salt for rechargeable Li-O₂ battery, and the interaction between Li₂O₂ and LiPF₆ in carbonates could result in a dramatic decrease in the thermal stability of the electrolyte. In recent studies, more and more researchers incline that the stability of lithium salts should be strongly dependent on the solvents used. For example, Du et al.¹⁵⁸ found LiPF₆ could decompose in tri(ethylene glycol)-substituted trimethylsilane (1NM3) electrolyte forming HF whereas no tracks could be detected in TEGDME. They also found both LiTFSI and LiCF₃SO₃ were very stable in both 1NM3 and TEGDME solvents. Younesi et al.¹⁶⁵ demonstrated that both LiClO₄ and LiBOB could decompose in PC while there was no decomposition in EC/DEC solvent.

(3) Effect of carbon materials and other compositions of cathode reaction layer on battery performance

In addition to the electrolyte, carbon materials, as the basis of porous cathodes and the catalyst support for non-aqueous Li-air batteries, can also affect the formation of cathode products owing to its instability during the charge-discharge process.^{231,263} For example, Itkis et al.²⁶⁴ showed carbon materials containing activated double bonds or aromatics could be easily attacked through nucleophilic reactions by superoxide radicals to form epoxy-groups

which were further converted into carbonates during the discharge process, thus limiting the rechargeability of Li-air cells. While for carbon materials with a low amount of functional groups and defects, a better stability keeping the carbon will-o'-the-wisp lit for lithium-air battery could be observed. Ottakam Thotiyl et al.¹⁰¹ studied the carbon electrode in a Li-O₂ battery with DMSO and tetraglyme-based electrolytes, and revealed the behavior of carbon material was dependent on the hydrophobicity/hydrophilicity of its surface, and both the electrode potential dependent carbon decomposition and electrolyte decomposition could be promoted by the carbon surface. Normally, hydrophobic carbon is relatively stable with little or no decomposition when compared to that of hydrophilic carbon. With hydrophilic carbon, Li₂CO₃ accompanied by lithium carboxylates (HCO₂Li and CH₃CO₂Li) could be formed and accumulated on the carbon surface. This is because the carbon surface's decomposition and reaction with the intermediate products such as LiO₂ and Li₂O₂ and the enhanced electrolyte decomposition, leading to a rapid polarization, electrode passivation, and capacity fading on cycling. With respect to this, Gallant et al.²²² considered that the Li₂CO₃-like species might be associated with the reactivity between carbon and Li₂O₂ or other reaction intermediates.

Besides carbon materials, other compositions in cathode reaction layer such as binders (Kynar and Teflon) may also participate in the discharge reaction to form cathode side products such as LiF.^{242,265,266}

In summary, although the ideal cathode product for non-aqueous Li-air battery is only Li₂O₂, the side products produced in cathode during the charge-discharge process including Li₂O, Li₂CO₃, LiF and many others seem to be unavoidable, which are strongly dependent on the types of electrolytes (Li salt + solvent), carbon materials, catalysts and binders. Therefore, the synergy between them should be given more attention in order to design and develop practical Li-air batteries.^{101,267,268}

2.4 Properties and morphology of lithium peroxide and their influences on Li-air battery performance

As the ideal cathode product in non-aqueous Li-air batteries, Li_2O_2 is an insulator with a calculated band gap of 4.9 eV and is also insoluble in organic electrolytes.^{172,269} As a result, the cathode reaction kinetics could be partially limited by the electrical and ionic transport properties of the bulk Li_2O_2 , particularly when the Li_2O_2 particle size or film thickness is increased.²⁷⁰ With these potential constraints in mind, the properties and morphology of Li_2O_2 are expected to be important parameters influencing Li-air battery performance in terms of charge-discharge polarization, discharge capacity, round-trip efficiency, rate capability and cycle-ability.^{178,271}

In general, understanding of the insulative property of Li_2O_2 is mainly based on experimental measurements and theoretical/mathematical calculations. It seems the insulative properties of Li_2O_2 can be modified to improve its electrical conductivity. For example, Radin et al.^{272,273} found the stable surface of Li_2O_2 was half-metallic which might mitigate electrical passivation through the growth of Li_2O_2 , leading to some enhanced reversibility of Li_2O_2 during recycling of the battery. Garcia-Lastra et al.²⁷⁴ postulated the polarons (both hole and electron) could be formed on the surface of Li_2O_2 , and the hole polarons had a much higher mobility than the electron polarons during the growth of Li_2O_2 . This would result in the Li_2O_2 having a certain electrical conductivity coming from the presence of polarons. Ong et al.²⁷⁵ also found the formation of hole polarons, and reported the migration barriers for the free polarons were between 68 and 152 meV. In their opinion, the electrical conductivity of lithium peroxide was likely to be determined by the vacancy diffusion. Additionally, a number of theoretical predictions suggested some surfaces of lithium peroxide had unpaired spin states that could play a role in the electrical conductivity of the discharge

products,^{172,273,275-277} despite the fact bulk lithium peroxide has a large band gap. Lau et al.²⁷⁸ reported the high spin states were more stable in high stoichiometric lithium peroxide clusters $((\text{Li}_2\text{O}_2)_n)$, thus promoting the formation of superoxide-like structures which could facilitate important conductivity mechanisms on the surface of Li_2O_2 . For example, the triplet spin state was favoured over a closed shell singlet spin state for a dimer $((\text{Li}_2\text{O}_2)_2)$, trimer $((\text{Li}_2\text{O}_2)_3)$, and tetramer $((\text{Li}_2\text{O}_2)_4)$ of lithium peroxide, and the quintet spin state was presented in $(\text{Li}_2\text{O}_2)_{16}$, while the closed shell singlet was strongly favored in the lithium peroxide monomer $((\text{Li}_2\text{O}_2)_1)$.

Furthermore, the kinetics of oxygen evolution reaction (OER) during the charge process has been proposed to be highly dependent on the surface orientation of lithium peroxide. Mo et al.'s study with first-principle calculation²⁷⁹ revealed the OER processes were kinetically limited by the high energy barrier for the evolution of oxygen molecules, and the rate of OER was highly dependent on the surface orientation of Li_2O_2 , that is, the rate of OER was slow on the abundant surfaces, such as the $(11\bar{2}0)$ and (0001) surfaces, while it was fast on the high energy surfaces.

The morphology of Li_2O_2 also has a significant influence on the performance of Li-air batteries.²⁸⁰ The morphology change of lithium peroxide in the cathode during the charge-discharge process can generally be described as: the Li_2O_2 first nucleates with the initiation of discharge, then grows during the discharge process, and finally decomposes in charge process.^{281,282} To date, a variety of Li_2O_2 morphologies, such as toroidal-shaped,^{189,194,196,198,283,284} spherical particles,^{84,285-287} elongated particles,^{288,289} close-packed nanosheets,^{202,290} rough thin films (thick layer)^{204,291,292} and porous ball-like,²⁹³ in the discharged cathode have been reported in literature (Fig. 6).

Regarding the specific growth of Li_2O_2 during discharge process of Li-air battery, there

are many different viewpoints, probably because of different materials used and different methodologies. For example, Jung et al.²⁸² presented that the amorphous spherical particles of Li_2O_2 with size in the range of several hundreds of nanometers could be formed at first, and then the crystalline Li_2O_2 primary particles started to nucleate on the pre-existent amorphous particle surface toward the end of discharge. Thus, lithium peroxide particles with several different morphologies could be observed on the surface of the discharged cathode, as shown in Fig. 7. The authors assumed the hollow spherical structure of lithium peroxide formed in the discharged cathode could be attributed to the simultaneous formation on the outer surface and decomposition on the inner surface. However, Fan et al.²⁸¹ and Zhai et al.¹⁷⁷ proposed the Li_2O_2 particles could grow from the small round solid at the beginning of discharge, and then the initial Li_2O_2 tiny deposits evolved into abacus-ball-shaped particles with increasing depth of discharge (Fig. 8). Mitchell et al.²⁸⁷ reported the Li_2O_2 particles could change into a toroid-shape while the particle size was increased up to 1 μm with increasing the depth-of-discharge.

Normally, the morphology of lithium peroxide is significantly dependent on the current density governing the electrochemical charge-discharge process.²⁹⁴ Mitchell et al.²⁹⁵ reported Li_2O_2 particles were formed first as some stacked thin plates with thickness of about 10 nm, which then spontaneously splayed so the secondary nucleation of new plates eventually developed into a particle with a toroidal shape at low discharge rates. It was discussed that since Li_2O_2 crystallites had large (001) crystal faces which were consistent with the theoretical Wulff shape, it could grow by a layer-by-layer mechanism at high discharge rates. Similarly, Adams et al.¹⁷⁹ revealed large toroidal morphologies of Li_2O_2 rose at low current densities in the range of 5-25 mA cm^{-2} while the thin-film morphologies appeared at higher current densities (50 and 100 mA cm^{-2}). Furthermore, Li^+ ion concentrations in an electrolyte solution could also tailor the morphology of discharge products at the cathode surface. In Liu

et al.'s study,²⁹⁶ it was revealed the discharge products existed in the form of about a 10 nm layer at a Li^+ concentration of 10^{-3} M, while they changed into large chunks at a Li^+ concentration of about 2-3 M.

The distribution of Li_2O_2 across the cathode thickness has also been investigated to obtain their effect on the battery performance. A non-uniform distribution was reported by Nanda et al.,²⁹⁷ they found the concentration of lithium species near the edge of the air electrode was higher and also relatively more uniform than in the center of the cathode. They assumed the origin of such anomalous behavior could be due to the competition between the transport of lithium and oxygen and the accompanying electrochemical reaction. Zhang et al.^{292,298} found the surface at the air side was covered almost completely by the discharge products, while the surface at the membrane side had some clear open pores. Another investigation by Zhang et al.⁹¹ revealed the deposition of discharge products on both sides of the air cathode was dependent on the status of electrolyte-filling. For the electrode containing insufficient electrolyte, more discharge products were deposited on the separator side, but the denser deposition was on the air side for an electrolyte-flooded cathode. Therefore, they proposed the discharge products could be evenly deposited throughout the air cathode by adjusting electrolyte-filling status. Similarly, Ren et al.⁹⁰ observed the discharge current density had a significant influence on the deposition and distribution of Li_2O_2 particles inside the air cathode, an increase in current density could lead to a shift of Li_2O_2 from the electrolyte interface to the air/cathode interface.

Cathode catalysts for ORR and OER have also been reported to influence the growth, morphology, distribution and particle size of the discharge product Li_2O_2 . Density Functional Theory (DFT) calculations revealed the discharge products mostly preferred to nucleate and grow around the defective sites on the cathode.²²⁸ Li et al.²⁹⁹ demonstrated with experiments

that the morphologies of Li_2O_2 on the surface of the cathode catalyzed by the GNSs (graphene nanosheets) and N-GNSs (Nitrogen-doped graphene nanosheets) were significantly different from each other. The formed diameters of the Li_2O_2 particles were about 600-1000 nm when GNSs was used as the catalyst and 200-500 nm with N-GNSs, respectively. The distribution of Li_2O_2 was more uniform on N-GNSs than it was on GNSs, while the Li_2O_2 particles could aggregate into large clusters on GNSs and some surface was free of coverage. Similarly, Lee et al.¹⁹⁶ reported the entire surface of the cathode with acid-leached $\text{Na}_{0.44}\text{MnO}_2$ as catalyst was uniformly covered with Li_2O_2 toroids, whereas only the outer edge of the cathode with pristine $\text{Na}_{0.44}\text{MnO}_2$ as catalyst and the carbon electrode without a catalyst was covered with Li_2O_2 (Fig. 9).

Although a number of studies have reported different Li_2O_2 morphologies formed during discharge and their effects on battery performance, a consistent understanding, particularly of their effect on OER kinetics and pathways during the recharge process, has not yet been reached. Gallant et al.¹⁷⁸ found the cathode producing small Li_2O_2 particles less than 20 nm in diameter showed a different current-voltage profile from the cathode producing disc/toroid Li_2O_2 particles with a diameter ranging from 50 to 200 nm. According to the research in *ref.* 177, different morphological evolutions of cathode products during discharge (Fig. 8) and charge (Fig. 10) processes suggest different formation-decomposition mechanisms and the formation of disproportionate superoxide which was identified in the grain boundaries and outer parts of the toroids.

2.5 Approaches for achieving ideal cathodes for non-aqueous Li-air batteries

A high-performing rechargeable non-aqueous Li-air battery needs to possess at least

four characteristics^{12,300} as shown in Fig. 11: (1) High specific capacity; (2) High round-trip efficiency; (3) Good rate capability; and (4) Excellent cycling performance. Actually, these characteristics originate largely from the cathode of the battery. Thus, in the following paragraphs, the crucial approaches for creating an ideal cathode, to achieve the high level of desired performance in non-aqueous Li-air batteries, are discussed in details.

2.5.1 Improving specific capacity

As generally known, the discharge product of Li_2O_2 does not dissolve in the organic electrolyte of the non-aqueous Li-air battery, but accumulates in the pores of the cathode during discharge process. Therefore, the capacity of Li-air battery is actually determined by the amount of discharge products that can be accommodated in the cathode. It has been observed the discharge process can be suddenly terminated by the blocking of the pores in the cathode, preventing further oxygen diffusion to the reaction sites.³⁰¹⁻³⁰³ Normally, using highly-active catalysts and optimum catalyst loadings, in combination with making a uniform distribution of electrode materials, will improve the structure of the cathode. This in turn will enhance the utilization of the pore structure in the air electrode, thereby improving the specific capacity of the battery.^{304,305} In addition, there is unavoidable passivation along with the growth of Li_2O_2 which would promote degradation of the battery due to the insulator characteristics of Li_2O_2 during the discharge process, therefore the adaptive property and morphology of Li_2O_2 could improve the discharge capacity.^{306,307}

2.5.2 Improving round trip efficiency

The charge-discharge processes of non-aqueous Li-air batteries generally proceed with two reactions, ORR for discharge and OER for recharge. Due to the slow kinetics of both reactions, there is often an unusual deviation between the charge and discharge voltages of Li-air batteries even at low current density, leading to low round-trip efficiency even though

the coulombic efficiency (charge in/charge out) may be close to 100%. Using a bi-functional catalyst which has catalytic activities for both ORR and OER on the cathode could reduce the overpotentials during the charge-discharge processes by increasing the discharge voltage and decreasing the charge voltage through accelerating the kinetics of ORR and OER, thus increase the round-trip efficiency.^{94,95,105,110,308-310}

It was found that the overpotential increase during the discharge process with the growth of lithium peroxide was owing to Li_2O_2 's insulativity which could lead to a decreased discharge voltage.³⁰⁷ As a result, the charge voltage could also exhibit at a higher value. Therefore, the round-trip efficiency of Li-air batteries can be enhanced by modifying the nucleation and growth of Li_2O_2 as well as optimizing its morphology, particle size and distribution in the cathode.

2.5.3 Improving rate capacity

In addition to quick diffusion of oxygen and a high rate transfer of both electrons and ions inside the air cathode,^{311,312} fast ORR and OER reaction rates on the cathode are also of great importance for enhancing the rate capability of Li-air batteries.²³⁰ In this regard, employing highly-active catalysts is both very important and necessary.

2.5.4 Improving cycling performance

In general, ORR/OER catalysts play an important role in promoting the cycle-ability of Li-air batteries. An efficient catalyst would not only drive the formation of desired reversible Li_2O_2 as a discharge product, while at the same time reduce the generation of by-products from electrolyte decomposition and the corrosion of the electrode materials. Such a catalyst would also enhance the reduction rate of Li_2O_2 during the charge process, thereby resulting in an improved overall cycling performance.^{19,83,94,110,313} At the same time, a stable cathode fabricated from porous materials is favorable to achieving excellent cycling performance

through facilitating oxygen diffusion and improving electrolyte wettability, leading to the fast accumulation and decomposition of the discharge products of Li_2O_2 in the pores of the cathode during the cycling process of the Li-air battery.^{28,314} In addition, passivation of the electrode materials should be well controlled^{306,315,316} and the electrode materials should not scale off from the substrate topography during cycling of the battery.

Overall, the electrical conductivity of the cathode must be sufficient to achieve high battery performance.²⁸ To obtain high conductivity, the ratios among the electrode materials, such as carbon materials, catalysts, conductive agents and binders, the substrate and current collector should be comparatively optimized. Furthermore, fast ion transfer within the interface between electrode and electrolyte, which is mainly determined by the wettability of the electrolyte on the electrode, is also very important.^{28,317} In addition, the cathode and its materials must have a durable porous structure in order to facilitate the diffusion and transport of oxygen.^{28,271,304,318} Nevertheless, the wettability of electrolyte and the diffusion of oxygen are mutually contradictory³¹⁹ due to the limited solubility of oxygen in organic electrolytes³²⁰. Therefore, a trade-off strategy should be reached by optimizing the electrode materials and cathode structure.³⁰⁴

In the following contents of this review paper, the progress and knowledge garnered in recent years about the cathode for non-aqueous Li-air batteries will be summarized from the aspects of: cathode materials, cathode structure and cathode fabrication process along with a discussion about the remaining challenges and research directions required to facilitate the future development of non-aqueous Li-air batteries.

3 Cathode materials

As discussed above, the cathode materials used in non-aqueous Li-air batteries should

have a durable porous structure in order to store discharge products and provide channels for oxygen diffusion. They should also possess high electrolyte wettability to satisfy the requirement of ionic transfer during the charge-discharge process. More importantly, the cathode materials including the catalyst should have the ability to accelerate the kinetics of both ORR and OER. The ideal cathode material with optimum structure/morphology/crystal forms can not only provide more space for the storage of discharge products but also to facilitate both the diffusion of oxygen and the formation of electrode wettability,^{311,321} while also enhancing its catalytic performance towards both ORR and OER due to the introduction of defects and vacancies.^{322,323}

At the current state of technology, a huge number of cathode materials, including some successfully used in fuel cells, Li-ion batteries and metal-air batteries,³²⁴⁻³²⁹ have been explored for incorporation into non-aqueous Li-air batteries. In this section, these materials are summarized as four main groups: carbon materials; metal and/or metal oxides; composite materials; and others.

3.1 Carbon materials

Carbon materials have been widely used as catalyst support, conductive agents and electrode material in fuel cells, lithium-ion batteries and electrochemical supercapacitors due to their excellent electrical conductivity and large surface areas.³³⁰⁻³³² In recent years, the application fields of carbon materials have been extended to Li-air batteries as cathode materials with growing interest worldwide because of their favourable properties. In non-aqueous Li-air batteries, carbon materials generally act as electrode materials to fabricate a porous cathode, and they can also work as catalysts towards ORR as well as OER.¹¹⁸

In general, carbon materials that have been explored for non-aqueous Li-air batteries can

be classified into three groups: (1) commercial carbon materials; (2) functional carbon materials; and (3) N-doped carbon materials, all of which will be given a detailed discussion in the following sub-sections.

3.1.1 Commercial carbon materials

Almost all commercially available carbon materials, such as Super P, Ketjen black (KB) (normally EC600JD and EC300JD), Activated carbon, Vulcan XC-72, Black pearl (BP 2000) and so on, have been explored as cathode materials for non-aqueous Li-air batteries.³³³⁻³⁵⁰ The reported discharge capacity of various commercial carbon materials are summarized in Table 2. As can be seen, the discharge capacities of the same types of carbon materials differ greatly from each other in different reports even at the same discharge current density. This indicates the discharge capacity can also be influenced by some other factors in addition to the cathode materials themselves.

Hayashi et al.³¹⁷ reported there was a rough correlation between the discharge capacity and the surface area of carbon materials, particularly the nano-sized pores such as mesopores on the carbon were able to serve as active sites for cathode reactions. They found that carbon materials with higher surface areas and larger number of mesopores could deliver higher discharge capacities. Meini et al.³⁵¹ also reported there was a strong correlation between the surface areas of carbon materials and their discharge capacities. For example, the carbon materials of Vulcan XC72, KB EC600JD and BP 2000 with surface areas of 240, 834 and 1509 m² g⁻¹ could display the discharge capacities of about 183, 439 and 517 mAh g_{carbon}⁻¹, respectively. Similarly, Cheng et al.'s study³⁰⁸ revealed the discharge capacities of Norit (4400 mAh g_{carbon}⁻¹), acetylene (3900 mAh g_{carbon}⁻¹) and Super P (3400 mAh g_{carbon}⁻¹) were in accordance with the relativity of their surface areas, i.e. 800, 75 and 62 m² g⁻¹ for Norit, Acetylene and Super P carbon black, respectively. Thus, the authors concluded larger surface

area of carbon materials should be beneficial for fabricating a cathode with higher discharge capacity. Xiao et al.³³⁶ showed KB EC600JD could exhibit the highest discharge capacity of 851 mAh g_{carbon}⁻¹ at a current density of 0.05 mA cm⁻² among the commercial carbon materials of BP 2000, Calgon, Denka and KB EC600JD, owing to its high mesopore volume that could store more discharge products and absorb more electrolyte. Beattie et al.²⁸ reported the KB-based cathode with a carbon loading of 1.9 mg cm⁻² exhibited a discharge capacity of 5813 mAh g_{carbon}⁻¹ at a current density of 0.1 mA cm⁻², while the capacities of 3378 and 404 mAh g_{carbon}⁻¹ could be achieved for the cathode with a carbon loading of 4 and 12.2 mg cm⁻², respectively. In another study by Gao et al.,³³⁴ it was demonstrated the Super P electrode displayed the highest discharge capacity among activated carbon SYTC-03, KB EC600JD, Vulcan XC-72 and Super P at a current density of 0.1 mA cm⁻². In Sun et al.'s investigation on Super P based cathodes,³³⁸ however, a very poor cycling performance was observed. The initial discharge capacity was 964 mAh g_{carbon}⁻¹, but the cell died after only 13 cycles at a current density of 100 mA g_{carbon}⁻¹.

Although Li-air batteries with commercial carbon materials based cathodes are feasible, many issues, such as low discharge voltage, high charge voltage, low round-trip efficiency, poor rate capability and cycling performance, resulted from the poor catalytic activity of commercial carbon materials,^{35,95,311,312} should be well addressed before their practical applications. Regarding the round-trip efficiency, the gaps between the charge and discharge potentials (ΔV) of Vulcan XC-72 and KB EC600JD-based cathodes were reported to be as wide as 1.69 V³³⁹ and 1.323 V,³⁵² respectively. The capacity retention of an acetylene carbon black electrode was only 37.07% when the current density was increased to 0.5 mA cm⁻² from 0.1 mA cm⁻².³¹¹ The discharge capacities of Norit, Acetylene and Super P based cathodes could be decreased from 4400, 3900 and 3400 mAh g_{carbon}⁻¹ (the 1st cycle) to 1150,

730 and 200 mAh g_{carbon}⁻¹, respectively, after fifty cycles at a current density of 70 mA g_{carbon}⁻¹.³⁰⁸ Therefore, in most recent studies, commercial carbon materials are usually used as conductive agents and/or catalyst support rather than for reaction sites in the cathode of non-aqueous Li-air batteries.^{201,205,308}

3.1.2 Functional carbon materials

Different from the commercial carbon materials, functional carbon materials, such as graphene,^{78,339,350,353} mesoporous carbon,^{175,204,289,338} carbon nanotubes (CNTs),³⁵⁴⁻³⁵⁶ carbon nanofibers (CNFs),^{287,292} and carbon microfibers,^{203,201} have some unique functions in battery cathode reactions in non-aqueous Li-air batteries, due to their unique structures and greater number of defects/vacancies.

Graphene is a monolayer of carbon atoms packed into a dense honeycomb crystal structure.³⁵⁷⁻³⁵⁹ It has attracted great attention as a carbon candidate since its discovery by Novoselov et al.³⁶⁰ in 2005. With the merits of high electron transfer rate, large surface area, high conductivity as well as thermal and chemical stability,^{357,361,362} graphene has been widely used as catalyst support or metal-free catalyst in fuel cells^{363,364} and anode materials in Li-ion batteries.^{365,366} Recently, graphene has been tested as a promising cathode material for Li-air batteries due to its extremely high discharge capacity and high round-trip efficiency. These merits have been attributed to its ideal 3D 3-phase electrochemical area and the diffusion channels for electrolyte and oxygen as well as its unique structure,^{64,339,350,353,367-369} although detailed mechanisms for the ORR/OER on graphene in non-aqueous Li-air batteries are still unclear at this time. The graphene nanosheets (GNSs) based electrode was employed by Li et al.³⁵⁰ in non-aqueous Li-air batteries, showing a discharge capacity of 8705.9 mAh g_{carbon}⁻¹ at a current density of 75 mA g_{carbon}⁻¹, which was much higher than that of the electrode with commercial carbon materials of BP 2000 and Vulcan XC-72 (Fig.12a). They

claimed the active sites at the edge of graphene could significantly contribute to the superior electrocatalytic activity towards ORR (Fig. 12b-e). Wang et al.³⁷⁰ showed the GNSs based electrode had a discharge capacity of 2000 mAh g_{carbon}⁻¹, a discharge voltage of 2.80 V and a charge voltage of 3.90 V at a current density of 50 mA g_{carbon}⁻¹. Similar to the study of Li et al.³⁵⁰ on GNSs based electrodes, the authors attributed the good round-trip efficiency of the graphene-based electrode to the presence of dangling σ -bonds (sp³ carbon atoms) at the edges and defects of graphene. The high electric conductivity was also considered to be another contributor. In a comparative study by Sun et al.³³⁹ on both GNSs and Vulcan XC-72 carbon based electrodes, the former exhibited a significantly lower ΔV and a much better cycling performance than the latter. Liu et al.³⁷¹ synthesized graphene directly on the skeleton of porous nickel foam (3D-G electrode) by chemical vapor deposition (CVD) method, and achieved a discharge capacity of 970 mAh g_{carbon+catalyst}⁻¹ at a current density of 0.083 mA cm⁻². The highest discharge capacity to date (15000 mAh g_{carbon}⁻¹ at a current density of 0.1 mA cm⁻²) of a graphene-based cathode was reported by Xiao et al.²²⁸ using a novel hierarchical arrangement of structural and functionalized graphene sheets. The authors reported oxygen can spread rapidly in the microporous channels of the hierarchically porous graphene due to the unique bimodal porous structure. Meanwhile, the highly connected nanoscale could offer a high density of reactive sites for Li/O₂ reactions, and the defects and functional groups on graphene could promote the formation of the isolated nanosized Li₂O₂ particles to prevent air blocking in the cathode.

Mesoporous carbon, mainly referring to the carbon with pore sizes ranged from 2 to 50 nm, can be classified into two categories: the ordered mesoporous carbon (OMC) and the disordered mesoporous carbon (DOMC), according to the structure and morphology.³⁷² The former (OMC), which is normally synthesized with a template of mesoporous silica, such as

SBA-15, M41S and MCM-48, etc.,³⁷³⁻³⁷⁵ is normally preferred as cathode material for non-aqueous Li-air batteries due to its high specific surface area, excellent electrical conductivity and fast mass transport. Sun et al.³³⁸ demonstrated that the unique ordered mesoporous structure of CMK-3, a mesoporous carbon synthesized by using mesoporous silica SBA-15 as the template, could facilitate the infiltration of the electrolyte and the diffusion of oxygen in the cathode. The discharge voltage of a CMK-3 electrode (about 2.6-2.7 V) was slightly higher than that of Super P, while the charge voltage (about 4.15 V) was apparently lower than that of Super P, and the CMK-3 electrode could demonstrate a higher discharge capacity and better cycling performance than the Super P cathode. The initial discharge capacity of the CMK-3 electrode was about 1324 mAh g_{carbon}⁻¹ and could sustain 521 mAh g_{carbon}⁻¹ at the 15th cycle, while the Super P electrode could not survive more than 13 cycles at 100 mA g_{carbon}⁻¹. Yang et al.¹⁷⁵ assumed the enhancement in discharge performance of mesocellular carbon foam (MCF-C), prepared by using mesocellular foam (MCF) silica as template, could be attributed to its large pore volume and ultra-large mesoporous structure which allowed more lithium peroxide deposits during the discharge process when compared to Super P (Fig. 13). Guo et al.³⁷⁶ prepared some ordered hierarchical mesoporous/macroporous carbon sphere arrays (MMCSAs) with monodisperse polystyrene spheres as a template. The electrode fabricated with 50 wt% MMCSAs displayed a discharge capacity of 7000 mAh g_{carbon+catalyst}⁻¹ at a current density of 50 mA g_{carbon+catalyst}⁻¹.

Carbon nanotubes (CNTs), including single wall carbon nanotubes (SWCNTs)³⁷⁷ and multiwall carbon nanotubes (MWCNTs),³⁷⁸ have recently been investigated as cathode materials for non-aqueous Li-air batteries because of their high chemical and thermal stability, high elasticity, high tensile strength and high conductivity resulting from their unique structures. For example, Yoon et al.³⁷⁹ reported the pure CNTs electrode could exhibit a

discharge capacity of about 800 mAh $g_{\text{electrode}}^{-1}$ at a current density of 0.4 mA cm^{-2} . Shen et al.³⁸⁰ presented the specific capacity and discharge voltage of pure CNTs sponge was 6424 mAh g^{-1} and 2.45 V, respectively, at a current density of 0.05 mA cm^{-2} . In Mi et al.'s study, the CNTs prepared using CVD method could give the discharge capacities of 2079 and 3483 mAh g_{carbon}^{-1} in carbonate and ether based electrolytes, respectively, at a current density of 100 mA g_{carbon}^{-1} .³⁸¹ Li et al.³⁵⁴ showed the partially cracked CNTs electrode delivered a capacity of 1513 mAh g_{carbon}^{-1} at a current density of 0.01 mA cm^{-2} , which was higher than that of 800 mAh g_{carbon}^{-1} obtained from MWCNTs electrode. Cui et al.¹⁶³ demonstrated the vertically aligned carbon nanotubes (VACNTs) based cathode had discharge capacities of around 3500 mAh g_{carbon}^{-1} and 1000 mAh g_{carbon}^{-1} , at the current densities of 0.1 mA cm^{-2} and 0.3 mA cm^{-2} , respectively, at the temperature of 60 °C. The authors also reported the initial columbic efficiency of 79% at 0.1 mA cm^{-2} , 74% at 0.2 mA cm^{-2} and 71% at 0.3 mA cm^{-2} for the studied VACNTs cathode. Wang et al.³⁸² prepared a freestanding carbon nanotubes (CNTs) based electrode via a facile impregnation method, and attained a discharge capacity of about 8300 mAh g_{carbon}^{-1} and a discharge plateau of about 2.75 V at a current density of 0.1 mA cm^{-2} . When the discharge rates are increased to 0.2 and 0.5 mA cm^{-2} , the discharge capacities of about 8000 mAh g_{carbon}^{-1} and 2000 mAh g_{carbon}^{-1} can be achieved, respectively. In Lim et al.'s study,³⁸³ a hierarchical-fibril CNTs electrode with 10 sheets of the CNT fibril was fabricated from dense carbon forests on a Ni-mesh current collector, and a discharge capacity of about 2500 mAh $g_{\text{electrode}}^{-1}$ was obtained at a current density of 2000 mA $g_{\text{electrode}}^{-1}$, which could be sustained after about 20 cycles. Nakanishi et al.³⁸⁴ prepared cup-stacked-type carbon nanotubes (CSCNTs) and the heat-treated CSCNTs based cathodes, the discharge capacities of 195 and 122 mAh $g_{\text{electrode}}^{-1}$, respectively, were obtained at a current density of 0.02 mA cm^{-2} . Chen et al.³⁸⁵ prepared the multi-walled carbon nanotube paper (MWCNTP)

by the floating catalyst method and achieved a discharge capacity of $34600 \text{ mAh g}_{\text{carbon}}^{-1}$ at a current density of $500 \text{ mA g}_{\text{carbon}}^{-1}$, which was probably the highest discharge capacity reported till now. The authors attributed the enhanced performance to large amount of void space in the MWCNTs for storage of Li_2O_2 and the interpenetrating MWCNT networks for facile electron transport.

In addition to graphene, mesoporous carbon and CNTs, some other functional carbon materials, such as **Carbon nanofibers (CNFs) and Carbon microfibers (CMFs)**, have also been employed to fabricate cathode for Li-air batteries. Zhang et al.²⁹² prepared a cathode with CNFs combined with CNTs, an initial discharge capacity of about $1500 \text{ mAh g}_{\text{carbon}}^{-1}$ was observed, but the recharge capacity was only $120 \text{ mAh g}_{\text{carbon}}^{-1}$ at a current density of 0.2 mA cm^{-2} . The activated carbon microfiber (ACMF) electrode exhibited a discharge capacity of $4116 \text{ mAh g}_{\text{carbon}}^{-1}$ and a charge voltage of 4.3 V at a current density of 0.025 mA cm^{-2} .²⁰³ The all-carbon-fiber electrode prepared by Mitchell et al.^{287,287} yielded a gravimetric energy of about 2500 Wh kg^{-1} .

Recently, several novel carbon frames, such as carbon spheres, carbon nanoballs (CNB) and honeycomb-like carbon (HCC), were also introduced into Li-air batteries as cathode materials. Park et al.³⁸⁶ prepared carbon spheres using a modified hydrothermal synthesis, and used them as the cathode materials in a non-aqueous Li-air battery. A discharge capacity of $4200 \text{ mAh g}_{\text{electrode}}^{-1}$ was observed. However, the charge capacity is only 13% of the discharged capacity in the voltage range from 4.35 to 2.35 V at a current density of $200 \text{ mA g}_{\text{electrode}}^{-1}$. Kang et al.³⁸⁷ prepared the CNB by a solution plasma process and found a CNB based electrode could obtain a discharge capacity of $3600 \text{ mAh g}_{\text{carbon}}^{-1}$ at a current density of about $67 \text{ mA g}_{\text{carbon}}^{-1}$, which was approximately 30% higher than that of KB carbon. The authors attributed the enhanced performance to the high pore volume and meso-macro

structure of the CNB material. Soavi et al.³⁸⁸ prepared a meso-macroporous carbon using colloidal silica as a template, and employed this material as a catalyst-free cathode for a Li-air battery. In their work, a discharge capacity of 2500 mAh g_{carbon}⁻¹, a discharge voltage at 2.6 V and a charge potential of about 3.8 V were displayed at a current density of 0.05 mA cm⁻². Yang et al.³⁸⁹ prepared a diamond like carbon thin film electrode by radio frequency sputtering, a discharge plateau around 2.7 V and a discharge capacity of 2318 mAh g_{carbon}⁻¹ were demonstrated at a current density of 220 mA g_{carbon}⁻¹. Lin et al.²⁰⁴ prepared the hierarchically porous HCC with silica templates in different diameters (Fig. 14), the obtained cathode yielded a specific capacity of 3912 mAh g_{carbon}⁻¹ and a discharge voltage plateau of 2.75 V at a current density of 0.05 mA cm⁻². In addition, a much higher discharge capacity of 5862 mAh g_{carbon}⁻¹ was achieved by Li et al.²⁸⁹ at a current density of 30 mA g_{carbon}⁻¹ with the micron-sized HCC electrode.

3.1.3 N-doped carbon materials

Many studies have demonstrated carbon materials doped with a certain amount of non-metallic elements, such as nitrogen, can exhibit some improved electrochemical properties because the doped heteroatoms can change the chemical and electronic nature of carbon-based materials³⁹⁰⁻³⁹² leading to the formation of defects and functional groups.²⁹⁹ For example, nitrogen-doped (N-doped) carbon materials have been widely used in fuel cells as well as electrochemical supercapacitors.³⁹³⁻³⁹⁸ The general synthetic routes for N-doped carbon materials mainly include: heating carbon materials in a nitrogen-rich atmosphere (such as NH₃);^{49,55} heating the composite of carbon materials and nitrogen contained materials (such as macrocyclic compounds of porphyrin and phthalocyanin and conductive polymers of polypyrrole, polyaniline and melamine) in an inert atmosphere;^{399,400} nitrogen plasma treatment;^{401,402} CVD with nitrogenous compounds^{403,404} and so on⁴⁰⁵⁻⁴⁰⁸. In recent

years, N-doped carbon materials have attracted more and more attention for use as cathodes in Li-air batteries.^{299,409-412}

With their excellent electro-catalytic activity towards ORR in fuel cells,^{393,394} N-doped GNSs have also been counted to act as a simple and effective catalyst in the cathode of Li-air batteries.^{49,299,413} Yan et al.'s DFT investigation on the activity of graphene and N-doped graphene towards oxygen adsorption and dissociation showed N-doping could not only enhance the adsorption of oxygen atoms but also decrease the energy barrier of O₂ dissociation from 2.39 eV to 1.20 eV, leading to better catalytic activity toward O₂ dissociation reaction.⁴¹⁴ The first introduction of N-doped GNSs into Li-air batteries was conducted by Li et al.²⁹⁹ in 2012. They prepared N-doped GNSs by heating the pure GNSs under an atmosphere composed of high purity ammonia mixed with argon, thus obtaining a N-doped GNSs based cathode which exhibited the discharge capacities of 11660, 6640 and 3960 mAh g_{carbon}⁻¹ at the current densities of 75, 150 and 300 mA g_{carbon}⁻¹, respectively, much higher than the electrode with pure GNSs (Fig.15). Higgins et al.³⁹⁷ also showed that a 20 wt% N-doped graphene containing electrode could give a discharge capacity of 11746 mAh g_{carbon}⁻¹ which was about 42% higher than a pure KB electrode at a current density of 70 mA g_{carbon}⁻¹.

Similar to N-doped graphene, N-doped CNTs, carbon fiber and mesoporous carbon have also been considered to be candidates for cathode materials in Li-air batteries. The electrode with N-doped CNTs synthesized by a floating catalyst chemical vapor deposition (FCCVD) method³⁶⁷ could deliver a discharge capacity of 866 mAh g_{carbon}⁻¹ in an PC/EC (1:1 weight ratio) electrolyte containing 1 M LiPF₆, which was about 1.5 times higher than that of CNTs (590 mAh g_{carbon}⁻¹) at a current density of 75 mA g_{carbon}⁻¹. When the current density was increased to 150 and 300 mA g_{carbon}⁻¹, the N-doped CNTs electrode could attain the discharge capacities of 525 and 374 mAh g_{carbon}⁻¹, respectively. Similarly, Lin et al.⁴¹⁵ reported the N-

doped CNTs@Ni electrode prepared by FCCVD method displayed the discharge capacities of 779, 472 and 337 mAh g_{carbon}^{-1} in an DMSO electrolyte containing 1 M LiPF₆ at the current densities of 0.05, 0.1 and 0.2 mA cm^{-2} , respectively. In another research study on the N-doped CNTs synthesized with FCCVD method,³⁸¹ however, much higher discharge capacities of 2991 and 4237 mAh g_{carbon}^{-1} were achieved in carbonate (1 M LiPF₆ in PC/EC) and ether (1 M LiTFSI in 1,3-dioxolane/DME) based electrolytes, respectively, at a current density of 100 mA g_{carbon}^{-1} . Shui et al.⁴¹⁶ prepared some vertically aligned N-doped coral-like carbon fiber (VA-NCCF) arrays by CVD method, the VA-NCCF electrode demonstrated a discharge capacity as high as 40000 mAh $g_{\text{electrode}}^{-1}$ and ran stably for 150 cycles with a limited capacity of 1000 mAh $g_{\text{electrode}}^{-1}$ at a current density of 500 mA $g_{\text{electrode}}^{-1}$, the gap between the discharge and charge voltages at a current density of 100 mA $g_{\text{electrode}}^{-1}$ was only 0.3 V. The authors believed the special continuously coating layer of Li₂O₂ could fill up the entire interbranch space which would enhance the contact between the electrode and Li₂O₂ when compared to isolated individual particles, leading to a low overpotential. Nie et al.⁴¹⁷ reported the discharge voltage plateau of nitrogen-enriched mesoporous carbon prepared by the hard template method was 100 mV higher than that of BP 2000, and its discharge capacity of 4500 mAh g_{carbon}^{-1} could be achieved, which was about 1.73 times higher than that of the BP2000 cathode (2600 mAh g_{carbon}^{-1}) at a current density of 30 mA g_{carbon}^{-1} .

3.2 Metals and/or Metal oxides

Metals and/or metal oxides have been widely used in cathodes of Li-air batteries as catalysts to reduce the electrode overpotential during the charge-discharge process and improve the overall performance of the battery. To date, the studied metals and/or metal oxides as catalysts can be classified into: (1) precious metals and/or their oxides; (2)

manganese oxides; (3) transition metals and/or their oxides; and (4) perovskite and perovskite-related oxides.

3.2.1 Precious metals and/or their oxides

Precious metals and/or their oxides are generally considered to be the best catalysts for chemical reactions, no matter whether they are in industrial catalysis or electrocatalysis processes. However, the studies on precious metals and/or their oxides used in Li-air batteries are rarely reported, probably because of their expensive price and scarce reserves. Up to now, the main precious metals that have been investigated in cathode catalysis of Li-air batteries include Pt,^{67,105,107,110,418} Au,^{97,105,107,110,230,418} Pd,¹⁰⁷ Ru,^{107,368} and Ir⁴¹⁹.

Lu et al.^{105,107,109-111} have systematically investigated the roles of Pt and Au on ORR as well as OER in Li-air batteries. They found Pt nanoparticles were catalytically effective towards OER while Au nanoparticles were effective for ORR (Fig. 16). The electrode overpotentials of a Pt-Au nanoparticles hybrid catalyst supported on Vulcan XC-72 could be reduced by about 150-360 mV (discharge) and 900 mV (charge) when compared to those of a pure carbon electrode during the charge-discharge processes, respectively.¹¹⁰ Yin et al.⁴¹⁸ prepared PtAu/C catalysts with various compositions, alloying degrees and phase segregations by a modified two phase method followed by a thermal treatment under controlled conditions. They comparatively investigated their catalytic performance to Au/C and Pt/C catalysts in the cathode of non-aqueous Li-air batteries (Table 3). Different from Lu et al.,¹⁰⁵ they found the discharge voltage of Au/C was similar to or slightly lower than that of pure carbon while the discharge voltage of Pt/C was clearly higher than that for pure carbon. Moreover, it was also observed that both the loading and nanoscale structural characteristics including the catalyst's size, composition, alloying degree and phase segregation had significant effects on the catalytic performance. Increasing loading of Pt/C could lead to

improved discharge capacity, increased discharge voltage and decreased charge voltage. The particle size of Au/C could also influence the charge/discharge voltages and discharge capacity, and there was an optimal size for achieving improved performance. The fully and partially alloyed PtAu/C catalysts exhibited some increased discharge voltage and decreased charge voltage, leading to improved round-trip efficiency. In addition, the phase segregation like that in an Au-enriched shell/alloyed core PtAu/C catalyst tended to enlarge the difference between the charge and discharge voltages. Furthermore, fully and partially alloyed PtAu/C catalysts could display higher discharge capacities than that of the catalyst with phase segregation. Zhang et al.⁴²⁰ synthesized PtAu nanoparticles by pulse electrodeposition on carbon to make a cathode. Their comparative investigation found that the PtAu nanoparticles-based electrode exhibited a marked lower charge plateau and an apparently higher discharge capacity than the electrode fabricated with pure carbon without catalyst. Kim et al.⁴²¹ prepared carbon-supported Pt₃Co alloy nanoparticles with a diameter of 3 nm (Pt₃Co/KB), and an outstanding activity towards OER was observed. At a current density of 100 mA g_{carbon}⁻¹, the Pt₃Co/KB based electrode showed only 135 mV of overpotential while the Pt/KB, α -MnO₂/KB, and KB based electrodes showed overpotentials of 635, 1150, and 1085 mV, respectively. The authors believed that the enhanced performance should be associated with the reduced adsorption strength of LiO₂ on the outermost Pt catalytic sites. Meanwhile, the alloy catalyst could also impel the generation of amorphous Li₂O₂ around the catalyst, leading to easier decomposition during the recharge process. Similarly, a series of Vulcan XC-72 carbon supported Pt_xCo_y alloy nanoparticles (Pt₄Co/C, Pt₂Co/C, PtCo/C and PtCo₂/C) were prepared by Su et al. through a chemical reduction method. At a current density of 100 mA g⁻¹, the PtCo₂/C based electrode exhibited the highest discharge capacity of 3040 mAh g⁻¹, compared to those of 2000, 2300, 2500, 1197 and 965 mAh g⁻¹, respectively, for Pt₄Co/C,

Pt₂Co/C, PtCo/C, Pt/C and bare Vulcan XC-72 carbon based electrodes.⁴²² Lei et al.³⁴⁷ prepared Super P carbon supported nanostructured Pd catalyst (Pd/C) through atomic layer deposition (ALD) method (the samples obtained after 1, 3 and 10 cycles of Pd ALD were denoted as 1c-ALD Pd/C 3c-ALD Pd/C and 10c-ALD Pd/C, respectively) and used as the cathodes for Li-air battery. They found that the amount of Pd had a great influence on the discharge capacity as well as the OER activity. At a current density of 100 mA g_{carbon+catalyst}⁻¹, the 3c-ALD Pd/C electrode exhibited the highest discharge capacity of 6600 mAh g_{carbon+catalyst}⁻¹ and the 10c-ALD Pd/C electrode displayed the lowest charge voltage of 3.4 V. Sun et al.⁴²³ synthesized Ru nanocrystals supported on Super P by a surfactant assisting method, and the cathode with this catalyst exhibited an excellent performance, including a capacity as high as 9800 mAh g_{carbon}⁻¹, a charge-discharge voltage difference as low as 0.37 V and an outstanding cycleability up to 150 cycles with a curtaining capacity of 1000 mAh g_{carbon}⁻¹ at a current density of 200 mA g_{carbon}⁻¹ (Fig. 17). Ke et al.³⁵² synthesized Pt/C, Ir/C and Pt-Ir/C catalysts by ethylene glycol reduction method, and evaluated their performance as cathode catalysts in Li-air battery using a pure carbon electrode as the baseline for comparison. Although some slightly decreased discharge capacities were observed, all the three catalysts could apparently decrease the charge overpotential from that of the carbon electrode, and the discharge voltage was not affected. Among them, Pt-Ir/C demonstrated the lowest charge voltage plateau and the highest discharge capacity. Ko et al.⁴¹⁹ prepared various carbon-supported metal and metal-alloy (Pt, Pd, Ir, Ru, Pt-Pd, Pd-Ir and Pt-Ru) catalysts with an impregnation-reduction method, and used them as the cathode catalysts for Li-air batteries. They found the Ru catalyst showed the highest capacity and the lowest charge-discharge overpotential among the studied metal catalysts. The initial discharge capacities of Pt-Ru, Pt-Pd and Pd-Ir were observed to be 346, 153 and 135 mAh g_{electrode}⁻¹,

respectively, at 0.2 mA cm^{-2} . Therefore, they reported different metal alloy catalysts could generate different characteristic behaviors from those of the pure metal catalysts.

Other than precious metals and their alloyed catalysts, several precious metal oxides have also been investigated as cathode catalysts for Li-air batteries. Thapa et al.¹⁹³ employed the oxides of RuO_2 and Ir_2O_3 in the cathode, and the initial discharge capacities of 317 and 345 $\text{mAh g}_{\text{electrode}}^{-1}$ were observed, respectively, at a current density of 0.025 mA cm^{-2} , and the capacities were sustained at 330 and 354 $\text{mAh g}_{\text{electrode}}^{-1}$ at the fifth cycle, respectively.

3.2.2 Manganese oxides

As the most successful catalyst used in earlier studies on cathodes for Li-air batteries, manganese oxides could not only improve the round-trip efficiency of battery, but also increase the specific discharge capacity.^{83,94,134,196,214,291,424,425} In recent studies, manganese dioxide are usually used as a reference to screen highly-active catalysts and are also employed as cathode catalysts in the studies on cathode mechanisms⁹⁸ as well as electrolyte performance.^{211,267} Furthermore, manganese dioxide can also play an important role in the composite electrodes.^{426,427}

Ogasawara et al. introduced electrolytic manganese dioxide (EMD) into the cathode of Li-air batteries in 2006,⁸³ and then the same group comparatively investigated the performance of several manganese oxides as cathode catalysts, such as commercial EMD, both $\alpha\text{-MnO}_2$ and $\beta\text{-MnO}_2$ in bulk and nanowire forms (Fig. 18a), $\gamma\text{-MnO}_2$, $\lambda\text{-MnO}_2$, Mn_2O_3 , and Mn_3O_4 .⁹⁴ Among them, $\alpha\text{-MnO}_2$ nanowire could deliver the highest discharge capacity of 3000 $\text{mAh g}_{\text{carbon}}^{-1}$ at a current density of $70 \text{ mA g}_{\text{carbon}}^{-1}$ (Fig. 18b) with a discharge voltage at around 2.6 V and a charge voltage at about 4.0 V versus Li/Li^+ (Fig. 18c).⁹⁴ After that, a vast amount of researches have been conducted on manganese oxides as cathode catalysts in Li-air batteries.

Manganese oxides generally exist in many crystallographic forms, such as 1D tunnel, 2D layered structure, 3D spinel phase and so on. Some intensive studies in the published literature have proven the performance of electrochemical devices can be strongly affected by the crystalline phase and morphology of the manganese oxides used. As the most widely studied manganese oxides in Li-air batteries, MnO₂ in various crystalline phases and with diverse morphologies has been extensively evaluated as the cathode catalysts. For example, Oloniyo et al.⁴²⁸ synthesized α -, β - and γ -MnO₂ nanowires, α -MnO₂ nanorods, α -MnO₂ nanospheres and carbon-supported α -MnO₂ nanowires (α -MnO₂/C), and compared their performance as cathode catalysts in non-aqueous Li-air batteries. In the electrolyte of 1 M LiPF₆/PC, all the unsupported catalysts demonstrated similar discharge capacity of around 2000 mAh g_{electrode}⁻¹, while the carbon supported α -MnO₂ nanowires displayed a greatly promoted discharge capacity as high as 11000 mAh g_{electrode}⁻¹. In 1 M LiTFSI/TEGDME, however, the β -MnO₂ nanowires exhibited the highest discharge capacity of 2600 mAh g_{electrode}⁻¹, while the α -MnO₂/C only delivered a capacity less than 1300 mAh g_{electrode}⁻¹. The authors attributed the different capacities to the difference in the surface area as well as in the specific characteristics of the electrolyte used. Song et al.⁴²⁹ prepared α -MnO₂ with various morphologies of nanoparticles, nanotubes and nanowires. The electrodes delivered a similar discharge voltage plateau, but the α -MnO₂ nanowires displayed an apparently lower charge voltage plateau, a much higher discharge capacity of 11000 mAh g_{carbon}⁻¹ at a current density of 200 mA g_{carbon}⁻¹ and a super rate capability of 4500 mAh g_{carbon}⁻¹ at a current density of 5000 mA g_{carbon}⁻¹, while the capacities of the other electrodes were as low as about 1000 mAh g_{carbon}⁻¹ at 5000 mA g_{carbon}⁻¹. The authors believed the superior performance of α -MnO₂ nanowires should be mainly associated with their relatively large amount of Mn³⁺ exposed on the surface, suggesting the surface oxidation states could be the dominant factor impacting

the deposition mechanism of discharge products and ORR/OER catalyst performance. They claimed the surface modification in combination with nano-architecture tailoring should be an efficient strategy for achieving high-power Li-air batteries. Similarly, Park et al.³²³ compared the performance of α -MnO₂ nanowires and α -MnO₂ nanopowders as cathode catalysts for Li-air batteries. The former exhibited a discharge capacity of 511 mAh g⁻¹ compared to that of 273 mAh g⁻¹ for the latter at a current density of 10 mA cm⁻². However, Truong et al.⁴³⁰ observed single-crystalline α -MnO₂ nanotubes could exhibit a much better capacity retention than both α -MnO₂ nanowires and δ -MnO₂ nanosheets. They considered the higher crystalline and surface area of α -MnO₂ nanotubes should be the reason for the enhanced performance. In order to further improve the performance of MnO₂ as a cathode catalyst for Li-air batteries, some morphology/structure modifications as well as elemental substitutions have been developed and explored. For example, a hierarchically structured porous α -MnO₂ reported by Zeng et al.⁴³¹ exhibited a discharge capacity of 900 mAh g_{carbon+catalyst}⁻¹ at a current density of 0.1 mA cm⁻². A polythiophene mesoporous birnessite MnO₂ nanocomposite with a submicron-sphere/nanosheet hierarchical structure, prepared by Thapa et al.⁴³² using a modified inorganic/organic interfacial route, exhibited a discharge capacity of 345 mAh g⁻¹, a discharge voltage of 2.74 V and a charge voltage of 3.66 V at a current density of 0.13 mA cm⁻². Zahoor et al.⁴³³ synthesized α - and δ -MnO₂ with different morphologies like urchins and flowers, respectively, by a low temperature hydrothermal synthesis, and compared their performance in Li-air battery application. They found the α -MnO₂ electrode could deliver a discharge capacity as high as 6125.5 mAh g⁻¹ at a current density of 0.1 mA cm⁻² compared to that of 3674 mAh g⁻¹ for the δ -MnO₂ electrode. However, both of them were much higher than that of about 2200 mAh g⁻¹ for a pure KB electrode. Hu et al.⁴³⁴ demonstrated an electrode of sponge-like ϵ -MnO₂ could grow directly on Ni foam by

electrodeposition, and the formed electrode displayed a considerable high-rate capability (discharge capacity of 6300 mAh g_{catalyst}⁻¹ at a current density of 500 mA g_{catalyst}⁻¹) and an enhanced cycleability (exceeding 120 cycles) without controlling the discharge depth. The authors attributed the superior performance to the 3D nanoporous structures and abundant oxygen defects as well as the absence of side reactions related to carbon based conductive additives and binders. Zhang et al.⁴³⁵ showed that α -MnO₂ nanoneedle-based hollow microspheres displayed the discharge capacities of 1090, 700.0 and 203.9 mAh g⁻¹ at the current densities of 0.1, 0.2 and 0.5 mA cm⁻², respectively. Oh et al.^{436,448} prepared manganese oxide nanowires (MONW) using M13 virus as a template, the obtained MONW cathode showed a discharge capacity of 9196 mAh g_{carbon}⁻¹ at a current density of 400 mA g_{carbon}⁻¹ which was much higher than that of 6545 mAh g_{carbon}⁻¹ for manganese oxide nanoparticles (MONP). Moreover, the MONW cathode showed decreased discharge and charge overpotentials than the MONP electrode, the discharge voltage of MONW was about 2.68 V compared to that of 2.60 V for MONP, and the charge voltage of MONW was about 3.65 V compared to that of 3.77 V for MONP. Zhang et al.⁴³⁷ improved the reversibility of charge-discharge capacity from 34.1% to 100% using α -MnO₂ hollow clews prepared via a redox reaction of manganese sulphate and potassium permanganate instead of commercial EMD. Similarly, Jin et al.³²² prepared titanium containing γ -MnO₂ (TM) hollow nanospheres using titanium cations as the structure-directing agents. The obtained TM hollow nanospheres were composed of nano-flakes with an average thickness of about 15 nm, and there were also some broken lattice fringes corresponding to structural defects and distortion of γ -MnO₂. The Li-air battery with the TM nanospheres as cathode catalyst exhibited an average capacity of around 2182 mAh g_{carbon}⁻¹ at a current density of 0.15 mA cm⁻². Thapa et al.⁴³⁸ developed an ordered mesoporous β -MnO₂ with small microparticles of 0.1-0.3 μ m, the battery with this material as

cathode catalyst could attain a discharge capacity of $513 \text{ mAh g}_{\text{catalyst}}^{-1}$, a discharge voltage of 2.8-2.9 V and a charge voltage of 3.7 V at a current density of 0.025 mA cm^{-2} . Ida et al.²¹⁶ synthesized a card-house-like structured manganese oxide by exfoliating layered $\text{K}_{0.45}\text{MnO}_2$, the obtained catalyst displayed excellent activities towards both ORR and OER, the cathode with this material as catalyst exhibited a discharge voltage of 2.7-2.8 V, a charge voltage of 3.8 V and a discharge capacity of $1562 \text{ mAh g}_{\text{catalyst}}^{-1}$ at 0.05 mA cm^{-2} , which was about 4.7 times higher than that of EMD electrode. Trahey et al.⁴²⁵ fabricated a dual-functioning MnO_2 electrode with $\alpha\text{-MnO}_2$ /ramsdellite- MnO_2 , and a capacity of about $5000 \text{ mAh g}_{\text{electrode}}^{-1}$ with non-optimized air electrode was delivered at 0.024 mA cm^{-2} . It is worthwhile to note that the amount of MnO_2 used in the cathode has also been found to be one of the key factors determining the discharge capacity as well as the cycleability of Li-air batteries. For example, Chung et al.⁴²⁴ prepared the cathode with various contents of MnO_2 (5, 10 and 15 wt%, respectively) and found that the 15 wt%- MnO_2 electrode possessed the best capacity retention while the 5 wt%- MnO_2 electrode exhibited the highest capacity which might be attributed to the largest surface area.

Several other forms of manganese oxides different from MnO_2 have also been employed and studied as cathode catalysts in non-aqueous Li-air batteries. For example, Kavakli et al.⁴³⁹ showed nanosized Mn_3O_4 could give a higher discharge capacity than all the MnO_2 in α -, β - and δ - phase. Minowa et al.'s comparative evaluation⁴⁴⁰ found that Mn_2O_3 could exhibit a larger discharge capacity, a smaller charge-discharge potential difference and a better cycle-ability than both MnO and MnO_2 . In order to further improve the performance of Li-air batteries employing Mn_2O_3 as the cathode catalyst, the authors substituted the Mn site with several other transition metals to form doped catalysts of $\text{Mn}_{1.8}\text{M}_{0.2}\text{O}_3$ (M=Fe, Mn, Ni, Co) by an amorphous malate precursor method. The results showed a 20% substitution of Mn

with Fe could apparently improve the catalytic performance by increasing the discharge capacity and decreasing the charge-discharge overpotential, while those doped with Ni and Co would deteriorate the activity. The authors attributed the decreased performance of $\text{Mn}_{1.8}\text{Co}_{0.2}\text{O}_3$ and $\text{Mn}_{1.8}\text{Ni}_{0.2}\text{O}_3$ to the impurities while a pure $\text{Mn}_{1.8}\text{Fe}_{0.2}\text{O}_3$ phase was responsible for the enhanced activity. Furthermore, the authors optimized the Fe substitution content ($x=0, 0.2$ and 0.4 , respectively) and the calcination temperature (500 - 950 °C) of the $\text{Mn}_{2-x}\text{Fe}_x\text{O}_3$ catalyst, and found that the $\text{Mn}_{1.8}\text{Fe}_{0.2}\text{O}_3$ heat-treated at 500 °C had the best performance and comparatively most stable cycling characteristics with a capacity loss of 25% after 10 cycles.

In addition to MnO_x , another member of manganese oxides, γ - MnOOH , has also been investigated as a cathode catalyst in Li-air batteries. Zhang et al.⁴⁴¹ synthesized γ - MnOOH nanowires (MNWs) by a simple one-step hydrothermal method, and found a discharge voltage slightly higher than that of pure KB by about 30 mV and a charge voltage substantially lower (by 300 mV) than that of pure KB. Furthermore, significant improvements in discharge capacity, cycle stability as well as rate retention have also been achieved, and the authors attributed the entire enhancement to both the high catalytic efficiency and the high porosity in the cathode (Fig. 19).

3.2.3 Transition metals and/or their oxides

In addition to manganese oxides, several other transition metals and their oxides have also been widely studied as cathode catalysts in Li-air batteries and also demonstrated promising activity towards both ORR and OER.^{442,443} For example, Thapa et al.¹⁹³ investigated the performance of various metal oxides including Co_3O_4 , NiO, Fe_2O_3 , CuO, V_2O_5 , MoO_3 and Y_2O_3 as cathode catalysts for Li-air batteries. As listed in Table 4, all the metal oxides basically displayed improved discharge capacity after five cycles. V_2O_5 and CuO

demonstrated higher capacities than all the other oxide catalysts including MnO_2 after five cycles, while all the metal oxides can give good reversibility of the electrode reaction. However, the study by Barile et al.¹⁹¹ on CuO as a cathode catalyst for Li-air batteries with differential electrochemical mass spectrometry observed that CuO was detrimental to battery performance because it could catalyze solvent or carbon cathode decomposition as evidenced by CO_2 evolution. As for V_2O_5 , many researchers have also studied its performance as cathode catalysts for Li-air batteries. For example, the V_2O_5 cathode in Xiao et al.'s investigation³³⁷ delivered a discharge capacity of above 800 and 400 $\text{mAh g}_{\text{carbon+catalyst}}^{-1}$ at the current densities of 0.1 and 0.2 mA cm^{-2} , respectively. Lim et al.⁴⁴⁴ synthesized a Al_2O_3 -supported V_2O_5 catalyst via a wet impregnation method, the Li-air battery using this material as the cathode catalyst showed a lower charge overpotential and a higher discharge capacity than that with either carbon supported V_2O_5 or pure carbon cathodes, and the battery with a 50 wt% $\text{V}_2\text{O}_5/\text{Al}_2\text{O}_3$ electrode delivered a discharge capacity of 2875 $\text{mAh g}_{\text{carbon}}^{-1}$ at the first cycle and reached a maximum of 3250 $\text{mAh g}_{\text{carbon}}^{-1}$ at the second cycle at a current density of 100 $\text{mA g}_{\text{carbon}}^{-1}$.

Co_3O_4 is another transition metal oxide that has been widely studied as a cathode catalyst in Li-air batteries. Park et al.³⁸⁶ fabricated a cathode consisted of commercial Co_3O_4 , and a discharge capacity of nearly 2000 $\text{mAh g}_{\text{electrode}}^{-1}$ at 200 $\text{mA g}_{\text{electrode}}^{-1}$ was delivered, but only about 34% of the discharged capacity could be charged back in the voltage range from 2.35 to 4.35 V. Kim et al.⁴⁴⁵ investigated the performance of cube-type, flower-type and villiform-type Co_3O_4 nanoparticles. All three catalysts showed similar charge-discharge-voltage differences of about 1.6 V. Nevertheless, the influence of morphology on discharge performance was apparently observed. The villiform-type Co_3O_4 exhibited the highest discharge capacity of approximately 2900 $\text{mAh g}_{\text{carbon}}^{-1}$, while those of the flower-type and

cube-type Co_3O_4 were about 1800 and 2600 $\text{mAh g}_{\text{carbon}}^{-1}$, respectively, at a current density of 0.4 mA cm^{-2} . Moreover, both the villiform-type and cube-type nanoparticles maintained their shape while the flower-type particles broke into nanorod type during the discharge process. Riaz et al.⁴⁴⁶ prepared Co_3O_4 -only electrodes with morphologies of nanosheets, nanoneedles and nanoflowers via an electrodeposition-conversion process, and found the performance was strongly dependent on the architecture of the Co_3O_4 cathode. The discharge capacity was increased in keeping with the order of nanosheets ($1127 \text{ mAh g}_{\text{catalyst}}^{-1}$) < nanoflowers ($1930 \text{ mAh g}_{\text{catalyst}}^{-1}$) < nanoneedle ($2280 \text{ mAh g}_{\text{catalyst}}^{-1}$) at a current density of $20 \text{ mA g}_{\text{catalyst}}^{-1}$. It was also observed that among the three catalysts, the nanoneedles Co_3O_4 electrode had the best long-term cycleability, although all three catalysts had closely similar discharge voltage of about 2.75 V and charge voltage as low as 3.85 V vs. Li/Li^+ (Fig. 20). Ming et al.⁴⁴⁷ fabricated a dense hollow porous Co_3O_4 electrode and thus achieved an obvious performance improvement when compared to those of both mesoporous Co_3O_4 and Co_3O_4 nanoparticles. The hollow porous Co_3O_4 cathode exhibited a low charge potential of about 4.0 V, a high discharge voltage of about 2.74 V and good cycle-ability greater than 100 cycles with a fixed capacity of $2000 \text{ mAh g}_{\text{catalyst}}^{-1}$ at $200 \text{ mA g}_{\text{catalyst}}^{-1}$. Cui et al.²⁸⁵ prepared a carbon-free electrode with free-standing type Co_3O_4 catalyst directly on nickel foam ($\text{Co}_3\text{O}_4@\text{Ni}$), the resulting cathode showed a higher discharge voltage (2.95 V), a lower charge voltage (3.44 V), a higher specific capacity ($4000 \text{ mAh g}_{\text{electrode}}^{-1}$) and less capacity fading than the conventional carbon supported cathode. In Zhao et al.'s study, they also fabricated a carbon-free $\text{Co}_3\text{O}_4@\text{Ni}$ electrode by electroplating directly the hierarchical porous Co_3O_4 film with free-standing hollowed flakes on Ni foam and then calcined at various temperatures in Ar atmosphere. The performance of the Li-air battery with the Co_3O_4 film as cathode catalyst demonstrated apparent calcination temperature dependence. The film calcined at $300 \text{ }^\circ\text{C}$

exhibited the highest discharge capacity of 2460 mAh $g_{\text{electrode}}^{-1}$ at a current density of 200 mA $g_{\text{electrode}}^{-1}$ while capacities of about 2000, 700 and 450 mAh $g_{\text{electrode}}^{-1}$ were displayed for the films calcined at 250, 350 and 450 °C, respectively.⁴⁴⁸ Anandan et al.⁴⁴⁹ partially substituted Co in Co_3O_4 with Mn, and prepared the catalysts of $\text{Mn}_{0.5}\text{Co}_{2.5}\text{O}_4$, MnCo_2O_4 and $\text{Mn}_{1.5}\text{Co}_{1.5}\text{O}_4$ to be used in the cathode of the Li-air battery. In battery testing, all three catalysts exhibited the same discharge voltages and slightly lower discharge capacities than the Co_3O_4 catalyst. However, their recharge voltages were apparently lower than that of the Co_3O_4 catalyst. In addition, another substituted Co_3O_4 , namely NiCo_2O_4 , was also studied by many researchers as a cathode catalyst for Li-air batteries. The mesoporous NiCo_2O_4 nanoflakes exhibited much higher ORR onset potential (2.9 V) and discharge capacity (1560 mAh g_{carbon}^{-1}) and much lower recharge overpotential when compared to those of the pure carbon cathode.²⁸⁶ Similarly, the hierarchical NiCo_2O_4 nanorods-based cathode delivered discharge capacities of 13250 and 5700 mAh g_{carbon}^{-1} at the current densities of 200 and 1000 mA g_{carbon}^{-1} , respectively,²⁸³ which were much higher than that of the carbon black electrode. Meanwhile, this hierarchical NiCo_2O_4 nanorods-based cathode also displayed lower charge over-potential and better cycling stability than the carbon black electrode. In Li et al.'s study,⁴⁵⁰ some ordered mesoporous NiCo_2O_4 using KIT-6 as the hard template was synthesized, and the effects of NiCo_2O_4 amount on the battery performance was comparatively studied. They found the cathodes with a NiCo_2O_4 amount of 20%, 45% and 70% could display discharge capacities of 4357, 4120 and 1881 mAh $g_{\text{carbon+catalyst}}^{-1}$, respectively, at a current density of 0.1 mA cm^{-2} . Besides, the charge voltages of these cathodes could also be influenced by the amount of NiCo_2O_4 . It could be decreased from about 4.0 V to 3.75 V when the content of NiCo_2O_4 was increased from 20% to 70%, while the discharge voltage plateaus exhibited similarly at about 2.75-2.80 V. The electrode with 45 wt% of NiCo_2O_4

gave a terminal voltage as high as 2.4 V after 20 cycles under a limited discharge capacity of 1000 mAh $\text{g}_{\text{carbon+catalyst}}^{-1}$, while it was decreased to 2.0 V at 12 cycles for pure KB EC600JD electrode.

As a special member of transition metal oxides, iron oxyhydroxide of β -FeOOH has also been studied as a cathode catalyst in Li-air batteries. Jung et al.⁴⁵¹ prepared β -FeOOH nanorod by ultrasonic-irradiated chemical synthesis, the resulting cathode with this material as catalyst delivered a high discharge capacity of 7183 mAh $\text{g}_{\text{carbon}}^{-1}$ along with a promoted round-trip efficiency of 74.8% which was higher than 62.5% for the pure carbon electrode. This oxide also had a lower charge potential for oxygen evolution from Li_2O_2 than pure carbon. The authors attributed the enhanced performance to the high fraction of surface defect active sites in the metallic oxide and its unique morphology and variable oxygen stoichiometry in this material.

3.2.4 Perovskite and Perovskite-related oxides

The representative crystal structure of perovskite oxide with the archetypal formula of ABO_3 is shown in Fig. 21a as cubic.^{452,453} The larger A cations and the oxygen form a face-centered cubic (*fcc*) lattice while the B cations occupy octahedral sites in this *fcc* lattice and are surrounded only by nearest oxygen neighbors. These B cations share corners with each other facing with the dodecahedra surrounding the A cations. The A and B cations are shielded from one another by the oxygen ions. Perovskite and perovskite-related oxides have been widely used in solid-oxide fuel cell (SOFC),⁴⁵⁴⁻⁴⁵⁷ superconductors^{458,459} and semiconductor-based gas sensors.⁴⁶⁰ These oxides generally have good catalytic activity towards both ORR and OER at high temperature⁴⁶¹ or in aqueous systems especially in alkaline conditions for low temperature metal-air batteries^{108,462-469}. In recent years, perovskite oxides have also attracted much attention in non-aqueous Li-air batteries to

facilitate the kinetics of ORR as well as OER.^{108,312,470-475}

Fu et al.⁴⁷² prepared nano-sized perovskite oxides of g-La_{0.8}Sr_{0.2}MnO₃ and s-La_{0.8}Sr_{0.2}MnO₃ with high purity by sol-gel and solid-state reaction method, respectively, and made a scrutiny into Li-air batteries as cathode catalysts. The battery with g-La_{0.8}Sr_{0.2}MnO₃ demonstrated a discharge capacity of 1900 mAh g_{carbon}⁻¹ at a current density of 0.1 mA cm⁻², compared to 1200 mAh g_{carbon}⁻¹ for the battery with s-La_{0.8}Sr_{0.2}MnO₃. Moreover, the discharge voltage of g-La_{0.8}Sr_{0.2}MnO₃ was 0.2 V higher than that of s-La_{0.8}Sr_{0.2}MnO₃. The authors assumed the surface morphology of the nanostructures might be the major factor enhancing the electrochemical property of the cathode materials. Xu et al.³¹² prepared perovskite-based porous La_{0.75}Sr_{0.25}MnO₃ (PNT-LSM) nanotubes with the electrospinning technique followed by heat treatment at high temperature and studied its performance as a cathode catalyst in non-aqueous Li-air batteries. Compared to the pure carbon cathode, the as-prepared La_{0.75}Sr_{0.25}MnO₃ nanotubes could significantly suppress the ORR and especially OER overpotentials and thus improved the round-trip efficiency. Furthermore, the synergistic effect of the high catalytic activity and the unique hollow channel structure of the PNT-LSM catalyst facilitated the battery with a high specific capacity, superior rate capability and good cycle stability (Fig. 22). Zhao et al.⁴⁷³ synthesized hierarchical mesoporous perovskite La_{0.5}Sr_{0.5}CoO_{2.91} nanowires with a facile multistep microemulsion followed by a slow annealing method. The cathode with this material as catalyst displayed a capacity of 11059 mAh g_{catalyst+carbon}⁻¹ at a current density of 50 mA g_{catalyst+carbon}⁻¹. Kalubarme et al.⁴⁷⁶ prepared some nickel-doped lanthanum cobaltite perovskite oxides of LaNi_xCo_{1-x}O_{3-δ} (x=0, 0.25, 0.5, 0.75 and 1) by a solution combustion method, and studied their catalytic activity for Li₂O₂ oxidation in Li-air batteries. Among the studied catalysts, LaNi_{0.25}Co_{0.75}O₃ exhibited the best performance with its lowest charge voltage of 3.76 V and highest discharge capacity of 7720

mAh $g_{\text{electrode}}^{-1}$. The authors presumed that the synergistic effect of the fast kinetics of electron transport provided by the carbon support and the high electro-catalytic activity of the perovskite oxide should be the major contributor to the excellent performance of $\text{LaNi}_{0.25}\text{Co}_{0.75}\text{O}_3$. Yuasa et al.⁴⁷⁷ presented that the carbon-supported $\text{LaMn}_{0.6}\text{Fe}_{0.4}\text{O}_3$ nanoparticles prepared via a reverse homogeneous precipitation method exhibited a discharge capacity of about 200 mAh $g_{\text{electrode}}^{-1}$ at a current density of 0.5 mA cm^{-2} . Meng et al.^{478,489} prepared Ce-incorporated $\text{LaFe}_{0.5}\text{Mn}_{0.5}\text{O}_3$ catalysts with the increasing Ce/(La+Ce) ratios (0, 0.05, 0.1 and 0.5) with both co-precipitation (CP) and micro-emulsion (ME) methods, and used them as catalysts in a cathode of Li-air batteries. They found Ce had a low solubility in $\text{LaFe}_{0.5}\text{Mn}_{0.5}\text{O}_3$ perovskite lattices and the as-prepared materials actually formed as $\text{LaFe}_{0.5}\text{Mn}_{0.5}\text{O}_3\text{-CeO}_2$ composite. The order of discharge capacity with respect to the Ce/(La+Ce) ratio is that of 0.05 > 0.1 > 0.5 > 0 regardless of the preparation method. The results also indicated the catalyst prepared with the CP method could deliver higher capacity than that with the ME method at a specific Ce content, and a highest discharge capacity of about 4700 mAh g_{carbon}^{-1} and a discharge voltage of 2.75 V could be obtained by the CP-prepared composite catalyst with a Ce content of 0.05 at a current density of 100 mA g_{carbon}^{-1} . The authors attributed the increased capacity to the enhanced oxygen storage/release capability and the increased conductivity with the incorporation of CeO_2 . Jin et al.⁴⁷⁹ found that the $\text{Ba}_{0.9}\text{Co}_{0.5}\text{Fe}_{0.4}\text{Nb}_{0.1}\text{O}_3$ perovskite oxide electrode delivered a discharge capacity of 1235 mAh $g_{\text{electrode}}^{-1}$ in a dry gas mixture composed of 80 vol.% pure N_2 and 20 vol.% pure O_2 at a current density of 50 mA $g_{\text{electrode}}^{-1}$. Han et al.⁴⁸⁰ investigated the porous perovskite CaMnO_3 synthesized by a citric acid assisted sol-gel route and used it as a cathode catalyst for Li-air batteries. The CaMnO_3 electrode presented a discharge-recharge voltage gap of 0.98 V which was about 620 mV lower than that of the pure carbon cathode with a controlled

discharge depth of 500 mAh g_{carbon}⁻¹ at a current density of 50 mA g_{carbon}⁻¹. In addition, a stable cycleability over 80 cycles with a discharge plateau higher than 2.35 V was observed while the pure carbon electrode could merely sustain less than 25 cycles at a current density of 100 mA g_{carbon}⁻¹ with a controlled discharge capacity of 500 mAh g_{carbon}⁻¹.

Furthermore, Oh et al.¹⁸⁹ synthesized metallic mesoporous pyrochlore, lead ruthenate, and the nanocrystalline expanded pyrochlores by using liquid-crystal templating and subsequent oxidation, and used them as catalysts in a cathode of Li-air batteries. The results showed the metallic mesoporous pyrochlore could form a high-performance cathode with reversible capacity up to 10400 mAh g_{carbon}⁻¹, which was much higher than that of 6920 mAh g_{carbon}⁻¹ for the nanocrystalline expanded pyrochlores electrode at a current density of 70 mA g_{carbon}⁻¹. The authors attributed the ultrahigh capacity of mesoporous pyrochlore to its tailored properties, which were vital to catalytic reactions, including a high fraction of exposed oxygen vacancies, porosity that enabled good diffusion to the active sites, and a nanoscale conductive network with metallic conductivity.

Although perovskite oxides have attracted certain attention for incorporation into Li-air batteries, the effects by partial substitution in both cation sublattices have not been comparatively studied and the mechanisms are still unclear. Furthermore, the perovskite-related oxides other than ABO₃, such as double perovskite oxides (A₂B₂O₆, as seen in Fig. 21b)⁴⁸¹ and layered perovskite oxides (Fig. 21c)⁴⁸²⁻⁴⁸⁸ have rarely been investigated as cathode catalysts in Li-air batteries. Therefore, much more systematic research on perovskite-type catalysts should be conducted in detail in the future to improve the catalytic performance towards ORR as well as OER and to promote the development of Li-air batteries⁴⁸⁹.

3.2.5 Other metals and their metal oxides

In addition to the metals and metal oxides discussed above, there are still some other

metals and their metal oxides which could also demonstrate good properties as catalysts of the cathode in Li-air batteries.^{102,490} For example, Kalubarme et al.⁴⁹⁰ prepared ceria based catalysts of $\text{Ce}_{1-x}\text{Zr}_x\text{O}_2$ ($x=0-0.5$) by a solution combustion technique, the $\text{Ce}_{0.8}\text{Zr}_{0.2}\text{O}_2$ -based cathode could attain a maximum discharge capacity of $1620 \text{ mAh g}_{\text{carbon}}^{-1}$ at a current density of $80 \text{ mA g}_{\text{carbon}}^{-1}$ due to its high surface area and porosity. An improvement of approximately 12% in discharge capacity was also achieved on the electrode with 50 wt% $\text{Ce}_{0.8}\text{Zr}_{0.2}\text{O}_2$ and 50 wt% MnO_2 .

Lithium-containing binary or ternary metal oxides have also been used as cathode catalysts in Li-air batteries. For example, Trahey et al.¹⁰² prepared Li_5FeO_4 (by heat-treating the mixture of $\text{LiOH}\cdot\text{H}_2\text{O}$ and nanosized Fe_2O_3) and $\text{Li}_2\text{MnO}_3\cdot\text{LiFeO}_2$ (by sol-gel method with the lithium-, manganese- and iron acetates as precursors). They found the Li_5FeO_4 and $\text{Li}_2\text{MnO}_3\cdot\text{LiFeO}_2$, as cathode catalysts in Li-air batteries, could be electrochemically or chemically activated by acid-treatment to remove Li_2O . The activated Li_5FeO_4 and $\text{Li}_2\text{MnO}_3\cdot\text{LiFeO}_2$ electrodes could provide discharge capacities of 2680 and 2516 $\text{mAh g}_{\text{carbon}}^{-1}$, respectively, at a current density of $70 \text{ mA g}_{\text{carbon}}^{-1}$.

3.3 Composite materials

As discussed above, the insoluble discharge products are generally deposited in the pores of the cathode in Li-air batteries. Therefore, the cathode materials must have a large surface area and huge porous volume to store more discharge products. Moreover, improving energy efficiency of the battery requires a catalyst not only effective to ORR but also efficient towards OER. Unfortunately, it is difficult to have any mono-material that can meet all these requirements completely. Therefore, hybrid electrodes with composite materials have become a trend to improve the performance of Li-air batteries.⁴⁹¹

Metal and their oxides hybridized with functional carbon materials seem to be good choices to meet the requirements of cathode materials for Li-air batteries.⁴⁹² The functional carbon material plays an important role in the composite. It can not only provide a high surface area for storing the discharge products, but also facilitates the dispersion of catalyst particles on the surface to enhance their catalytic performance. Furthermore, it has some intrinsic catalytic activity towards the cathode reactions because of the vacancies and defects.

As a type of superior functional carbon material, graphene is widely used for hybrid electrodes with metals or metal oxides. Yang et al.³⁵³ prepared a hybrid electrode of highly dispersed platinum nanoparticle-graphene nanosheets (PtNP-GNSs) by liquid phase pulsed laser ablation, and a discharge capacity of about 4820 mAh g_{electrode}⁻¹ was obtained at 70 mA g_{electrode}⁻¹. It was discussed that the ORR proceeded at two different types of catalytic active sites induced by Pt nanoparticles and GNSs, leading to two discharge voltage plateaus at 2.88 V and 2.52 V, respectively, and the average charge voltage was at 4.07 V. In a similar study by Wang et al.³⁷⁰ on PtNP-GNSs prepared by ethylene glycol reduction using H₂PtCl₆ as Pt precursor, a much lower charge voltage of 3.58 V was demonstrated. Jung et al.³⁶⁸ showed the Ru-rGO and RuO₂·0.64H₂O-rGO synthesized by depositing metallic ruthenium and hydrated ruthenium oxide, respectively, on reduced graphene oxide (rGO) could significantly reduce the average charge potential of 4.3 V for rGO to about 3.9 and 3.7 V at 500 mA g_{electrode}⁻¹ under the capacity-controlled regimes of 5000 mAh g_{electrode}⁻¹ (Fig. 23). The covalently coupled MnCo₂O₄-graphene hybrid prepared by reducing the mixture of graphene oxide and Mn(OAc)₂ and Co(OAc)₂ via solvothermal method⁴⁹¹ displayed a discharge voltage as high as 2.95 V and a charge voltage as low as 3.75 V at a current density of 100 mA g_{catalyst}⁻¹, which was among the lowest overpotentials (similar to a Pt/C catalyst) reported so far using the similar electrolyte at comparable gravimetric current density. The MnCo₂O₄-

graphene hybrid also demonstrated a better cycle-ability than Pt/C as the cathode catalyst. Cao et al.⁴⁹³ synthesized α -MnO₂ nanorods on graphene via the redox reaction, and showed that the α -MnO₂/GNSs exhibited a discharge capacity of 11520 mAh g_{carbon}⁻¹ at a current density of 200 mA g_{carbon}⁻¹, which was much higher than 7200 mAh g_{carbon}⁻¹ for α -MnO₂ and GNSs mixture. Kalubarme et al.⁴⁹⁴ also found that the MnO₂/GNSs composite obtained by solvothermal oxidation of the Mn-precursor on a graphene surface could give enhanced discharge capacity, promoted oxygen reduction, and accelerated Li₂O₂ oxidation when compared to the pristine GNSs. Yang et al.⁴²⁶ studied the MnO₂-GNSs composite prepared by mixing aqueous GNSs colloids and aqueous MnO₂ dispersions, with a MnO₂ ratio of 30, 50 and 70 wt%, as cathode materials for Li-air batteries. The 30 wt% MnO₂-GNSs electrode exhibited the highest discharge capacity of 11235 mAh g_{electrode}⁻¹ at a current density of 75 mA g_{electrode}⁻¹, which were much higher than 9719, 7723 and 4852 mAh g_{electrode}⁻¹ for pure GNSs, 50 wt% and 70 wt% MnO₂-GNSs electrodes, respectively. In addition, the 30 wt% MnO₂-GNSs electrode also demonstrated a slightly higher discharge voltage (2.55 vs. 2.51 V) and an apparently lower charge voltage (3.95 vs. 4.25 V) than the GNS electrode, indicating its better catalytic performance towards ORR especially OER. Ryu et al.⁴⁹⁵ immobilized Co₃O₄ nanofibers onto nonoxidized graphene nanoflakes and the obtained cathode exhibited a large discharge capacity of 10500 mAh g_{electrode}⁻¹ at a current density of 200 mA g_{electrode}⁻¹ and also run stably for about 80 cycles with a limited capacity of 1000 mAh g_{electrode}⁻¹. Zhang et al.⁴⁹⁶ prepared some Fe₂O₃ nanocluster-decorated graphene cathodes, and found that the Fe₂O₃/graphene hybrid electrodes with 10.7, 29.0 and 52.1 wt% of Fe₂O₃ could deliver discharge capacities of 6420, 8290 and 7920 mAh g_{carbon}⁻¹, respectively, which were all higher than 5100 mAh g_{carbon}⁻¹ for the pure graphene electrode at 100 mA g_{carbon}⁻¹. Wang et al.³⁷⁰ mixed La_{0.5}Ce_{0.5}Fe_{0.5}Mn_{0.5}O₃ and GNSs during the cathode slurry preparation, and

observed that this cathode could give a discharge capacity of 1200 mAh $\text{g}_{\text{carbon+catalyst}}^{-1}$ at a stable nominal discharge voltage of 2.8 V and a charge voltage of 3.8 V at a current density of 50 mA $\text{g}_{\text{carbon+catalyst}}^{-1}$. This cathode also exhibited 100 cycles with a charge voltage less than 4 V and with a total efficiency of about 70%. Ahn et al.⁴⁹⁷ investigated the zirconium doped ceria and graphene mixture (ZDC/GNSs) as catalyst for oxygen reduction in non-aqueous Li-air batteries. The ZDC/GNSs electrodes containing ZDC weight contents of 5%, 10%, 20%, 30% and 40% achieved capacities of 2751, 3254, 3159, 2179 and 2109 mAh $\text{g}_{\text{electrode}}^{-1}$, respectively, which were all higher than 996 mAh $\text{g}_{\text{electrode}}^{-1}$ for the bare GNSs electrode. The authors assumed the excellent performance of this blend catalyst could be attributed to the fast kinetics of electron transport provided by both the graphene support and the high electro-catalytic activity provided by the ZDC. Selvaraj et al.⁴⁹⁸ showed a reduced graphene oxide-polypyrrole composite (rGO-PPy) could deliver a discharge capacity of 3358 mAh g^{-1} at a current density of 0.3 mA cm^{-2} and the gap between discharge and charge voltages was 1.06 V which was greatly lower than that of 1.41 V for the pure reduced graphene oxide (rGO) at the capacity of 50 mAh g^{-1} .

In addition to graphene, many other functional carbon materials also play an important role in composite cathode materials. San et al.'s study with first-principle theory⁴⁹⁹ indicated a Pt-doped CNTs had a higher catalytic activity towards ORR than both N-doped CNTs and Pt-adsorbed CNTs, and increasing the concentrations of Pt doping could enhance its catalytic activity towards ORR. Shen et al.³⁸⁰ reported a Pd coated CNTs sponge (Pd-CNTs) cathode synthesized by electrochemical deposition of Pd on the CNTs sponge delivered a capacity as high as 9092 mAh $\text{g}_{\text{electrode}}^{-1}$ and a discharge voltage of 2.65 V at a current density of 0.05 mA cm^{-2} . In Li et al.'s study, they prepared a Ru/MWCNT/P catalyst via a wet chemical method, and found that this catalyst could decrease the charge voltage by about 0.68 V compared to

the pure MWCNT electrode.⁵⁰⁰ Yilmaz et al.⁵⁰¹ found that the ruthenium oxide nanoparticles dispersed on multiwalled carbon nanotubes (RuO₂/MWCNTs) prepared by solvothermal method could display a recharge voltage of 3.48 V which is lower than 3.91 V for pure MWCNTs at a current density of 0.05 mA cm⁻², although it exhibited a similar discharge voltage (about 2.68 V) and slightly lower discharge capacity (around 1800 mAh g_{carbon}⁻¹) when compared to pure MWCNTs with a discharge cut-off voltage at 2.4 V. The authors considered that the RuO₂ nanoparticles could promote the coating of poorly crystalline lithium peroxide on MWCNTs, and make it easy for lithium peroxide to decompose at low potential, indicated by that only large Li₂O₂ particles could be formed on the pure MWCNTs. Similarly, Jian et al.⁵⁰² found the core-shell-structured RuO₂@CNT composite prepared by sol-gel method could display a very good performance in Li-air batteries. Compared to the gap between the discharge and charge voltages of 1.81 V which was corresponding to a round-trip efficiency of 59% for pure CNT cathode, the RuO₂@CNT composite electrode exhibited a voltage difference of 0.72 V and a round-trip efficiency of 79% at a current density of 385 mA g_{carbon}⁻¹. Furthermore, the RuO₂@CNT composite cathode could deliver a discharge capacity of 4350 mAh g_{carbon}⁻¹ which was much higher than 3258 mAh g_{carbon}⁻¹ for the pristine CNTs. The discharge and charge voltages of this RuO₂@CNT composite cathode were 0.11 V higher and 0.98 V lower than those of the pristine CNTs, respectively, indicating its promoting effect on both ORR and OER. The NiO/MWCNTs electrode prepared by a chemical bath deposition displayed a much higher discharge voltage and drastically lower charge voltage than the MWCNTs cathode.³⁴⁶³⁴⁶ Eom et al.⁵⁰³ prepared MnO₂/MWCNTs nanocomposites electrode by hydrothermal method, and a discharge capacity of 3428 mAh g_{carbon}⁻¹ was delivered with a cut-off voltage at 2.3 V at a current density of 0.2 mA cm⁻². Yoon et al.³⁷⁹ showed that the charge voltage of Co₃O₄/CNTs

prepared by a hydrothermal method displayed at a much lower value than the pure CNTs cathode, although their discharge voltages were closely similar to each other. Zhang et al.²⁹² reported the composite cathode of α -MnO₂/CNTs/CNFs prepared by filtering the mixed suspension of α -MnO₂, CNTs, and CNFs could give much lower charge voltage and improved cyclability than the cathode without α -MnO₂. Etacheri et al.²⁰³ showed α -MnO₂/ACM hybrid prepared by electrodepositing α -MnO₂ on ACM exhibited a higher discharge capacity of 9000 mAh g_{carbon}⁻¹ which was much higher than 4116 mAh g_{carbon}⁻¹ for the ACM cathode. A lower charge voltage of 3.75V compared to that of 4.3 V for the ACM electrode at a current density of 0.025 mA cm⁻² was also observed. The authors attributed the promoted performance to the extremely high surface area, hierarchical microstructure and efficient ORR catalysis of α -MnO₂ nanoparticles. Huang et al.⁵⁰⁴ reported the nanofibrous MnNi/CNFs, a composite prepared via electrospinning technique followed by a carbonization process using polyacrylonitrile (PAN), manganese acetate and nickel acetate as raw materials, displayed a discharge capacity of 3850 mAh g⁻¹ and a discharge voltage plateau of 2.71 V at 0.1 mA cm⁻², which were much better than the pristine CNFs cathode. Sun et al.³³⁸ reported the CoO/CMK-3 composite prepared by the wet impregnation method could give a much lower ΔV than that of the only CMK-3 electrode since CMK-3 carbon might facilitate the diffusion of oxygen while the CoO nanoparticles could significantly reduce the charge overpotential. The authors also found the CoO/Super-P electrode showed a much lower charge overpotential than that of an only Super-P electrode. Park et al.³⁸⁶ reported the carbon-sphere/Co₃O₄ prepared by calcinating the mixture of cobalt nitrate and carbon spheres in N₂ atmosphere exhibited a slightly lower discharge capacity than the pure carbon sphere electrode, but its discharge and charge voltages were much higher and lower, respectively, than that of both the carbon sphere and commercial Co₃O₄ nanopowders. The discharge

capacities of carbon-sphere/ Co_3O_4 electrodes achieved at 7000, 3400 and 2100 $\text{mAh g}_{\text{electrode}}^{-1}$ at current densities of 100, 200 and 400 $\text{mA g}_{\text{electrode}}^{-1}$, respectively. In another paper,⁵⁰⁵ it was found the $\text{Co}_3\text{O}_4/\text{RuO}_2/\text{carbon-sphere}$ nanocomposite prepared by the same method could deliver higher discharge capacity and voltage, lower charge voltage and better cycleability than the KB cathode, and its discharge capacities could achieve about 6600, 4000 and 2900 $\text{mAh g}_{\text{electrode}}^{-1}$ at the current densities of 200, 400 and 600 $\text{mA g}_{\text{electrode}}^{-1}$, respectively. The porous carbon supported core-shelled $\text{Fe}_3\text{O}_4/\text{Fe}$ nanocomposite prepared by a wet-chemistry approach displayed a discharge voltage at 2.73 V and a total specific capacity of about 4000 $\text{mAh g}_{\text{carbon+catalyst}}^{-1}$ with the voltage cut-off at 2.3 V at a current density of 100 $\text{mA g}_{\text{carbon+catalyst}}^{-1}$, which were much better results than those of the bare carbon cathode and the electrode made from mechanically milled same carbon and pre-synthesized $\text{Fe}_3\text{O}_4/\text{Fe}$.⁵⁰⁶ Wu et al.⁵⁰⁷ prepared the porous iron-carbon based nanofiber catalyst by electrospinning method, and found that this catalyst exhibited a higher ORR onset potential when compared to both glassy carbon and Pt disk electrodes in O_2 -saturated 1.0 M LiPF_6 in TEGDME. Liu et al.²⁹³ prepared 3D NiCo_2O_4 nanowire array/carbon cloth (NCONW/CC) by solvothermal method followed by calcination process and integrated it into Li-air batteries as the cathode catalyst. The NCONW/CC electrode displayed a discharge capacity of 980 $\text{mAh g}_{\text{catalyst}}^{-1}$ at 18 $\text{mA g}_{\text{catalyst}}^{-1}$ which was much higher than 500 $\text{mAh g}_{\text{carbon}}^{-1}$ for pure carbon cloth electrode, although they could deliver the same discharge and charge voltages at about 2.6 V and 4.2 V, respectively. The discharge capacities of such an electrode could be attained at 1577 and 730 $\text{mAh g}_{\text{catalyst}}^{-1}$ at the current densities of 4 and 150 $\text{mA g}_{\text{catalyst}}^{-1}$, respectively.

The composite materials hybridized by metals and metal oxides also exhibit excellent capability as cathode materials of Li-air batteries.^{418,427,508-510} For example, Thapa et al. mixed Pd with mesoporous $\alpha\text{-MnO}_2$ ⁵⁰⁸ and achieved a higher discharge capacity (545 vs. 365 mAh

g_{catalyst}^{-1}) and lower charge/discharge voltages difference (0.6 vs. 0.8 V) than the cathode with only mesoporous α -MnO₂ at a current density of 0.025 mA cm⁻². Similarly, they also dispersed a small amount of Pd on ordered mesoporous β -MnO₂⁴³⁸ and achieved a capacity promotion (817 vs. 513 mAh g_{catalyst}^{-1}) and also a charge potential decrease (3.6 vs. 3.7 V) compared to the mesoporous β -MnO₂ only cathode. The Pd/EMD-PTFE-coated acetylene black electrode exhibited a discharge capacity of 257 mAh g⁻¹ repeatedly for over 20 cycles¹⁹³. The authors also synthesized Pd and Au/Pd nanoparticles loaded mesoporous β -MnO₂ (Pd/ β -MnO₂ and Au/Pd/ β -MnO₂) with hydrothermal process using a silica KIT-6 template, and used as catalysts in Li-air battery. At the current density of 0.13 mA cm⁻², the Pd/ β -MnO₂ electrode displayed a discharge capacity of 576 mAh $g_{\text{electrode}}^{-1}$ and a discharge voltage of 2.7-2.9 V, while the Au/Pd/ β -MnO₂ electrode exhibited a significantly higher discharge capacity of 775 mAh $g_{\text{electrode}}^{-1}$ and recycled with a stable charge/discharge capacity of 714 mAh $g_{\text{electrode}}^{-1}$ for 12 times in the voltage range from 2.0 to 4.0 V. When the current density was increased to 0.63, 1.91, and 2.55 mA cm⁻², respectively, the discharge capacities could reach at 545, 259, 169 mAh $g_{\text{electrode}}^{-1}$. With these results, the authors discussed that loading of Au-Pd nanoparticles on the mesoporous β -MnO₂ was effective for decreasing the charge potential to its theoretical value.²¹⁷ Thapa et al.⁴³² found the electrode with a small amount of Pd dispersed on polythiophene mesoporous birnessite MnO₂ showed a discharge capacity of 487 mAh g⁻¹, a discharge voltage at 2.71 V and a charge voltage at 3.58 V at a current density of 0.13 mA cm⁻², all of which were much better than those without Pd particles. Zhang et al.⁴³⁵ showed α -MnO₂ nanoneedle-based hollow microspheres coated with Pd nanoparticles exhibited higher discharge capacity and voltage, lower charge voltage and better cyclability than the cathode without Pd. Discharge capacities of 1220, 921.4 and 419.3 mAh g⁻¹ at current densities of 0.1, 0.2 and 0.5 mA cm⁻², respectively, were obtained, and a

value of 567.6 mAh g⁻¹ after 13 cycles at 0.1 mA cm⁻² could be maintained. Oh et al.⁴³⁶ studied the effects of incorporating metal (Pd and Au) nanoparticles onto MONW on the performance of Li-air batteries. They firstly incorporated poly acrylic acid (PAA) around the MONW to form PAA-MONW, and then nucleated the metal nanoparticle on PAA-MONW. The resulting Pd/PAA-MONW electrode (about 3 wt% Pd) could deliver a capacity of 13350 mAh g_{carbon}⁻¹ at 400 mA g_{carbon}⁻¹ and a stable cycle life up to 50 cycles with a fixed capacity of 4000 mAh g_{carbon}⁻¹ at 1 A g_{carbon}⁻¹ compared to that of 9930 mAh g_{carbon}⁻¹ for the Au/PAA-MONW (1.7% Au). Guo et al.⁵¹¹ synthesized the composite of γ -MnO₂ (fusiform nanorods) and hydrous RuO₂ (nanoparticles) (Mn-Ru binary oxide) by a hydrothermal method. At a current density of 0.1 mA cm⁻², the oxide based electrode with 45 wt% catalyst displayed a discharge capacity of 6500 mAh g_{carbon}⁻¹, which were much higher than 5100 and 3500 mAh g_{carbon}⁻¹, respectively, for the electrodes with 20 wt% catalyst and pure KB carbon. Furthermore, the charge voltage of such an electrode was about 500 mV lower than that of the cathode with KB, and could run stably for 50 cycles without sharp decay under a limited discharge depth of 1100 mAh g_{carbon}⁻¹. Ishihara et al.⁵¹² prepared mesoporous Co₃O₄ with mesoporous silica (KIT-6) as a template and mixed it with PdO to form a catalyst for the cathode of a Li-air battery. A discharge capacity of 481 mAh g_{catalyst}⁻¹, a discharge potential plateau of 2.8-2.7V and a charge voltage of 3.75 V at a current density of 0.1 mA cm⁻² were achieved. Choi et al.⁵¹³ found PdCu nanoparticles (PdCu NPs) mixed with disordered face-centered cubic (*fcc*) and ordered body-centered cubic (B2-type) phases could greatly enhance the rateability of the battery and also the kinetics of oxygen reduction/evolution reaction by significantly reducing the overpotentials, leading to a super round-trip efficiency of about 80%. The PdCu NPs electrode obtained a discharge capacity of 12000 mAh g_{carbon}⁻¹ at a current density of 200 mA g_{carbon}⁻¹ and attained 8000 and 1689 mAh g_{carbon}⁻¹, respectively, when the current densities

were increased to 2000 and 5000 mA g_{carbon}^{-1} , which were much better than the electrode with only Pd nanoparticles as catalysts. In Gomez et al.'s study,⁵¹⁰ the binder-free Co-Mn composite oxide electrode was prepared through a combination of electroless method (co-precipitating of Co and Mn metal directly on the carbon substrate) and electrolytic step (electro-oxidating co-deposited metal thin film substrate to form Co-Mn composite oxide). This electrode yielded an initial specific capacity of up to 2000 mAh g_{catalyst}^{-1} at a current density of 0.1 mA cm^{-2} . To avoid battery performance deterioration from the decomposition of carbon materials induced by discharge products and electrolyte to form Li_2CO_3 , much attention is paid to carbon-free cathode and their corresponding composite materials in non-aqueous Li-air batteries in recent years.⁵¹⁴⁻⁵¹⁷ For example, Li et al.⁵¹⁸ fabricated a carbon-free electrode of Ru/ITO by depositing Ru nanoparticles directly on indium tin oxide (ITO) and found that this electrode could decrease the charge overpotential by about 200 and 600 mV compared to the Super P and Ru/Super P electrode, respectively, at a current density of 0.025 mA cm^{-2} . The authors pointed out that the absence of carbon, which could react with Li_2O_2 to form Li_2CO_3 , should be a reason for the enhanced performance of Ru/ITO electrode except the good activity of Ru/ITO to ORR and OER. Similarly, Zhao et al.⁵¹⁹ prepared a carbon- and binder-free electrode with Pt/ Co_3O_4 flake arrays by electroplating Co_3O_4 directly on Ni foam forming flake arrays on which Pt nanoparticles were deposited by cool sputtering method. Although the obtained Pt/ Co_3O_4 flake arrays electrode delivered a much lower discharge capacity than the only Co_3O_4 flake arrays containing electrode (1000 vs. 3000 mAh $g_{\text{electrode}}^{-1}$ at 0.1 A $g_{\text{electrode}}^{-1}$), it could run stably for about 40 cycles which was much better than 10 cycles for the Co_3O_4 flake arrays electrode at a current density of 0.2 A $g_{\text{electrode}}^{-1}$. In addition, it was also found that the addition of Pt nanoparticles could lead to a much lower overpotential (3.2 V) in charge process than the pristine Co_3O_4 flake arrays

electrode (4.0 V).

The compounds with transition metals coordinated to heterocyclic N (such as Fe/N/C, Co/N/C etc.) are another group of composite materials which can exhibit good catalytic activity towards both ORR and OER.^{19,77,212,399,520,521} The heat-treated FeCu-phthalocyanine/KB EC600JD carbon complexes showed at least 0.2 V lower discharge overpotential at a current density of 0.2 mA cm⁻² than that of the pure carbon electrode.⁸⁷ Shui et al.⁵²² showed the atomically dispersed Fe/N/C composite prepared by pyrolyzing and the subsequent acid-leaching of the mixture of 1,10-phenanthroline, iron acetate and carbon could reduce the charge and discharge overpotentials and also significantly improve the battery lifespan when compared to the well-studied α -MnO₂/XC-72 and its unmodified carbon only counterpart. In addition, using this Fe/N/C catalyst, only oxygen could be detected during charge process, whereas CO₂ was also detected when α -MnO₂/C or carbon-only cathode was used, suggesting this catalyst could promote the decomposition of lithium peroxide. Yu et al.⁵²³ modified the graphene sponge (GS) with Fe-N-C catalyst (Fe-N-GS) by pyrolysis, the thus obtained cathode delivered a discharge capacity of 6762 mAh g_{electrode}⁻¹ which was about two times higher than that of 3474 mAh g_{electrode}⁻¹ for the GS electrode at a current density of 0.1 mA cm⁻². Furthermore, the Fe-N-GS electrode could also reduce the charge plateau to about 3.9 V which was almost 450 mV lower than that of 4.35 V for the GS electrode. Li et al.⁵²⁴ demonstrated a Fe-based catalyst (N-Fe-MOF) dominated by nitrogen-doped graphene/graphene-tube nanocomposites prepared by heat-treating Cage-Containing Metal-Organic Frameworks (MOF), and found that this catalyst could exhibit a discharge voltage of about 2.80 V which was higher than 2.51 V for carbon black, 2.62 V for the MOF-free N-Fe material, and 2.71 V for the Pt/C catalyst. A highest discharge capacity of 5300 mAh g_{catalyst}⁻¹ at a current density of 50 mA g_{catalyst}⁻¹ could be achieved, and this electrode

could also run stably for 16 cycles without capacity loss using 2.5 V as the discharge cut-off voltage (Fig. 24). Wang et al.⁵²⁵ found the Co(phenanthroline)₂/C catalyst prepared by pyrolyzing the cobalt(II) phenanthroline (phen) chelate and BP2000 carbon black mixture in an inert atmosphere could deliver the discharge capacities of 4870, 3353 and 3220 mAh g_{catalyst}⁻¹ at 0.05, 0.1 and 0.15 mA cm⁻², respectively, much higher than that of the BP2000 only cathode at the same current density. Zhang et al.⁵²⁶ prepared the Co nanoparticles highly dispersed on N-rich carbon substrates (Co-C composite) by sol-gel method, and found that Co-C composite was a promising electrocatalyst for Li-air battery. The Co-C composite electrode displayed a discharge capacity of about 5000 mAh g_{carbon}⁻¹ which was much higher than 3000 mAh g_{carbon}⁻¹ for the pure KB electrode at a current density of 300 mA g_{carbon}⁻¹. Besides, the Co-C composite electrode could run stably for about 50 cycles with a small increase in gap between the discharge and charge voltages under a limited capacity of 600 mAh g_{carbon}⁻¹ at a current density of 200 mA g_{carbon}⁻¹ (Fig. 25). Wu et al.³⁴⁹ reported the Co-N-MWCNTs catalyst prepared by graphitization of polyaniline under the catalysis of a cobalt species using multiwalled carbon nanotubes (MWCNTs) as a supporting template displayed significantly higher discharge voltage and capacity than those of the Co-N-KJ catalyst (a catalyst prepared using the ketjenblack as supporting template), metal-free N-C material and even Pt/C catalyst at 50 mA g_{catalyst}⁻¹, and it also demonstrated excellent capacity retention for 20 cycles without significant capacity loss.

In addition, composites consisting of nitrogen-doped carbon materials and molybdenum nitride or Mn oxides have also been introduced into non-aqueous Li-air batteries as the cathode catalysts. For instance, Dong et al.⁴¹³ synthesized the molybdenum nitride/nitrogen-doped graphene nanosheets (MoN/NGNSs) through a hydrothermal reaction of graphene oxide (GO) and molybdic acid followed by annealing in ammonia, a specific capacity of

1490 mAh $g_{\text{carbon+catalyst}}^{-1}$ at a current density of 0.04 mA cm^{-2} was achieved. Similarly, Zhang et al.²⁹⁰ reported that the molybdenum nitride/N-doped carbon nanospheres (MoN/N-C) synthesized by a hydrothermal method and subsequent ammonia annealing showed a discharge capacity above 1400 mAh $g_{\text{electrode}}^{-1}$ at 0.1 mA cm^{-2} in the first charge-discharge process and sustained at 790 mAh $g_{\text{electrode}}^{-1}$ after 10 cycles. The MnO₂ nanotubes/nitrogen-doped exfoliated graphene hybrid prepared by heating the GO in Ar/NH₃ mixed gases and then mixed with MnO₂ nanotubes exhibited an ORR onset potential of 2.92 V, which was very close to the theoretical value of 2.96 V, and a power density of 15.8 W g_{carbon}^{-1} at a current density of 100 mA g_{carbon}^{-1} .⁵²⁷

3.4 Other cathode materials

Except the carbon materials, metals/metal oxides and composite materials discussed above, some other materials have also been used as cathode materials for non-aqueous Li-air batteries. For example, Li et al.⁵²⁸ reported sulphur-doped graphene (S-GNS), prepared by pyrolyzing the mixture of GNS and *p*-toluenesulfonic acid, had an initial recharge capacity of 4100 mAh g_{catalyst}^{-1} , which was much higher than 170 mAh g_{catalyst}^{-1} for a pristine graphene electrode at a current density of 75 mA g_{catalyst}^{-1} , although its initial discharge capacity displayed at 4300 mAh g_{catalyst}^{-1} which was dramatically lower than that 8700 mAh g_{catalyst}^{-1} for the pristine graphene electrode. Moreover, the discharge capacity of the S-GNS electrode attained 3500 mAh g_{catalyst}^{-1} at the second cycle while the pristine graphene electrodes only had a retention of 220 mAh g_{catalyst}^{-1} . Tian et al.⁵²⁹ reported a fluorinated carbon nanotube (CF_x) showed capacities of 1007 and 676 mAh g_{carbon}^{-1} at the current densities of 30 and 100 mA g_{carbon}^{-1} , respectively, which were higher than 682 and 188 mAh g_{carbon}^{-1} for the pristine CNTs. The CF_x as cathode was also investigated by Xiao et al.³³⁷ and the attained capacities

were approximately 950 and 521 mAh $g_{\text{electrode}}^{-1}$ at the current densities of 0.1 and 0.2 mA cm^{-2} , respectively, which were about two times higher than those of the pure KB electrode. Zhang et al.²⁰² prepared a mesoporous cobalt molybdenum nitride (Co_3Mo_3N) using a co-precipitation method followed by ammonia annealing treatment, and the obtained catalyst displayed a discharge capacity of about 1300 mAh $g_{\text{electrode}}^{-1}$ at a current density of 0.1 mA cm^{-2} . Li et al.²⁰⁵ showed that a n-TiN/VC-based (nano-sized TiN nanoparticles supported on Vulcan XC-72 carbon) electrode exhibited a discharge capacity of above 6000 mAh g_{carbon}^{-1} at 500 mA g_{carbon}^{-1} and a discharge-recharge voltage gap of 1.05 V at 50 mA g_{carbon}^{-1} , which were 390 and 450 mV lower than that of m-TiN/VC (micro-sized TiN supported by Vulcan XC-72) and Vulcan XC-72, respectively. In addition, the coaxial platinum/titanium nitride nanotube arrays were also explored by Dong et al.⁵³⁰ as cathode catalyst in non-aqueous Li-air batteries and produced a better performance than the commercial Pt/C catalyst (with 20 wt% Pt).

Because of the unique metallic/semiconductor characteristics and their potential usage in electrochemistry^{520,531-535} electronics⁵³⁶ and biosensors,⁵³⁷ conjugated heterocyclic conductive polymers have received more and more attention since the late 1970s. Polypyrrole (PPy), poly(3,4-ethylenedioxythiophene) (PEDOT) and polyaniline (PANi) have recently been proven to have certain activity when they are used in the cathode of Li-air batteries.^{311,538-541} For example, Cui et al.³¹¹ synthesized some tubular polypyrrole nanotubes (TPPy) with a self-degraded template for cathode materials of Li-air batteries, and compared their performance with those of acetylene carbon black (AB) and granular PPy (GPPy) (Fig. 26). At a current density of 0.1 mA cm^{-2} , the discharge voltage of TPPy electrode was consistently higher than that of a GPPy electrode by about 100 mV and that of a AB electrode by about 300 mV, while its charge voltage was substantially lower than that of GPPy by 100 mV and

AB by 600 mV, respectively. The TPPy electrode also exhibited both much better rate capability and cycling performance than the GPPy and AB electrodes. A discharge capacity of 1764 mAh g_{catalyst}^{-1} was delivered at 0.5 mA cm^{-2} by the TPPy electrode, which was comparable to that of 1982 mAh g_{catalyst}^{-1} at 0.1 mA cm^{-2} , implying a capacity retention of 89.0%, while the GPPy and AB electrodes only exhibited the capacity retentions of 71.27% and 37.07%, respectively. The authors attributed the better performance of TPPy electrode to both the abundant gas diffusion channels and reaction sites. Zhang et al.⁵³⁸ found PPy could exhibit both higher capacity and better cycling performance than carbon materials owing to its high catalytic activity towards ORR as well as OER. Moreover, they demonstrated that the electrochemical performance of PPy could be significantly influenced by the dopants, and that the PPy doped with Cl^- exhibited higher capacity and more stable cyclability than that doped with ClO_4^- . Nasybulin et al.⁵³⁹ prepared PEDOT by in-situ chemical polymerization of 3,4-ethylenedioxythiophene monomer in a carbon matrix, and showed that the PEDOT could significantly reduce the overpotential by 0.7-0.8 V during the charging process of the Li-air battery in addition to its apparent improvement in discharge capacity. The authors attributed the positive effect of PEDOT to its redox activity, and believed that PEDOT could act as a mediator in electron transfer during the charge-discharge process. The nonfibrous PANi, synthesized by a chemical route of miniemulsion polymerization technique,⁵⁴⁰ demonstrated a discharge capacity of 1380 mAh g_{catalyst}^{-1} at 0.05 mA cm^{-2} , however, it dropped fast to less than 100 mAh g_{catalyst}^{-1} when the current density was increased to 0.5 mA cm^{-2} within the voltage range of 1.75-4.2 V. In order to promote the performance of PANi as a cathode material in non-aqueous Li-air batteries, Lu et al.⁵⁴⁰ modified the synthesis route and prepared a water dispersed conducting PANi nanofiber material by doping phosphate ester as an anion, the resulting electrode could deliver discharge capacities as high as 3260 mAh

g_{catalyst}^{-1} and $1000 \text{ mAh } g_{\text{catalyst}}^{-1}$, at current densities of 0.05 mA cm^{-2} and 0.5 mA cm^{-2} , respectively. After an initial degradation from 3260 to 2320 $\text{mAh } g_{\text{catalyst}}^{-1}$ after three cycles at 0.05 mA cm^{-2} , its discharge capacity kept relatively stable in the next 27 cycles with only a 4% loss. Therefore, the authors claimed that this procedure could provide a new choice for fabrication of high-capacity rechargeable Li-air batteries. Moreover, conductive polymers can also act as binders to improve the electrical conductivity of cathodes in non-aqueous Li-air battery. The earlier usage of PPy as a functional binder in air cathodes was conducted by Cui et al.⁵⁴¹ using a self-assembly process. The obtained PPy/C electrode exhibited the discharge capacities of 2626.3 and 1816.4 $\text{mAh } g_{\text{electrode}}^{-1}$ at current densities of 0.1 and 0.5 mA cm^{-2} , respectively, which were much higher than 1005.8 and 345.6 $\text{mAh } g_{\text{electrode}}^{-1}$ for the cathode with PVDF as a binder. They also found that the contacts between electrode materials and the distribution of the discharge products in the cathode could be optimized by using PPy as a binder, leading to the reduction of overpotential in the charge-discharge process as well as an increase in battery round-trip efficiency.

In general, both catalysts and discharge products (Li_2O_2) are in solid states and thus it is difficult to bring the catalyst into homogeneous contact with the formed reaction products, i.e., some portion of the solid reaction products could block the catalyst activity during the discharge process. Meantime, the solid-solid interface between catalyst and discharge products also limits the efficiency of catalyzed formation and decomposition of discharge products (Fig. 27a), leading to difficulty in the discharge process with increasing discharge depth, and resulting in high cathode overpotential during the charge process. Two possible approaches have been proposed to alleviate these issues. One is to increase the solubility of Li_2O_2 ⁵⁴² so that its oxidation could take place primarily in solution at the electrode surface, and the other is to incorporate a redox mediator (M_{red}) which is a soluble molecule in

solution.^{259,543} In this way, during the charge process, the M_{red} could be oxidized directly at the electrode surface to form its oxidized form (M_{ox}), which then oxidizes the Li_2O_2 particles and itself is reduced back to M_{red} . Actually, this mediator acts as an electron-hole transfer agent between the solid electrode and solid Li_2O_2 (Fig. 27b). A suitable redox mediator must meet three characteristics:^{103,114} (1) the redox potential (oxidation/reduction) of M_{red} should be compatible with that of Li_2O_2 formation, that is, the oxidation potential needs to be slightly higher than the equilibrium potential of the Li_2O_2 formation; (2) M_{ox} should be capable of efficiently decomposing Li_2O_2 ; and (3) the redox mediator must not react with the electrolyte or Li metal anode, and should be highly dissolvable in the electrolyte. In recent years, several researches on redox mediators have been reported in literature in the effort to enhance the performance of non-aqueous Li-air batteries.⁵⁴⁴ Chen et al.¹⁰³ employed tetrathiafulvalene (TTF), ferrocene (FC) and N,N,N',N' -tetramethyl-*p*-phenylenediamine (TMPD) as redox mediators in non-aqueous Li-air batteries, and found FC and TMPD were unstable during the charge process although they could oxidize the solid Li_2O_2 , while TTF enabled the recharging at rates that were impossible for the cell without a mediator. The battery with the TTF mediator demonstrated a dramatically lower charge potential than the one without TTF, and ran stably for 100 cycles. In Kim et al.'s study,^{259,259} they systematically investigated the effects of LiI concentration on the performance of battery with carbon or Co_3O_4 as catalyst. The results showed that the battery with both solid Co_3O_4 and dissolved LiI outperformed all the others with only carbon, only Co_3O_4 or only LiI as the catalyst. It was also found that the increase in LiI concentration could lead to a decreased charge voltage and also an enhanced electrochemical reversibility of the electrode. In addition, the redox mediator of ethyl viologen ditriflate was also used to catalyze an oxygen reduction reaction during the discharge process by Lacey et al.⁵⁴⁵ and some improvement in

overall battery performance was observed.

In addition to the materials summarized above, organic materials are gradually attracting attention as cathode materials, especially as the catalysts in Li-air batteries, due to their merits of being inexpensive, renewable and even self-repairing.^{546,547} Metal-organic frameworks (MOFs) are good examples. The large mesopores in the frameworks can not only provide channels for electrolyte and oxygen diffusion but also supply spaces for product deposition. Wu et al.⁵⁴⁸ synthesized the MOFs of MOF-5, HKUST-1, Mg-MOF-74, Mn-MOF-74 and Co-MOF-74 and prepared the cathodes with the combination of MOFs and Super P as the electrode materials. These MOFs could deliver discharge capacities of 1780, 4170, 4560, 9420 and 3630 mAh g_{catlyst+carbon}⁻¹, respectively, whereas the pure Super P electrode only had a discharge capacity of 2170 mAh g_{catlyst+carbon}⁻¹ at a current density of 50 mA g_{catlyst+carbon}⁻¹ (Fig. 28). Other than MOFs, Weng et al.⁵⁴⁹ prepared polyethylenimine (PEI) supported anthraquinone (AQ) by the Riedl-Pfleiderer process as a cathode catalyst for Li-air batteries, and found the PEI-AQ based electrode could increase the discharge voltage by about 70 mV from that of a pure Super P electrode, and could also run stably for about 20 cycles compared to less than 10 cycles for the latter.

4 Cathode Structures and Processes

In addition to storing the discharge products, the cathode structures of Li-air battery can also affect the utilization of electrode materials,⁵⁵⁰ the morphology of discharge products,³¹⁶ oxygen transport,⁵⁵¹ wettability, ionic transfer and electric conductivity of the whole cathode.³¹² All of these factors can play very important roles on the overall battery performance. Therefore, an ideal cathode should be developed via an optimized process to achieve a perfect cathode structure using appropriate cathode materials.

As discussed above, the discharge products in non-aqueous Li-air batteries are insoluble in the electrolyte, and can deposit on the surface or in the pores of the cathode, preventing oxygen from diffusing to the catalyst surface. Therefore, an ideal cathode^{84,552-554} should remain partially dry so that air/oxygen can diffuse smoothly in the gas phase throughout the electrode porous channels, and then be reduced on the oxygen-catalyst-electrolyte interface. Another preferred ideal cathode structure⁹¹ is that all the surface in the cathode is completely wetted with a very thin film of liquid electrolyte in order to maximize the reaction area, but the pores in the electrode are not flooded with liquid electrolyte so that oxygen can diffuse quickly through the gas phase. Thus, the porous structure of the cathode should be well controlled and developed to achieve high-performing Li-air batteries.

The porosity, pore size, pore volume and the usable fraction as well as surface area of the cathode have been found to play significant roles on the performance of Li-air batteries.^{35,555,556} Zhang et al.⁹¹ presented a theoretical correlation between the cathode porosity and discharge capacity. Combined with the experimental results, they assumed the normal porosity of a carbon air electrode was about 2.8-3.4 ml g⁻¹ and the gravity densities of Li₂O₂ and Li₂O were 2.140 and 2.013 g cm⁻³, respectively. Thus, they considered the carbon cathode could provide a maximum capacity ranged from 7000 to 12000 mAh g_{carbon}⁻¹, as shown in Fig. 29. Cheng et al.³⁰⁸ found post heat-treatment on the MnO₂/C cathode could lead to a great improvement in the discharge capacity as well as cycling performance owing to increased porosity in the electrode. Gbolahan et al.⁵⁵⁷ prepared Li-air batteries using phenol-formaldehyde based activated carbon with different mesopore volumes and found the discharge capacity could be increased with increasing mesopore volume, and a highest capacity of 1852 mAh g⁻¹ at a current density of 70 mA g⁻¹ can be obtained with a pore volume of 1.8717 cm³ g⁻¹. Kraytsberg et al.¹¹⁶ considered the pore volume in the cathode

would not be completely filled with discharge products when the discharge was terminated, and the fraction of usable pore volume was different in the studies carried out by different researchers.^{28,245,333} For example, it was about 47% with a carbon loading of 1.96 mg cm^{-2} , but only 3% when the loading was increased to 12.57 mg cm^{-2} .²⁸ The probable reason for this discrepancy should be, at least in part, due to the different processes used to prepare the electrode as well as the different materials used and their various characteristics such as morphology/structure, surface area, particle size and pores.

It is generally believed the cathode with a high surface area is beneficial for obtaining a high discharge capacity induced by the increased number of electrochemical active sites available to form lithium oxides and also enlarged space for accommodating the discharge products.³²⁷ However, the surface area does not have a simple positive relationship with overall battery performance because some other performance-determining factors, especially pore size and the distribution in the electrode, can also make contributions. When the pore size is too small, such as micropores, the entrance of the pores is easily blocked, thus the inner part of the pores cannot be utilized, resulting in lower discharge capacity.⁵⁵⁸ Nimon et al.²⁴³ reported the discharge capacity of a cathode could be limited by the volume of small mesopores with radii up to 10 nm, observed by their standard contact porosimetry method. Ma et al.⁵⁵⁶ depicted mesopores were more effective in the utilization of pore volume than micropores. The cathode prepared with mesoporous carbon aerogel showed at least ten times higher discharge capacity than that with microporous activated carbons. Chervin et al.²⁸⁸²⁸⁸ studied the influence of pore size in free standing, binder-free carbon nanofoam papers on their discharge capacity when used as cathode materials in Li-air batteries. They found the capacity tracked the average pore size distribution in the carbon nanofoam cathode, rather than the specific surface area of the nanoscale carbon network or its total pore volume. The

macroporous nanofoams could yield a higher discharge capacity than the mesoporous nanofoams, even though the macroporous foams had lower specific surface areas. Based on these observations, they proposed a cathode design strategy that incorporated macropores, particularly at the O₂-facing boundary of the electrode, might be beneficial in cathodes for Li-air batteries, as they are less susceptible to blockage by discharge products than cathodes incorporating mesopores. In other words, they concluded that gradients of pore size with larger pores at the O₂ side of the electrode tapering to smaller pores near the electrolyte (O₂-diffusion-limited region) might ultimately be desirable to achieve an optimal combination of surface-to-volume ratio as well as a more uniform discharge product distribution. Similarly, Zhang et al.³¹⁹ found pores with diameters of 10-300 nm were more suitable for the deposition of solid products than those with diameters less than 10 nm. However, Lin et al.²⁰⁴ found the HCC electrodes with pore sizes of 100 nm (HCC-100) had a better performance than those with pore size of 400 nm (HCC-400), based on the initial discharge capacity and cycleability as well as the associated volumetric energy density.

Several novel cathode structures have been developed in recent years and each of them has demonstrated feasibility. Zhang et al.³⁵⁵ employed SWCNTs and the ionic liquid (IL) of [C₂C₁im][NTf₂] to prepare a cross-linked network gel (CNG) of SWCNTs/[C₂C₁im][NTf₂] using an ultrasonic method followed by grinding and subsequent centrifugation (Fig. 30). The SWCNTs/[C₂C₁im][NTf₂] CNG based electrode exhibited a discharge capacity of 5930 mAh g_{carbon}⁻¹ at a current density of 200 mA g_{carbon}⁻¹ while the SWCNTs/IL mixture obtained by direct centrifugating the suspension of SWNTs and [C₂C₁im][NTf₂] by ultrasonic dispersion without grinding only delivered a capacity of 950 mAh g_{carbon}⁻¹. Furthermore, the CNG electrode could give capacities of about 4000 and 2000 mAh g_{carbon}⁻¹ at the current densities of 1000 and 2000 mA g_{carbon}⁻¹, respectively. The authors attributed the outstanding

performance of the CNG cathode to the superior three-dimensional tricontinuous passage of electrons, ions, and oxygen, which was able to expand the conventional three-phase reactive interface to the whole cross-linked network. They believed the three-phase interfacial reaction was only confined by the dissolved oxygen in a conventional air electrode. In their novel cathode, however, the SWNTs were untangled by a π -cation/ π -electron interaction with the imidazolium cation of $[\text{C}_2\text{C}_1\text{im}]^+$, forming physical gels with cross-linked networks in which $[\text{NTf}_2]^-$ ions were anchored through electric neutrality, oxygen could fill the entire cross-linked network gel, electrons could conduct along the carbon nanotubes, transport of lithium ions from the ionic liquid electrolyte outside into the cross-linked network gel could become coordinated by the inside-anchored $[\text{NTf}_2]^-$ ion, oxygen in the cross-linked network could incorporate with the lithium ions and electrons along the SWNTs, then turning into the discharge products. Similarly, Balaish et al.⁵⁵⁹ developed a three-phase reaction zone cathode by employing two immiscible solvents of perfluorinated carbon liquids (PFC) and TEGDME which undertook the diffusion of oxygen and Li ion, respectively (Fig. 31). They placed a small drop of PFC solvents (perfluoro-n-octane, perfluoro(decahydrophthalene), perfluoro-n-nonane or 1-bromoperfluoroheptane) on the carbon side of the cathode surface to impregnate the cathode *meso*-pores by PFC, and then assembled the batteries using LiPF_6 -TEGDME as the second electrolyte. All the PFC-contained batteries displayed increased discharge capacities and improved discharge voltages from that of the pure TEGDME battery, demonstrating the PFC-treatment had positive effects on overall battery performance. Considering the insufficient oxygen solubility and diffusivity in the electrolyte of conventional non-aqueous Li-air batteries employing a flooded cathode which could lead to a non-uniform deposition of Li_2O_2 and incomplete utilization of cathode volume, Xia et al.⁵⁶⁰ developed a partially flooded cathode by evaporating diethyl ether from the electrolyte

allowing gaseous oxygen to penetrate quickly into the interior part of the porous cathode for electrochemical reaction. The effective electrode area for oxygen reduction was, thereby, increased to enhance the cathode kinetics. Using typical cathode materials, the partially wetted cathodes yielded a 60% higher discharge capacity and one magnitude higher rate capability than the flooded cathode. Lim et al.⁵⁶¹ prepared a hierarchical air electrode by cross-weaving ten sheets of CNT fibrils layer-by-layer on a Ni mesh followed by embedding Pt nanoparticles. At a high rate of $2 \text{ A g}_{\text{carbon}}^{-1}$, this electrode performed stably for over 130 cycles with a fixed capacity of $1000 \text{ mAh g}_{\text{carbon}}^{-1}$ and for 100 cycles with full charge-discharge in the voltage range from 2.0 to 4.7 V, which were much better than 70 and 30 cycles, respectively, for the bare CNTs electrode (ten sheets of CNT fibrils layer-by-layer). The authors attributed the outstanding performance of the novel cathode to its aligned carbon structure with a hierarchical micro-nano-mesh which could ensure a facile accessibility of reaction products and provide the optimal catalytic conditions for the Pt catalyst. Liu et al.⁵⁶² prepared a free-standing, hierarchically porous carbon nanotube film electrode by virtue of the unique bimodal design for porosity and a discharge capacity of $4683 \text{ mAh g}_{\text{electrode}}^{-1}$ at $50 \text{ mA g}_{\text{electrode}}^{-1}$ was observed. A gas diffusion electrode (GDE) with a double-layer structure (gas diffusion layer and catalyst layer), similar to that in proton exchange membrane fuel cells, has also been used as the cathode in Li-air batteries.³³⁴ A Super P electrode prepared by this method could acquire a high specific discharge capacity of $6587 \text{ mAh g}_{\text{carbon}}^{-1}$ at a current density of 0.15 mA cm^{-2} with a 2.077 mg cm^{-2} of carbon loading, which was dramatically higher than that of a conventional cathode with Super P carbon materials. Cheng et al.⁵⁶³ showed the nanoporous three-dimensional GDE with carbon-supported MnO_2 catalyst could display higher discharge capacity and discharge voltage, lower charge voltage and better cycleability than the composite electrode. Similarly, Yang et al.¹⁹⁰ prepared a double-layer

structural air cathode consisting of diamond like carbon (DLC) active layer and CoO_x catalytic layer, showing a significant improvement in discharge/charge electrochemical performance.

The loading of cathode materials is another considerable parameter influencing the battery performance as well as the utilization of the materials.^{214,334} Gao et al.³³⁴ found the best carbon loading was 2.08 mg cm^{-2} in a range from 2.08 to 6.00 mg cm^{-2} according to the fact that the discharge capacity decreased with increasing carbon loading. Similarly, Park et al.³⁸⁶ displayed the carbon-sphere/ Co_3O_4 electrode with a materials (catalyst + carbon + binder) loading of 1.1 mg cm^{-2} could deliver about $4500 \text{ mAh g}_{\text{electrode}}^{-1}$ at $200 \text{ mA g}_{\text{electrode}}^{-1}$, while the discharge capacity was decreased to ~ 3400 and $\sim 2900 \text{ mAh g}_{\text{electrode}}^{-1}$, respectively, as the loading was increased to 1.3 and 1.9 mg cm^{-2} . Park et al.,²¹⁴ however, believed there was an optimal carbon loading to achieve best performance. They studied the cathode with various carbon loadings in the range from 0.61 to 5.91 mg cm^{-2} and found the electrode with a carbon loading of 2.96 mg cm^{-2} on the nickel foam displayed the highest discharge capacity. The authors assumed the carbon particles adhered to the nickel foam structure instead of agglomerating themselves, which could reduce the pore volume for depositing Li_2O and/or Li_2O_2 under this optimal value. On the contrary, however, the excess carbon would close the open structure of the foam thus impeding the flow of oxygen, leading to reduced discharge capacity.

The thickness of the cathode also plays an important role on the battery performance in terms of the charge-discharge capacities and the uniform distribution of lithium peroxide in the interior and on both sides of the electrode.²⁹⁸ Chervin et al.²⁸⁸ showed that an increase in electrode thickness could lead to a decreased capacity. The carbon nanofoam paper electrodes with thicknesses of about 180 , 360 , and $530 \mu\text{m}$ could yield the discharge capacities of 890 ,

590, and 360 mAh g_{electrode}⁻¹, respectively, at a current density of 0.3 mA cm⁻². Similarly, Zhang et al.²⁹⁸ found SWCNTs/CNFs bucky papers with a thickness of 19.7 μm could deliver a capacity as high as 2500 mAh g_{electrode}⁻¹ at a current density of 0.1 mA cm⁻², but only 1600 and 400 mAh g_{electrode}⁻¹ could be achieved for the electrode with a thickness of 65.5 and 219.2 μm, respectively.

The process employed to construct a cathode can also significantly influence the structure of the obtained electrode, resulting in different performance. Normally, an ideal cathode structure should be built with proper process. So far, the main processes reported in literature to fabricate a cathode include rolling,^{49,336} spreading,⁴⁰⁹ casting,^{299,367,564} coating^{110,230} or spraying³³⁴ the slurry made from cathode materials such as catalyst, conductive agent and binder onto a substrate such as nickel foam (NF),^{336,409,565} aluminum grid,^{83,94,566} carbon paper^{112,334} and even separator (i.e. glass fiber),¹³⁵ and each of them has their own inherent characteristics. However, only very few researchers have conducted comparative investigation on the effects of cathode process as well as the substrate on the performance of Li-air batteries. Ma et al.³⁰⁵ prepared cathodes by rolling, coating and spraying the cathode materials onto carbon paper and nickel foam substrates, and systematically compared the morphologies, discharge characteristics and high rate dischargeability of the obtained cathodes. The results indicated nickel foam was a preferred substrate for a cathode prepared with a spraying method owing to its skeletal porous structure, and the spraying method along with the nickel foam substrate seemed to be the best approach to fabricating Li-air batteries with high performance. The intermediate pressing process could improve the performance of the cathode prepared with the coating method which might be attributed to the establishment of sufficient paths for oxygen diffusion. In Shui et al.'s study,⁴¹⁶ they found the VA-NCCF arrays supported on stainless steel (SS) cloth could

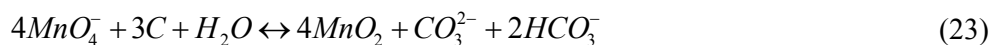
deliver a gap of 0.55 V between the discharge and charge voltages, which was apparently lower than that on carbon paper.

In addition to the general fabrication processes discussed above, several novel processes have recently been proposed and explored to enhance the performance of non-aqueous Li-air batteries.^{28,567} For example, Beattie et al.²⁸ demonstrated an ultrasonic immersion method of encouraging the cathode slurry to penetrate into the structure of nickel foam through sonication followed by removing the solvent using heat treatment. Nevertheless, it seems very difficult to control the loading of the materials in the electrode. Crowther et al.³⁴⁰ presented a novel “mineral spirits” approach. They produced a dough of electrode materials with a small amount of mineral spirits and then pressed the dough onto a substrate at a certain temperature to establish composite cathodes. The resulting electrode acquired a high porosity of about 85%.

For most of the cathode processes discussed above, the electrode materials are usually physically mixed into slurry and then loaded onto the substrate. The as-prepared cathode sometimes has a low conductivity because of the poor interaction between conductive agent (usually carbon) and catalyst due to the using of a binder. According to Younesi et al.’s study,⁵⁵⁵ the discharge capacity can decrease with an increased amount of binder owing to its blocking effect on the pores on the carbon with a width below 300 Å. Cheng et al.³⁰⁸ presented there was an optimal additive amount of binder to achieve the balance between the requirement for good adhesion, acceptable conductivity and access for oxygen. In order to overcome this challenge, many methods have fortunately been developed in recent years to prepare the binder free cathode to improve the interaction between catalyst and conductive agent.^{287,568} Zhang et al.²⁹² suspended α -MnO₂ into DMF with ultra-sonication and then mixed it with CNTs and CNF followed by filtering to get a α -MnO₂/CNT/CNF composite

paper. The obtained cathode exhibited great advantages over the general binder-used processes, indicated by a much lower electrical resistance probably because the materials could be held together by van der Waals forces, resulting in a highly reproducible process. In their study, the variations of the specific surface area and porosity of composite papers could be controlled to less than 5%. A discharge capacity of $3120 \text{ mAh g}_{\text{catalyst}}^{-1}$ at a current density of 0.2 mA cm^{-2} was achieved with this electrode, which was significantly higher than all the reported capacity values for the binder-contained MnO_2 electrodes. Cheng et al.³⁰⁸ and Li et al.⁵⁶⁴ individually prepared the Norit carbon supported MnO_2 (MnO_2/NC) and the multi-walled carbon nanotubes supported MnO_2 nanoflakes ($\text{MnO}_2/\text{MWCNTs}$), respectively, by in-situ redox reaction. The MnO_2/NC electrode demonstrated a better dispersion and connection between the catalyst and carbon matrix than the conventional cathode prepared with physically mixed carbon and commercial EMD. A discharge capacity of $3700 \text{ mAh g}_{\text{carbon}}^{-1}$ was attained which was higher than $2700 \text{ mAh g}_{\text{carbon}}^{-1}$ for the conventional cathode at $70 \text{ mA g}_{\text{carbon}}^{-1}$.³⁰⁸ The $\text{MnO}_2/\text{MWCNTs}$ electrode enhanced the kinetics of both ORR and OER, thereby effectively improved the energy efficiency and reversible capability. It exhibited a low charge potential of 3.8 V and a considerable capacity of $1768 \text{ mAh g}_{\text{carbon}}^{-1}$ at a current density of $70 \text{ mA g}_{\text{carbon}}^{-1}$.⁵⁶⁴ Yoon et al.⁵⁶⁷ created a new facile approach allowing effective interaction between the carbon materials (CNTs) and catalyst (CO_3O_4) by introducing a polydopamine layer as a reacting assistant. The resulting electrode produced a discharge capacity of $6300 \text{ mAh g}_{\text{electrode}}^{-1}$ at a current density of $200 \text{ mA g}_{\text{electrode}}^{-1}$. Wang et al.⁵⁶⁹ drew an electrode on a ceramic state electrolyte with pencil, obtained a discharge capacity of $950 \text{ mAh g}_{\text{carbon}}^{-1}$ at a current density of $0.1 \text{ A g}_{\text{carbon}}^{-1}$ and good reversibility without obvious capacity loss after 15 full cycles with a cut-off voltage at 2.0 V . Qin et al.²⁰¹ fabricated a porous-carbon-supported $\alpha\text{-MnO}_2$ nanorods cathode by in-situ depositing MnO_2 onto carbon,

a resulting discharge capacity of 1400 mAh $g_{\text{carbon+catalyst}}^{-1}$ and a charge voltage as low as 3.5-3.7 V were demonstrated at a current density of 100 mA $g_{\text{carbon+catalyst}}^{-1}$. Wang et al.²⁸⁴ prepared a graphene oxide gel-derived free-standing hierarchically porous carbon (FHPC) electrode which exhibited discharge capacities of 11060 and 2020 mAh g_{carbon}^{-1} at a current density of 0.2 mA cm^{-2} (280 mA g_{carbon}^{-1}) and 2 mA cm^{-2} (2.8 A g_{carbon}^{-1}), respectively. Similarly, Zhang et al.⁵⁷⁰ also prepared the freestanding and binder free MnO₂@carbon papers electrode wherein the carbon papers not only acted as reducing agents, but also as a substrate for the reaction as described by Equation 23. This electrode displayed the discharge and charge voltages of 2.68 V and 4.15 V, respectively, and the discharge capacity was sustained at about 1000 mAh g_{catalyst}^{-1} after 80 cycles at a current density of 0.1 mA cm^{-2} . These results were much better than the 50 mAh g_{catalyst}^{-1} after 20 cycles for the mixed MnO₂ electrode.



In order to avoid the undesired surface passivation (identified as dense Li oxide film) on carbon surface in the cathode, which could reduce the discharge capacity and terminate the lifespan of the battery early,⁵⁷¹ during discharge process, Tran et al.⁵⁷¹ modified the carbon surface with long-chain hydrophobic molecules by soaking in an aqueous solution containing 5% of an active fluoroaliphatic polyoxyethylene compound under vacuum for 30 minutes. The resulting cathode achieved a substantially increased discharge capacity (more than 3 times greater.). The conjecture as to the cause of this result was that the carbon surface modification delayed the formation of dense Li oxide layers and thus kept the discharge capacity at a high level.

5 Challenges and research directions

Li-air batteries are becoming one of the most promising energy storage and conversion technologies because of their ultrahigh energy density.⁵⁷² They are, however, still in the infancy stage of development. There are many challenges needing to be overcome before their practical commercial application.^{4,573-576} These challenges include the low round-trip efficiency, low discharge capacity and practical energy density, poor cycle-ability, and low rate capability, as well as many others. These challenges seem to be caused by the low-performing air cathode of the Li-air battery. Therefore, seeking new cathode materials and designing/fabricating specific structures to reduce the cathode overpotential, especially during the charge process, are the primary future tasks related to the cathode of rechargeable non-aqueous Li-air batteries.

Several future directions for developing cathodes of non-aqueous Li-air batteries can be suggested as follows:

(1) Exploring new cathode materials including catalysts and new cathode structures for both ORR and OER through innovative synthesis, characterization, design and fabrication as well as performance validation. The solution-phase catalysis might be a direction for developing new cathode catalysts.⁵⁷⁷ Building the electrode with different pore size/distribution/structure to meet the multiple purposes of electrolyte wettability and oxygen transfer could be a good choice for optimizing the cathode structure and fabrication.

(2) Significantly reducing the large cathode overpotentials during charge-discharge processes by developing highly active and stable catalytic materials such as bi-functional catalysts towards both ORR and OER. The developed catalysts should have insignificant promoting effects on the decomposition of the electrolyte.^{337,578} In this regard, the carbon

supported catalysts and composite catalysts with optimized structure and uniform particle distribution seem attractive, and are worthy of further optimization in terms of both catalytic activity and stability. However, considering the instability of carbon materials,^{101,186,579} carbon-free catalysts and their associated cathodes should receive more attention in the future.^{517,580}

(3) Efficiently controlling and optimizing the formation/decomposition of Li_2O_2 in terms of morphology and distribution as well as its interaction with the cathode materials/catalysts. This is because the morphology and distribution of discharge products has a significant influence on the cathode overpotentials during Li-air battery charge-discharge processes.

(4) Optimizing the cathode structure and its fabrication process. In the literature, very few researchers have systematically conducted studies to compare the effects of cathode structure and fabrication on overall battery performance. Therefore, the optimization of cathode structure and fabrication process (such as cathode preparation, loading of cathode materials and so on) seems to be very urgent in order to promote the performance of Li-air batteries up to a practical application level.

(5) Optimizing and standardizing the weight ration of electrolyte to cathode. The contact between cathode and electrolyte is a key factor for building a high-performing Li-air battery. This involves many aspects, such as oxygen diffusion channels and the weight ratio of the electrolyte/cathode.^{581,582} At this stage, researchers have realized the significant role of oxygen diffusion channels in cathode toward cell performance, but they have not been able to fully answer the questions how the oxygen diffusion channels can be optimally built.⁵⁸³ Therefore, the optimization and standardization of the weight ration of electrolyte to cathode is a very important task before the commercial application of Li-air batteries can be realized.

(6) Further fundamental understanding of the reaction mechanisms of Li-air batteries is

required. This is especially true for those mechanisms related to ORR and OER in terms of cathode material, catalysts and cathode structures, and fabrication processes and their effects on Li-air battery performance.^{9,117,232,584-586} Based on these fundamental understandings, cathode materials/catalysts, structures and their fabrication processes can be down-selected and optimized with respect to the overall battery performance.

(7) Mechanical properties of Li-air battery components should be given more attention. Currently, most of the research interests are mainly focused on fundamental aspects of Li-air batteries, such as the cathode catalyst, structure and mechanisms, but the mechanical properties and their influence on Li-air battery cathode components have not been given sufficient attention, particularly for flexible Li-air batteries.

Acknowledgements

The authors are grateful for the financial support of this work by the National Science Foundation of China (21176155 and 21476138).

References

1. M. Winter and R. J. Brodd, *Chem. Rev.*, 2004, **104**, 4245-4270.
2. P. Simon and Y. Gogotsi, *Nat. Mater.*, 2008, **7**, 845-854.
3. Y.-J. Wang, D. P. Wilkinson and J. Zhang, *Chem. Rev.*, 2011, **111**, 7625-7651.
4. B. Dunn, H. Kamath and J. M. Tarascon, *Science*, 2011, **334**, 928-935.
5. Z. Yang, J. Zhang, M. C. Kintner-Meyer, X. Lu, D. Choi, J. P. Lemmon and J. Liu, *Chem. Rev.*, 2011, **111**, 3577-3613.
6. G. Wang, L. Zhang and J. Zhang, *Chem. Soc. Rev.*, 2012, **41**, 797-828.
7. P. G. Bruce, S. A. Freunberger, L. J. Hardwick and J.-M. Tarascon, *Nat. Mater.*, 2012, **11**, 19-29.
8. M. D. Bhatt, H. Geaney, M. Nolan and C. O'Dwyer, *Phys. Chem. Chem. Phys.*, 2014, **16**, 12093-12130.
9. F. Cheng and J. Chen, *Chem. Soc. Rev.*, 2012, **41**, 2172-2192.
10. J. Lu, L. Li, J.-B. Park, Y.-K. Sun, F. Wu and K. Amine, *Chem. Rev.*, 2014, **114**, 5611-5640.
11. I. Kowalczyk, J. Read and M. Salomon, *Pure Appl. Chem.*, 2007, **79**, 851-860.
12. E. J. Cairns and P. Albertus, *Annu. Rev. Chem. Biomol.*, 2010, **1**, 299-320.
13. P. G. Bruce, L. J. Hardwick and K. M. Abraham, *Mrs. Bull.*, 2011, **36**, 506-512.
14. J. B. Goodenough and Y. Kim, *J. Power Sources*, 2011, **196**, 6688-6694.

15. Y.-C. Lu, B. M. Gallant, D. G. Kwabi, J. R. Harding, R. R. Mitchell, M. S. Whittingham and Y. Shao-Horn, *Energy Environ. Sci.*, 2013, **6**, 750-768.
16. Y. Wang and Y. Xia, *Nat. Chem.*, 2013, **5**, 445-447.
17. E. L. Littauer and K. C. Tsai, *J. Electrochem. Soc.*, 1976, **123**, 771-776.
18. E. L. Littauer and K. C. Tsai, *J. Electrochem. Soc.*, 1976, **123**, 964-969.
19. K. M. Abraham and Z. Jiang, *J. Electrochem. Soc.*, 1996, **143**, 1-5.
20. K. M. Abraham and Z. Jiang, ELC Laboratories, Inc., United States, 1996.
21. J. P. Zheng, R. Y. Liang, M. Hendrickson and E. J. Plichta, *J. Electrochem. Soc.*, 2008, **155**, A432-A437.
22. J. Christensen, P. Albertus, R. S. Sanchez-Carrera, T. Lohmann, B. Kozinsky, R. Liedtke, J. Ahmed and A. Kojic, *J. Electrochem. Soc.*, 2012, **159**, R1-R30.
23. G. Girishkumar, B. McCloskey, A. C. Luntz, S. Swanson and W. Wilcke, *J. Phys. Chem. Lett.*, 2010, **1**, 2193-2203.
24. L. J. Hardwick and P. G. Bruce, *Curr. Opin. Solid St. M.*, 2012, **16**, 178-185.
25. J. M. Tarascon and M. Armand, *Nature*, 2001, **414**, 359-367.
26. J. Goodenough, *J. Solid. State. Electr.*, 2012, **16**, 2019-2029.
27. B. Scrosati, J. Hassoun and Y.-K. Sun, *Energy Environ. Sci.*, 2011, **4**, 3287-3295.
28. S. D. Beattie, D. M. Manolescu and S. L. Blair, *J. Electrochem. Soc.*, 2009, **156**, A44-A47.
29. B. Richter, D. Goldston, G. Crabtree, L. Glicksman, D. Goldstein, D. Greene, D. Kammen, M. Levine, M. Lubell, M. Savitz and D. Sperling, eds., *Energy Future: Think Efficiency*, American Physical Society, College Park, MD, 2008.
30. S. J. Gerssen-Gondelach and A. P. C. Faaij, *J. Power Sources*, 2012, **212**, 111-129.
31. F. T. Wagner, B. Lakshmanan and M. F. Mathias, *J. Phys. Chem. Lett.*, 2010, **1**, 2204-2219.
32. L. Cecchetto, M. Salomon, B. Scrosati and F. Croce, *J. Power Sources*, 2012, **213**, 233-238.
33. W. Xu, J. Xiao, D. Wang, J. Zhang and J.-G. Zhang, *J. Electrochem. Soc.*, 2010, **157**, A219-A224.
34. Y. Chen, S. A. Freunberger, Z. Peng, F. Bardé and P. G. Bruce, *J. Am. Chem. Soc.*, 2012, **134**, 7952-7957.
35. J. Xiao, J. Hu, D. Wang, D. Hu, W. Xu, G. L. Graff, Z. Nie, J. Liu and J.-G. Zhang, *J. Power Sources*, 2011, **196**, 5674-5678.
36. C. O. Laoire, S. Mukerjee, K. M. Abraham, E. J. Plichta and M. A. Hendrickson, *J. Phys. Chem. C*, 2010, **114**, 9178-9186.
37. S. Visco, in *4th Symposium of Energy Storage: Beyond Lithium Ion*, Pacific Northwest National Laboratory, Richland, WA, 2011.
38. T. Zhang, N. Imanishi, Y. Takeda and O. Yamamoto, *Chem. Lett.*, 2011, **40**, 668-673.
39. P. He, Y. Wang and H. Zhou, *Chem. Commun.*, 2011, **47**, 10701-10703.
40. H. Wang, D. Im, D. J. Lee, M. Matsui, Y. Takeda, O. Yamamoto and N. Imanishi, *J. Electrochem. Soc.*, 2013, **160**, A728-A733.
41. T. Zhang, N. Imanishi, Y. Shimonishi, A. Hirano, J. Xie, Y. Takeda, O. Yamamoto and N. Sammes, *J. Electrochem. Soc.*, 2010, **157**, A214-A218.
42. T. Zhang, N. Imanishi, S. Hasegawa, A. Hirano, J. Xie, Y. Takeda, O. Yamamoto and N. Sammes, *J. Electrochem. Soc.*, 2008, **155**, A965-A969.
43. B. Horstmann, T. Danner and W. G. Bessler, *Energy Environ. Sci.*, 2013, **6**, 1299-1314.
44. T. Zhang, N. Imanishi, S. Hasegawa, A. Hirano, J. Xie, Y. Takeda, O. Yamamoto and N. Sammes, *Electrochem. Solid St.*, 2009, **12**, A132-A135.
45. L. Li, X. Zhao, Y. Fu and A. Manthiram, *Phys. Chem. Chem. Phys.*, 2012, **14**, 12737-12740.
46. N. Imanishi, Y. Takeda and O. Yamamoto, *Electrochemistry*, 2012, **80**, 706-715.
47. A. I. Demidov, V. K. Domanskii and A. G. Morachevskii, *Russ. J. Appl. Chem.*, 2001, **74**, 1118-1121.
48. P. He, Y. Wang and H. Zhou, *Electrochem. Commun.*, 2010, **12**, 1686-1689.
49. E. Yoo, J. Nakamura and H. Zhou, *Energy Environ. Sci.*, 2012, **5**, 6928-6932.
50. Y. Wang, R. Ohnishi, E. Yoo, P. He, J. Kubota, K. Domen and H. Zhou, *J. Mater. Chem.*, 2012, **22**, 15549-15555.
51. J. P. Zheng, P. Andrei, M. Hendrickson and E. J. Plichta, *J. Electrochem. Soc.*, 2011, **158**, A43-A46.
52. D. Wittmaier, N. Wagner, K. A. Friedrich, H. M. A. Amin and H. Baltruschat, *J. Power Sources*, 2014, **265**, 299-308.
53. N. Alias and A. A. Mohamad, *J. Power Sources*, 2015, **274**, 237-251.
54. P. Zhang, H. Wang, Y.-G. Lee, M. Matsui, Y. Takeda, O. Yamamoto and N. Imanishi, *J. Electrochem. Soc.*, 2015, **162**, A1265-A1271.
55. P. Kichambare, J. Kumar, S. Rodrigues and B. Kumar, *J. Power Sources*, 2011, **196**, 3310-3316.

56. B. Kumar, J. Kumar, R. Leese, J. P. Fellner, S. J. Rodrigues and K. M. Abraham, *J. Electrochem. Soc.*, 2010, **157**, A50-A54.
57. H. Kitaura and H. Zhou, *Energy Environ. Sci.*, 2012, **5**, 9077-9084.
58. H. Kitaura and H. Zhou, *Adv. Energy Mater.*, 2012, **2**, 889-894.
59. F. Li, H. Kitaura and H. Zhou, *Energy Environ. Sci.*, 2013, **6**, 2302-2311.
60. Q. Lu, Y. Gao, Q. Zhao, J. Li, X. Wang and F. Wang, *J. Power Sources*, 2013, **242**, 677-682.
61. I. S. Noor, S. R. Majid and A. K. Arof, *Electrochim. Acta*, 2013, **102**, 149-160.
62. G. Yu. Aleshin, D. A. Semenenko, A. I. Belova, T. K. Zakharchenko, D. M. Itkis, E. A. Goodilin and Y. D. Tretyakov, *Solid State Ionics*, 2011, **184**, 62-64.
63. L. Li, X. Zhao and A. Manthiram, *Electrochem. Commun.*, 2012, **14**, 78-81.
64. P. Kichambare, S. Rodrigues and J. Kumar, *ACS Appl. Mater. Inter.*, 2011, **4**, 49-52.
65. B. Kumar and J. Kumar, *J. Electrochem. Soc.*, 2010, **157**, A611-A616.
66. Y. Wang and H. Zhou, *J. Power Sources*, 2010, **195**, 358-361.
67. T. Zhang, N. Imanishi, Y. Shimonishi, A. Hirano, Y. Takeda, O. Yamamoto and N. Sannes, *Chem. Commun.*, 2010, **46**, 1661-1663.
68. R. Black, B. Adams and L. F. Nazar, *Adv. Energy Mater.*, 2012, **2**, 801-815.
69. H. He, W. Niu, N. M. Asl, J. Salim, R. Chen and Y. Kim, *Electrochim. Acta*, 2012, **67**, 87-94.
70. L. Li and A. Manthiram, *J. Mater. Chem. A*, 2013, **1**, 5121-5127.
71. K. Huang, Y. Li and Y. Xing, *Electrochim. Acta*, 2013, **103**, 44-49.
72. Y. Li, K. Huang and Y. Xing, *Electrochim. Acta*, 2012, **81**, 20-24.
73. Y. Wang, P. He and H. Zhou, *Energy Environ. Sci.*, 2011, **4**, 4994-4999.
74. Y. Wang and H. Zhou, *Electrochem. Commun.*, 2009, **11**, 1834-1837.
75. Y. Wang and H. Zhou, *Chem. Commun.*, 2010, **46**, 6305-6307.
76. P. He, Y. Wang and H. Zhou, *J. Power Sources*, 2011, **196**, 5611-5616.
77. E. Yoo and H. Zhou, *J. Power Sources*, 2013, **244**, 429-434.
78. E. Yoo and H. Zhou, *ACS Nano*, 2011, **5**, 3020-3026.
79. H. Zhou, Y. Wang, H. Li and P. He, *ChemSusChem*, 2010, **3**, 1009-1019.
80. E. Yoo and H. Zhou, *RSC Adv.*, 2014, **4**, 11798-11801.
81. L. Li and A. Manthiram, *Adv. Energy Mater.*, 2014, **4**, 1301795.
82. M. Mehta, V. Bevara and P. Andrei, *J. Power Sources*, 2015, **286**, 299-308.
83. T. Ogasawara, A. Débart, M. Holzzapfel, P. Novák and P. G. Bruce, *J. Am. Chem. Soc.*, 2006, **128**, 1390-1393.
84. J. Read, *J. Electrochem. Soc.*, 2002, **149**, A1190-A1195.
85. J. Read, *J. Electrochem. Soc.*, 2006, **153**, A96-A100.
86. J. Read, K. Mutolo, M. Ervin, W. Behl, J. Wolfenstine, A. Driedger and D. Foster, *J. Electrochem. Soc.*, 2003, **150**, A1351-A1356.
87. S. S. Zhang, X. Ren and J. Read, *Electrochim. Acta*, 2011, **56**, 4544-4548.
88. S. S. Zhang and J. Read, *J. Power Sources*, 2011, **196**, 2867-2870.
89. S. S. Zhang, X. Ren, D. T. Tran and J. Read, *Green*, 2012, **2**, 63-69.
90. X. Ren, S. S. Zhang, D. T. Tran and J. Read, *J. Mater. Chem.*, 2011, **21**, 10118-10125.
91. S. S. Zhang, D. Foster and J. Read, *J. Power Sources*, 2010, **195**, 1235-1240.
92. S. S. Zhang, K. Xu and J. Read, *J. Power Sources*, 2011, **196**, 3906-3910.
93. S. S. Zhang, D. Foster and J. Read, *Electrochim. Acta*, 2011, **56**, 1283-1287.
94. A. Débart, A. J. Paterson, J. Bao and P. G. Bruce, *Angew. Chem. Int. Edit.*, 2008, **47**, 4521-4524.
95. A. Débart, J. Bao, G. Armstrong and P. G. Bruce, *J. Power Sources*, 2007, **174**, 1177-1182.
96. S. A. Freunberger, Z. Peng, L. J. Hardwick, Y. Chen, F. Barde and P. Bruce, *ECS Meeting Abstracts*, 2010, **1002**, 340.
97. Z. Peng, S. A. Freunberger, Y. Chen and P. G. Bruce, *Science*, 2012, **337**, 563-566.
98. S. A. Freunberger, Y. Chen, Z. Peng, J. M. Griffin, L. J. Hardwick, F. Bardé, P. Novák and P. G. Bruce, *J. Am. Chem. Soc.*, 2011, **133**, 8040-8047.
99. Z. Peng, S. A. Freunberger, L. J. Hardwick, Y. Chen, V. Giordani, F. Bardé, P. Novák, D. Graham, J.-M. Tarascon and P. G. Bruce, *Angew. Chem. Int. Edit.*, 2011, **50**, 6351-6355.
100. S. A. Freunberger, Y. Chen, N. E. Drewett, L. J. Hardwick, F. Bardé and P. G. Bruce, *Angew. Chem. Int. Edit.*, 2011, **50**, 8609-8613.
101. M. M. Ottakam Thotiyl, S. A. Freunberger, Z. Peng and P. G. Bruce, *J. Am. Chem. Soc.*, 2013, **135**, 494-500.
102. L. Trahey, C. S. Johnson, J. T. Vaughey, S.-H. Kang, L. J. Hardwick, S. A. Freunberger, P. G. Bruce and M. M. Thackeray, *Electrochem. Solid St.*, 2011, **14**, A64-A66.

103. Y. Chen, S. A. Freunberger, Z. Peng, O. Fontaine and P. G. Bruce, *Nat. Chem.*, 2013, **5**, 489-494.
104. V. Giordani, S. A. Freunberger, P. G. Bruce, J. M. Tarascon and D. Larcher, *Electrochem. Solid St.*, 2010, **13**, A180-A183.
105. Y.-C. Lu, H. A. Gasteiger, M. C. Parent, V. Chiloyan and Y. Shao-Horn, *Electrochem. Solid St.*, 2010, **13**, A69-A72.
106. J. R. Harding, Y.-C. Lu, Y. Tsukada and Y. Shao-Horn, *Phys. Chem. Chem. Phys.*, 2012, **14**, 10540-10546.
107. Y.-C. Lu, H. A. Gasteiger and Y. Shao-Horn, *J. Am. Chem. Soc.*, 2011, **133**, 19048-19051.
108. J. Suntivich, H. A. Gasteiger, N. Yabuuchi, H. Nakanishi, J. B. Goodenough and Y. Shao-Horn, *Nat. Chem.*, 2011, **3**, 546-550.
109. Y.-C. Lu, H. A. Gasteiger and Y. Shao-Horn, *Electrochem. Solid St.*, 2011, **14**, A70-A74.
110. Y.-C. Lu, Z. Xu, H. A. Gasteiger, S. Chen, K. Hamad-Schifferli and Y. Shao-Horn, *J. Am. Chem. Soc.*, 2010, **132**, 12170-12171.
111. Y.-C. Lu, H. A. Gasteiger, E. Crumlin, R. McGuire and Y. Shao-Horn, *J. Electrochem. Soc.*, 2010, **157**, A1016-A1025.
112. H.-G. Jung, J. Hassoun, J.-B. Park, Y.-K. Sun and B. Scrosati, *Nat. Chem.*, 2012, **4**, 579-585.
113. J. Lu, Y. Lei, K. C. Lau, X. Luo, P. Du, J. Wen, R. S. Assary, U. Das, D. J. Miller, J. W. Elam, H. M. Albishri, D. A. El-Hady, Y.-K. Sun, L. A. Curtiss and K. Amine, *Nat. Commun.*, 2013, **4**, 2383.
114. H.-D. Lim, H. Song, J. Kim, H. Gwon, Y. Bae, K.-Y. Park, J. Hong, H. Kim, T. Kim, Y. H. Kim, X. Lepró, R. Ovalle-Robles, R. H. Baughman and K. Kang, *Angew. Chem. Int. Edit.*, 2014, **53**, 3926-3931.
115. M. M. Ottakam Thotiyil, S. A. Freunberger, Z. Peng, Y. Chen, Z. Liu and P. G. Bruce, *Nat. Mater.*, 2013, **12**, 1050-1056.
116. A. Kraytsberg and Y. Ein-Eli, *J. Power Sources*, 2011, **196**, 886-893.
117. Y. Shao, F. Ding, J. Xiao, J. Zhang, W. Xu, S. Park, J.-G. Zhang, Y. Wang and J. Liu, *Adv. Funct. Mater.*, 2013, **23**, 987-1004.
118. Y. Shao, S. Park, J. Xiao, J.-G. Zhang, Y. Wang and J. Liu, *ACS Catal.*, 2012, **2**, 844-857.
119. Z.-K. Luo, C.-S. Liang, F. Wang, Y.-H. Xu, J. Chen, D. Liu, H.-Y. Sun, H. Yang and X.-P. Fan, *Adv. Funct. Mater.*, 2014, **24**, 2101-2105.
120. J.-L. Shui, H.-H. Wang and D.-J. Liu, *Electrochem. Commun.*, 2013, **34**, 45-47.
121. I. C. Jang, Y. Hidaka and T. Ishihara, *J. Power Sources*, 2013, **244**, 606-609.
122. N. Imanishi, S. Hasegawa, T. Zhang, A. Hirano, Y. Takeda and O. Yamamoto, *J. Power Sources*, 2008, **185**, 1392-1397.
123. Y. Sun, *Nano Energy*, 2013, **2**, 801-816.
124. M. Zhang, K. Takahashi, I. Uechi, Y. Takeda, O. Yamamoto, D. Im, D.-J. Lee, B. Chi, J. Pu, J. Li and N. Imanishi, *J. Power Sources*, 2013, **235**, 117-121.
125. T. Zhang, S. Liu, N. Imanishi, A. Hirano, Y. Takeda and O. Yamamoto, *Electrochemistry.*, 2010, **78**, 360-362.
126. T. Zhang, N. Imanishi, A. Hirano, Y. Takeda and O. Yamamoto, *Electrochem. Solid St.*, 2011, **14**, A45-A48.
127. Y. Shimonishi, T. Zhang, P. Johnson, N. Imanishi, A. Hirano, Y. Takeda, O. Yamamoto and N. Sammes, *J. Power Sources*, 2010, **195**, 6187-6191.
128. T. T. Truong, Y. Qin, Y. Ren, Z. Chen, M. K. Chan, J. P. Greeley, K. Amine and Y. Sun, *Adv. Mater.*, 2011, **23**, 4947-4952.
129. R. Younesi, M. Hahlin, M. Roberts and K. Edström, *J. Power Sources*, 2013, **225**, 40-45.
130. J.-L. Shui, J. S. Okasinski, P. Kenesei, H. A. Dobbs, D. Zhao, J. D. Almer and D.-J. Liu, *Nat. Commun.*, 2013, **4**, 2255.
131. R. S. Assary, J. Lu, P. Du, X. Luo, X. Zhang, Y. Ren, L. A. Curtiss and K. Amine, *ChemSusChem*, 2013, **6**, 51-55.
132. K. Yoo, S. Banerjee and P. Dutta, *J. Power Sources*, 2014, **258**, 340-350.
133. X.-H. Yang and Y.-Y. Xia, *J. Solid. State. Electr.*, 2010, **14**, 109-114.
134. M. Mirzaeian, P. J. Hall, F. B. Sillars, I. Fletcher, M. M. Goldin, G. O. Shitta-bey and H. F. Jirandehi, *J. Electrochem. Soc.*, 2013, **160**, A25-A30.
135. S. Meini, M. Piana, N. Tsiouvaras, A. Garsuch and H. A. Gasteiger, *Electrochem. Solid St.*, 2012, **15**, A45-A48.
136. J.-B. Park, J. Hassoun, H.-G. Jung, H.-S. Kim, C. S. Yoon, I.-H. Oh, B. Scrosati and Y.-K. Sun, *Nano Lett.*, 2013, **13**, 2971-2975.
137. M. Song, D. Zhu, L. Zhang, X. Wang, L. Huang, Q. Shi, R. Mi, H. Liu, J. Mei, L. M. Lau and Y. Chen, *J. Solid. State. Electr.*, 2013, **17**, 2061-2069.

138. S. K. Das, S. Xu, A.-H. Emwas, Y. Y. Lu, S. Srivastava and L. A. Archer, *Energy Environ. Sci.*, 2012, **5**, 8927-8931.
139. Y. Li, Y. Yin, K. Guo, X. Xue, Z. Zou, X. Li, T. He and H. Yang, *J. Power Sources*, 2013, **241**, 288-294.
140. O. Crowther and M. Salomon, *Membranes*, 2012, **2**, 216-227.
141. J. Kumar and B. Kumar, *J. Power Sources*, 2009, **194**, 1113-1119.
142. Z. Fu, Z. Wei, X. Lin, T. Huang and A. Yu, *Electrochim. Acta*, 2012, **78**, 195-199.
143. S. R. Gowda, A. Brunet, G. M. Wallraff and B. D. McCloskey, *J. Phys. Chem. Lett.*, 2012, **4**, 276-279.
144. H.-K. Lim, H.-D. Lim, K.-Y. Park, D.-H. Seo, H. Gwon, J. Hong, W. A. Goddard, H. Kim and K. Kang, *J. Am. Chem. Soc.*, 2013, **135**, 9733-9742.
145. Z. Guo, X. Dong, S. Yuan, Y. Wang and Y. Xia, *J. Power Sources*, 2014, **264**, 1-7.
146. E. Nasybulin, W. Xu, M. H. Engelhard, Z. Nie, X. S. Li and J.-G. Zhang, *J. Power Sources*, 2013, **243**, 899-907.
147. H. Cheng and K. Scott, *Electrochim. Acta*, 2014, **116**, 51-58.
148. Y. Wang, D. Zheng, X.-Q. Yang and D. Qu, *Energy Environ. Sci.*, 2011, **4**, 3697-3702.
149. E. Quartarone and P. Mustarelli, *Chem. Soc. Rev.*, 2011, **40**, 2525-2540.
150. W. Xu, J. Xiao, D. Wang, J. Zhang and J.-G. Zhang, *Electrochem. Solid St.*, 2010, **13**, A48-A51.
151. N.-S. Choi, G. Jeong, B. Koo, Y.-W. Lee and K. T. Lee, *J. Power Sources*, 2013, **225**, 95-100.
152. B. G. Kim, J.-N. Lee, D. J. Lee, J.-K. Park and J. W. Choi, *ChemSusChem*, 2013, **6**, 443-448.
153. V. S. Bryantsev, J. Uddin, V. Giordani, W. Walker, D. Addison and G. V. Chase, *J. Electrochem. Soc.*, 2013, **160**, A160-A171.
154. K. Xu, *Chem. Rev.*, 2004, **104**, 4303-4418.
155. D. Sharon, V. Etacheri, A. Garsuch, M. Afri, A. A. Frimer and D. Aurbach, *J. Phys. Chem. Lett.*, 2012, **4**, 127-131.
156. G. M. Veith, J. Nanda, L. H. Delmau and N. J. Dudney, *J. Phys. Chem. Lett.*, 2012, **3**, 1242-1247.
157. F. Wang, C.-S. Liang, Y. Pang, Y.-H. Xu and Z.-K. Luo, *Ionics*, 2013, **19**, 1791-1793.
158. P. Du, J. Lu, K. C. Lau, X. Luo, J. Bareno, X. Zhang, Y. Ren, Z. Zhang, L. A. Curtiss, Y.-K. Sun and K. Amine, *Phys. Chem. Chem. Phys.*, 2013, **15**, 5572-5581.
159. E. Nasybulin, W. Xu, M. H. Engelhard, Z. Nie, S. D. Burton, L. Cosimbescu, M. E. Gross and J.-G. Zhang, *J. Phys. Chem. C*, 2013, **117**, 2635-2645.
160. W. Walker, V. Giordani, J. Uddin, V. S. Bryantsev, G. V. Chase and D. Addison, *J. Am. Chem. Soc.*, 2013, **135**, 2076-2079.
161. C. O. Laoire, S. Mukerjee, E. J. Plichta, M. A. Hendrickson and K. M. Abraham, *J. Electrochem. Soc.*, 2011, **158**, A302-A308.
162. O. Crowther, D. Keeny, D. M. Moureau, B. Meyer, M. Salomon and M. Hendrickson, *J. Power Sources*, 2012, **202**, 347-351.
163. Z. H. Cui, W. G. Fan and X. X. Guo, *J. Power Sources*, 2013, **235**, 251-255.
164. H. Liu and Y. Xing, *Electrochem. Commun.*, 2011, **13**, 646-649.
165. R. Younesi, M. Hahlin and K. Edström, *ACS Appl. Mater. Inter.*, 2013, **5**, 1333-1341.
166. F. Li, T. Zhang, Y. Yamada, A. Yamada and H. Zhou, *Adv. Energy Mater.*, 2013, **3**, 532-538.
167. P. G. Bruce, *Solid State Ionics*, 2008, **179**, 752-760.
168. M. Armand and J. M. Tarascon, *Nature*, 2008, **451**, 652-657.
169. M. A. Rahman, X. Wang and C. Wen, *J. Appl. Electrochem.*, 2014, **44**, 5-22.
170. K. M. Abraham, *ECS Trans.*, 2008, **3**, 67-71.
171. J. M. W. Chase, *J. Phys. Chem. Ref. Data*, 1998, **No.9**, 1510-1511.
172. J. S. Hummelshøj, J. Blomqvist, S. Datta, T. Vegge, J. Rossmeisl, K. S. Thygesen, A. C. Luntz, K. W. Jacobsen and J. K. Nørskov, *J. Chem. Phys.*, 2010, **132**, 071101.
173. C. O. Laoire, S. Mukerjee, K. M. Abraham, E. J. Plichta and M. A. Hendrickson, *J. Phys. Chem. C*, 2009, **113**, 20127-20134.
174. J. M. W. Chase, *J. Phys. Chem. Ref. Data*, 1998, **No.9**, 1506-1509.
175. X.-H. Yang, P. He and Y.-Y. Xia, *Electrochem. Commun.*, 2009, **11**, 1127-1130.
176. P. Tan, Z. Wei, W. Shyy and T. S. Zhao, *Appl. Energ.*, 2013, **109**, 275-282.
177. D. Zhai, H.-H. Wang, J. Yang, K. C. Lau, K. Li, K. Amine and L. A. Curtiss, *J. Am. Chem. Soc.*, 2013, **135**, 15364-15372.
178. B. M. Gallant, D. G. Kwabi, R. R. Mitchell, J. Zhou, C. V. Thompson and Y. Shao-Horn, *Energy Environ. Sci.*, 2013, **6**, 2518-2528.
179. B. D. Adams, C. Radtke, R. Black, M. L. Trudeau, K. Zaghbi and L. F. Nazar, *Energy Environ. Sci.*, 2013, **6**, 1772-1778.

180. R. Black, S. H. Oh, J.-H. Lee, T. Yim, B. Adams and L. F. Nazar, *J. Am. Chem. Soc.*, 2012, **134**, 2902-2905.
181. D. Zhai, K. C. Lau, H.-H. Wang, J. Wen, D. J. Miller, J. Lu, F. Kang, B. Li, W. Yang, J. Gao, E. Indacochea, L. A. Curtiss and K. Amine, *Nano Lett.*, 2015, **15**, 1041-1046.
182. D. T. Sawyer, G. Chiericato, C. T. Angelis, E. J. Nanni and T. Tsuchiya, *Anal. Chem.*, 1982, **54**, 1720-1724.
183. D. Aurbach, M. Daroux, P. Faguy and E. Yeager, *J. Electron. Chem. Interfa. Electrochem.*, 1991, **297**, 225-244.
184. T. Fujinaga and S. Sakura, *B. Chem. Soc. Jpn.*, 1974, **47**, 2781-2786.
185. J. Hassoun, F. Croce, M. Armand and B. Scrosati, *Angew. Chem. Int. Edit.*, 2011, **50**, 2999-3002.
186. B. D. McCloskey, R. Scheffler, A. Speidel, G. Girishkumar and A. C. Luntz, *J. Phys. Chem. C*, 2012, **116**, 23897-23905.
187. R. Cao, E. D. Walter, W. Xu, E. N. Nasybulin, P. Bhattacharya, M. E. Bowden, M. H. Engelhard and J.-G. Zhang, *ChemSusChem*, 2014, **7**, 2436-2440.
188. K.-H. Xue, E. McTurk, L. Johnson, P. G. Bruce and A. A. Franco, *J. Electrochem. Soc.*, 2015, **162**, A614-A621.
189. S. H. Oh, R. Black, E. Pomerantseva, J.-H. Lee and L. F. Nazar, *Nat. Chem.*, 2012, **4**, 1004-1010.
190. Y. Yang, Q. Sun, Y.-S. Li, H. Li and Z.-W. Fu, *J. Power Sources*, 2013, **223**, 312-318.
191. C. J. Barile and A. A. Gewirth, *J. Electrochem. Soc.*, 2013, **160**, A549-A552.
192. U. Sahapatombut, H. Cheng and K. Scott, *J. Power Sources*, 2013, **243**, 409-418.
193. A. K. Thapa, K. Saimen and T. Ishihara, *Electrochem. Solid St.*, 2010, **13**, A165-A167.
194. R. Black, J.-H. Lee, B. Adams, C. A. Mims and L. F. Nazar, *Angew. Chem. Int. Edit.*, 2013, **52**, 392-396.
195. T. Zhang and H. Zhou, *Nat. Commun.*, 2013, **4**, 1817.
196. J.-H. Lee, R. Black, G. Popov, E. Pomerantseva, F. Nan, G. A. Botton and L. F. Nazar, *Energy Environ. Sci.*, 2012, **5**, 9558-9565.
197. K. R. Ryan, L. Trahey, J. S. Okasinski, A. K. Burrell and B. J. Ingram, *J. Mater. Chem. A*, 2013, **1**, 6915-6919.
198. J. Yang, D. Zhai, H.-H. Wang, K. C. Lau, J. A. Schlueter, P. Du, D. J. Myers, Y.-K. Sun, L. A. Curtiss and K. Amine, *Phys. Chem. Chem. Phys.*, 2013, **15**, 3764-3771.
199. S. Higashi, Y. Kato, K. Takechi, H. Nakamoto, F. Mizuno, H. Nishikoori, H. Iba and T. Asaoka, *J. Power Sources*, 2013, **240**, 14-17.
200. L. Zhong, R. R. Mitchell, Y. Liu, B. M. Gallant, C. V. Thompson, J. Y. Huang, S. X. Mao and Y. Shao-Horn, *Nano Lett.*, 2013, **13**, 2209-2214.
201. Y. Qin, J. Lu, P. Du, Z. Chen, Y. Ren, T. Wu, J. T. Miller, J. Wen, D. J. Miller, Z. Zhang and K. Amine, *Energy Environ. Sci.*, 2013, **6**, 519-531.
202. K. Zhang, L. Zhang, X. Chen, X. He, X. Wang, S. Dong, P. Han, C. Zhang, S. Wang, L. Gu and G. Cui, *J. Phys. Chem. C*, 2012, **117**, 858-865.
203. V. Etacheri, D. Sharon, A. Garsuch, M. Afri, A. A. Frimer and D. Aurbach, *J. Mater. Chem. A*, 2013, **1**, 5021-5030.
204. X. Lin, L. Zhou, T. Huang and A. Yu, *J. Mater. Chem. A*, 2013, **1**, 1239-1245.
205. F. Li, R. Ohnishi, Y. Yamada, J. Kubota, K. Domen, A. Yamada and H. Zhou, *Chem. Commun.*, 2013, **49**, 1175-1177.
206. L. A. Huff, J. L. Rapp, L. Zhu and A. A. Gewirth, *J. Power Sources*, 2013, **235**, 87-94.
207. R. Wen, M. Hong and H. R. Byon, *J. Am. Chem. Soc.*, 2013, **135**, 10870-10876.
208. S. E. Herrera, A. Y. Tesio, R. Clarenc and E. J. Calvo, *Phys. Chem. Chem. Phys.*, 2014, **16**, 9925-9929.
209. R. Wen and H. R. Byon, *Chem. Commun.*, 2014, **50**, 2628-2631.
210. N. Tsiouvaras, S. Meini, I. Buchberger and H. A. Gasteiger, *J. Electrochem. Soc.*, 2013, **160**, A471-A477.
211. F. Mizuno, S. Nakanishi, Y. Kotani, S. Yokoishi and H. Iba, *Electrochemistry*, 2010, **78**, 403-405.
212. M. J. Trahan, Q. Jia, S. Mukerjee, E. J. Plichta, M. A. Hendrickson and K. M. Abraham, *J. Electrochem. Soc.*, 2013, **160**, A1577-A1586.
213. Y. S. Cohen, Y. Cohen and D. Aurbach, *J. Phys. Chem. B*, 2000, **104**, 12282-12291.
214. C. K. Park, S. B. Park, S. Y. Lee, H. Lee, H. Jang and W. I. Cho, *Bull. Korean Chem. Soc.*, 2010, **31**, 3221-3224.
215. M. Eswaran, N. Munichandraiah and L. G. Scanlon, *Electrochem. Solid St.*, 2010, **13**, A121-A124.
216. S. Ida, A. K. Thapa, Y. Hidaka, Y. Okamoto, M. Matsuka, H. Hagiwara and T. Ishihara, *J. Power Sources*, 2012, **203**, 159-164.

217. A. K. Thapa, T. H. Shin, S. Ida, G. U. Sumanasekera, M. K. Sunkara and T. Ishihara, *J. Power Sources*, 2012, **220**, 211-216.
218. T. Laino and A. Curioni, *Chem.-Eur. J.*, 2012, **18**, 3510-3520.
219. J. Herranz, A. Garsuch and H. A. Gasteiger, *J. Phys. Chem. C*, 2012, **116**, 19084-19094.
220. W. Xu, V. V. Viswanathan, D. Wang, S. A. Towne, J. Xiao, Z. Nie, D. Hu and J.-G. Zhang, *J. Power Sources*, 2011, **196**, 3894-3899.
221. G. M. Veith, N. J. Dudney, J. Howe and J. Nanda, *J. Phys. Chem. C*, 2011, **115**, 14325-14333.
222. B. M. Gallant, R. R. Mitchell, D. G. Kwabi, J. Zhou, L. Zuin, C. V. Thompson and Y. Shao-Horn, *J. Phys. Chem. C*, 2012, **116**, 20800-20805.
223. J.-L. Shui, J. Okasinski, D. Zhao, J. Almer and D.-J. Liu, *ECS Trans.*, 2013, **50**, 37-45.
224. W. Xu, K. Xu, V. V. Viswanathan, S. A. Towne, J. S. Hardy, J. Xiao, Z. Nie, D. Hu, D. Wang and J.-G. Zhang, *J. Power Sources*, 2011, **196**, 9631-9639.
225. H. Nakamoto, Y. Suzuki, T. Shiotsuki, F. Mizuno, S. Higashi, K. Takechi, T. Asaoka, H. Nishikoori and H. Iba, *J. Power Sources*, 2013, **243**, 19-23.
226. O. Crowther, B. Meyer and M. Salomon, *Electrochem. Solid St.*, 2011, **14**, A113-A115.
227. H.-D. Lim, K.-Y. Park, H. Gwon, J. Hong, H. Kim and K. Kang, *Chem. Commun.*, 2012, **48**, 8374-8376.
228. J. Xiao, D. Mei, X. Li, W. Xu, D. Wang, G. L. Graff, W. D. Bennett, Z. Nie, L. V. Saraf, I. A. Aksay, J. Liu and J.-G. Zhang, *Nano Lett.*, 2011, **11**, 5071-5078.
229. B. D. McCloskey, D. S. Bethune, R. M. Shelby, G. Girishkumar and A. C. Luntz, *J. Phys. Chem. Lett.*, 2011, **2**, 1161-1166.
230. Y.-C. Lu, D. G. Kwabi, K. P. C. Yao, J. R. Harding, J. Zhou, L. Zuin and Y. Shao-Horn, *Energy Environ. Sci.*, 2011, **4**, 2999-3007.
231. B. McCloskey, A. Speidel, R. Scheffler, D. Miller, V. Viswanathan, J. Hummelshøj, J. Nørskov and A. Luntz, *J. Phys. Chem. Lett.*, 2012, **3**, 997-1001.
232. J. M. García, H. W. Horn and J. E. Rice, *J. Phys. Chem. Lett.*, 2015, 1795-1799.
233. M. J. Trahan, S. Mukerjee, E. J. Plichta, M. A. Hendrickson and K. M. Abraham, *J. Electrochem. Soc.*, 2013, **160**, A259-A267.
234. D. Xu, Z.-L. Wang, J.-J. Xu, L.-L. Zhang and X.-B. Zhang, *Chem. Commun.*, 2012, **48**, 6948-6950.
235. C. Liang, F. Wang, Y. Xu, J. Chen, D. Liu and Z. Luo, *New J. Chem.*, 2013, **37**, 2568-2572.
236. D. Xu, Z.-L. Wang, J.-J. Xu, L.-L. Zhang, L.-M. Wang and X.-B. Zhang, *Chem. Commun.*, 2012, **48**, 11674-11676.
237. M. Leskes, N. E. Drewett, L. J. Hardwick, P. G. Bruce, G. R. Goward and C. P. Grey, *Angew. Chem.*, 2012, **124**, 8688-8691.
238. H. Lim, E. Yilmaz and H. R. Byon, *J. Phys. Chem. Lett.*, 2012, **3**, 3210-3215.
239. R. S. Assary, K. C. Lau, K. Amine, Y.-K. Sun and L. A. Curtiss, *J. Phys. Chem. C*, 2013, **117**, 8041-8049.
240. K. R. Ryan, L. Trahey, B. J. Ingram and A. K. Burrell, *J. Phys. Chem. C*, 2012, **116**, 19724-19728.
241. R. Younesi, P. Norby and T. Vegge, *ECS Electrochem. Lett.*, 2014, **3**, A15-A18.
242. W. Xu, J. Hu, M. H. Engelhard, S. A. Towne, J. S. Hardy, J. Xiao, J. Feng, M. Y. Hu, J. Zhang, F. Ding, M. E. Gross and J.-G. Zhang, *J. Power Sources*, 2012, **215**, 240-247.
243. V. Y. Nimon, S. J. Visco, L. C. De Jonghe, Y. M. Volfkovich and D. A. Bograchev, *ECS Electrochem. Lett.*, 2013, **2**, A33-A35.
244. V. S. Bryantsev, V. Giordani, W. Walker, J. Uddin, I. Lee, A. C. T. van Duin, G. V. Chase and D. Addison, *J. Phys. Chem. C*, 2013, **117**, 11977-11988.
245. T. Kuboki, T. Okuyama, T. Ohsaki and N. Takami, *J. Power Sources*, 2005, **146**, 766-769.
246. H. Ye, J. Huang, J. J. Xu, A. Khalfan and S. G. Greenbaum, *J. Electrochem. Soc.*, 2007, **154**, A1048-A1057.
247. K. Cai, W. Pu, Y. Gao, J. Hou, C. Deng, C. Wang and Z. Mao, *Int. J. Hydrogen Energ.*, 2013, **38**, 11023-11027.
248. F. De Giorgio, F. Soavi and M. Mastragostino, *Electrochem. Commun.*, 2011, **13**, 1090-1093.
249. D. G. Kwabi, N. Ortiz-Vitoriano, S. A. Freunberger, Y. Chen, N. Imanishi, P. G. Bruce and Y. Shao-Horn, *Mrs. Bull.*, 2014, **39**, 443-452.
250. C. J. Allen, J. Hwang, R. Kautz, S. Mukerjee, E. J. Plichta, M. A. Hendrickson and K. M. Abraham, *J. Phys. Chem. C*, 2012, **116**, 20755-20764.
251. F. Mizuno, K. Takechi, S. Higashi, T. Shiga, T. Shiotsuki, N. Takazawa, Y. Sakurabayashi, S. Okazaki, I. Nitta, T. Kodama, H. Nakamoto, H. Nishikoori, S. Nakanishi, Y. Kotani and H. Iba, *J. Power Sources*, 2013, **228**, 47-56.

252. S. Meini, S. Solchenbach, M. Piana and H. A. Gasteiger, *J. Electrochem. Soc.*, 2014, **161**, A1306-A1314.
253. G. A. Elia, J. Hassoun, W. J. Kwak, Y. K. Sun, B. Scrosati, F. Mueller, D. Bresser, S. Passerini, P. Oberhumer, N. Tsiouvaras and J. Reiter, *Nano Lett.*, 2014, **14**, 6572-6577.
254. M. Balaish, A. Kraysberg and Y. Ein-Eli, *Phys. Chem. Chem. Phys.*, 2014, **16**, 2801-2822.
255. C. Li, O. Fontaine, S. A. Freunberger, L. Johnson, S. Grugeon, S. Laruelle, P. G. Bruce and M. Armand, *J. Phys. Chem. C*, 2014, **118**, 3393-3401.
256. V. S. Bryantsev, V. Giordani, W. Walker, M. Blanco, S. Zecevic, K. Sasaki, J. Uddin, D. Addison and G. V. Chase, *J. Phys. Chem. A*, 2011, **115**, 12399-12409.
257. G. A. Elia, J.-B. Park, Y.-K. Sun, B. Scrosati and J. Hassoun, *ChemElectroChem*, 2014, **1**, 47-50.
258. I. Gunasekara, S. Mukerjee, E. J. Plichta, M. A. Hendrickson and K. M. Abraham, *J. Electrochem. Soc.*, 2014, **161**, A381-A392.
259. D. S. Kim and Y. J. Park, *J. Alloy. Compd.*, 2014, **591**, 164-169.
260. B. Sun, X. Huang, S. Chen, J. Zhang and G. Wang, *RSC Adv.*, 2014, **4**, 11115-11120.
261. V. S. Bryantsev, J. Uddin, V. Giordani, W. Walker, G. V. Chase and D. Addison, *J. Am. Chem. Soc.*, 2014, **136**, 3087-3096.
262. D. Chalasani and B. L. Lucht, *ECS Electrochem. Lett.*, 2012, **1**, A38-A42.
263. X. Guo and N. Zhao, *Adv. Energy Mater.*, 2013, **3**, 1413-1416.
264. D. M. Itkis, D. A. Semenenko, E. Y. Kataev, A. I. Belova, V. S. Neudachina, A. P. Sirotnina, M. Hävecker, D. Teschner, A. Knop-Gericke, P. Dudin, A. Barinov, E. A. Goodilin, Y. Shao-Horn and L. V. Yashina, *Nano Lett.*, 2013, **13**, 4697-4701.
265. R. Younesi, M. Hahlin, M. Treskow, J. Scheers, P. Johansson and K. Edström, *J. Phys. Chem. C*, 2012, **116**, 18597-18604.
266. R. Younesi, S. Urbonaite, K. Edström and M. Hahlin, *J. Phys. Chem. C*, 2012, **116**, 20673-20680.
267. Z. Zhang, J. Lu, R. S. Assary, P. Du, H.-H. Wang, Y.-K. Sun, Y. Qin, K. C. Lau, J. Greeley, P. C. Redfern, H. Iddir, L. A. Curtiss and K. Amine, *J. Phys. Chem. C*, 2011, **115**, 25535-25542.
268. V. S. Bryantsev, *Chem. Phys. Lett.*, 2013, **558**, 42-47.
269. J. M. Garcia-Lastra, J. Bass and K. S. Thygesen, *J. Chem. Phys.*, 2011, **135**, 121101.
270. O. Gerbig, R. Merkle and J. Maier, *Adv. Mater.*, 2013, **25**, 3129-3133.
271. M.-K. Song, S. Park, F. M. Alamgir, J. Cho and M. Liu, *Mater. Sci. Eng. R*, 2011, **72**, 203-252.
272. M. Radin, F. Tian and D. Siegel, *J. Mater. Sci.*, 2012, **47**, 7564-7570.
273. M. D. Radin, J. F. Rodriguez, F. Tian and D. J. Siegel, *J. Am. Chem. Soc.*, 2012, **134**, 1093-1103.
274. J. M. Garcia-Lastra, J. S. G. Myrdal, R. Christensen, K. S. Thygesen and T. Vegge, *J. Phys. Chem. C*, 2013, **117**, 5568-5577.
275. S. P. Ong, Y. Mo and G. Ceder, *Phys. Rev. B*, 2012, **85**, 081105.
276. J. Chen, J. S. Hummelshøj, K. S. Thygesen, J. S. G. Myrdal, J. K. Nørskov and T. Vegge, *Catal. Today*, 2011, **165**, 2-9.
277. B. D. McCloskey, D. S. Bethune, R. M. Shelby, T. Mori, R. Scheffler, A. Speidel, M. Sherwood and A. C. Luntz, *J. Phys. Chem. Lett.*, 2012, **3**, 3043-3047.
278. K. C. Lau, R. S. Assary, P. Redfern, J. Greeley and L. A. Curtiss, *J. Phys. Chem. C*, 2012, **116**, 23890-23896.
279. Y. Mo, S. P. Ong and G. Ceder, *Phys. Rev. B*, 2011, **84**, 205446.
280. U. Sahapatombut, H. Cheng and K. Scott, *J. Power Sources*, 2013, **227**, 243-253.
281. W. Fan, Z. Cui and X. Guo, *J. Phys. Chem. C*, 2013, **117**, 2623-2627.
282. H.-G. Jung, H.-S. Kim, J.-B. Park, I.-H. Oh, J. Hassoun, C. S. Yoon, B. Scrosati and Y.-K. Sun, *Nano Lett.*, 2012, **12**, 4333-4335.
283. B. Sun, J. Zhang, P. Munroe, H.-J. Ahn and G. Wang, *Electrochem. Commun.*, 2013, **31**, 88-91.
284. Z.-L. Wang, D. Xu, J.-J. Xu, L.-L. Zhang and X.-B. Zhang, *Adv. Funct. Mater.*, 2012, **22**, 3699-3705.
285. Y. Cui, Z. Wen and Y. Liu, *Energy Environ. Sci.*, 2011, **4**, 4727-4734.
286. L. Zhang, S. Zhang, K. Zhang, G. Xu, X. He, S. Dong, Z. Liu, C. Huang, L. Gu and G. Cui, *Chem. Commun.*, 2013, **49**, 3540-3542.
287. R. R. Mitchell, B. M. Gallant, C. V. Thompson and Y. Shao-Horn, *Energy Environ. Sci.*, 2011, **4**, 2952-2958.
288. C. N. Chervin, M. J. Wattendorf, J. W. Long, N. W. Kucko and D. R. Rolison, *J. Electrochem. Soc.*, 2013, **160**, A1510-A1516.
289. J. Li, H. Zhang, Y. Zhang, M. Wang, F. Zhang and H. Nie, *Nanoscale*, 2013, **5**, 4647-4651.
290. K. Zhang, L. Zhang, X. Chen, X. He, X. Wang, S. Dong, L. Gu, Z. Liu, C. Huang and G. Cui, *ACS Appl. Mater. Inter.*, 2013, **5**, 3677-3682.

291. Y. Yu, B. Zhang, Y.-B. He, Z.-D. Huang, S.-W. Oh and J.-K. Kim, *J. Mater. Chem. A*, 2013, **1**, 1163-1170.
292. G. Q. Zhang, J. P. Zheng, R. Liang, C. Zhang, B. Wang, M. Au, M. Hendrickson and E. J. Plichta, *J. Electrochem. Soc.*, 2011, **158**, A822-A827.
293. W.-M. Liu, T.-T. Gao, Y. Yang, Q. Sun and Z.-W. Fu, *Phys. Chem. Chem. Phys.*, 2013, **15**, 15806-15810.
294. L. D. Griffith, A. E. S. Sleightholme, J. F. Mansfield, D. J. Siegel and C. W. Monroe, *ACS Appl. Mater. Inter.*, 2015, **7**, 7670-7678.
295. R. R. Mitchell, B. M. Gallant, Y. Shao-Horn and C. V. Thompson, *J. Phys. Chem. Lett.*, 2013, **4**, 1060-1064.
296. Y. Liu, L. M. Suo, H. Lin, W. Yang, Y. Fang, X. Liu, D. Wang, Y.-S. Hu, W. Han and L. Chen, *J. Mater. Chem. A*, 2014, **2**, 9020-9024.
297. J. Nanda, H. Bilheux, S. Voisin, G. M. Veith, R. Archibald, L. Walker, S. Allu, N. J. Dudney and S. Pannala, *J. Phys. Chem. C*, 2012, **116**, 8401-8408.
298. G. Q. Zhang, J. P. Zheng, R. Liang, C. Zhang, B. Wang, M. Hendrickson and E. J. Plichta, *J. Electrochem. Soc.*, 2010, **157**, A953-A956.
299. Y. Li, J. Wang, X. Li, D. Geng, M. N. Banis, R. Li and X. Sun, *Electrochem. Commun.*, 2012, **18**, 12-15.
300. D. Capsoni, M. Bini, S. Ferrari, E. Quartarone and P. Mustarelli, *J. Power Sources*, 2012, **220**, 253-263.
301. S. Monaco, F. Soavi and M. Mastragostino, *J. Phys. Chem. Lett.*, 2013, **4**, 1379-1382.
302. E. M. Ryan, K. Ferris, A. Tartakovsky and M. Khaleel, *ECS Trans.*, 2013, **45**, 123-136.
303. P. Andrei, J. P. Zheng, M. Hendrickson and E. J. Plichta, *J. Electrochem. Soc.*, 2010, **157**, A1287-A1295.
304. R. Padbury and X. Zhang, *J. Power Sources*, 2011, **196**, 4436-4444.
305. Z. Ma, X. Yuan, H.-D. Sha, Z.-F. Ma and Q. Li, *Int. J. Hydrogen Energ.*, 2013, **38**, 11004-11010.
306. P. Albertus, G. Girishkumar, B. McCloskey, R. S. Sánchez-Carrera, B. Kozinsky, J. Christensen and A. C. Luntz, *J. Electrochem. Soc.*, 2011, **158**, A343-A351.
307. V. Viswanathan, K. S. Thygesen, J. S. Hummelshøj, J. K. Nørskov, G. Girishkumar, B. D. McCloskey and A. C. Luntz, *J. Chem. Phys.*, 2011, **135**, 214704.
308. H. Cheng and K. Scott, *J. Power Sources*, 2010, **195**, 1370-1374.
309. F. Cheng and J. Chen, *Nat. Chem.*, 2012, **4**, 962-963.
310. J. S. Hummelshøj, A. C. Luntz and J. K. Nørskov, *J. Chem. Phys.*, 2013, **138**, 034703.
311. Y. Cui, Z. Wen, X. Liang, Y. Lu, J. Jin, M. Wu and X. Wu, *Energy Environ. Sci.*, 2012, **5**, 7893-7897.
312. J.-J. Xu, D. Xu, Z.-L. Wang, H.-G. Wang, L.-L. Zhang and X.-B. Zhang, *Angew. Chem. Int. Edit.*, 2013, **52**, 3887-3890.
313. J. Hou, M. Yang, M. W. Ellis, R. B. Moore and B. Yi, *Phys. Chem. Chem. Phys.*, 2012, **14**, 13487-13501.
314. T. Schied, H. Ehrenberg, J. Eckert, S. Oswald, M. Hoffmann and F. Scheiba, *J. Power Sources*, 2014, **269**, 825-833.
315. H. Ohkuma, I. Uechi, M. Matsui, Y. Takeda, O. Yamamoto and N. Imanishi, *J. Power Sources*, 2014, **245**, 947-952.
316. Y. Wang and S. C. Cho, *J. Electrochem. Soc.*, 2013, **160**, A1847-A1855.
317. M. Hayashi, H. Minowa, M. Takahashi and T. Shodai, *Electrochemistry*, 2010, **78**, 325-328.
318. P. Andrei, J. P. Zheng, M. Hendrickson and E. J. Plichta, *J. Electrochem. Soc.*, 2012, **159**, A770-A780.
319. Y. Zhang, H. Zhang, J. Li, M. Wang, H. Nie and F. Zhang, *J. Power Sources*, 2013, **240**, 390-396.
320. D. Zheng, X.-Q. Yang and D. Qu, *Chem. Asian J.*, 2011, **6**, 3306-3311.
321. J. Wang, Y. Li and X. Sun, *Nano Energy*, 2013, **2**, 443-467.
322. L. Jin, L. Xu, C. Morein, C.-H. Chen, M. Lai, S. Dharmarathna, A. Doble and S. L. Suib, *Adv. Funct. Mater.*, 2010, **20**, 3373-3382.
323. M.-S. Park, J.-H. Kim, K. J. Kim, G. Jeong and Y.-J. Kim, *J. Nanosci Nanotechnol.*, 2013, **13**, 3611-3616.
324. Z.-S. Wu, W. Ren, L. Wen, L. Gao, J. Zhao, Z. Chen, G. Zhou, F. Li and H.-M. Cheng, *ACS Nano*, 2010, **4**, 3187-3194.
325. A. L. M. Reddy, M. M. Shaijumon, S. R. Gowda and P. M. Ajayan, *Nano Lett.*, 2009, **9**, 1002-1006.
326. G. Wang, X. Shen, J. Yao and J. Park, *Carbon*, 2009, **47**, 2049-2053.
327. J.-S. Lee, S. Tai Kim, R. Cao, N.-S. Choi, M. Liu, K. T. Lee and J. Cho, *Adv. Energy Mater.*, 2011, **1**, 34-50.
328. V. Neburchilov, H. Wang, J. J. Martin and W. Qu, *J. Power Sources*, 2010, **195**, 1271-1291.

329. Z.-L. Wang, D. Xu, J.-J. Xu and X.-B. Zhang, *Chem. Soc. Rev.*, 2014, **43**, 7746-7786.
330. M. Endo, C. Kim, K. Nishimura, T. Fujino and K. Miyashita, *Carbon*, 2000, **38**, 183-197.
331. S. Sharma and B. G. Pollet, *J. Power Sources*, 2012, **208**, 96-119.
332. E. Frackowiak and F. Béguin, *Carbon*, 2001, **39**, 937-950.
333. J.-G. Zhang, D. Wang, W. Xu, J. Xiao and R. E. Williford, *J. Power Sources*, 2010, **195**, 4332-4337.
334. Y. Gao, C. Wang, W. Pu, Z. Liu, C. Deng, P. Zhang and Z. Mao, *Int. J. Hydrogen Energ.*, 2012, **37**, 12725-12730.
335. D. Wang, J. Xiao, W. Xu and J.-G. Zhang, *J. Electrochem. Soc.*, 2010, **157**, A760-A764.
336. J. Xiao, D. Wang, W. Xu, D. Wang, R. E. Williford, J. Liu and J.-G. Zhang, *J. Electrochem. Soc.*, 2010, **157**, A487-A492.
337. J. Xiao, W. Xu, D. Wang and J.-G. Zhang, *J. Electrochem. Soc.*, 2010, **157**, A294-A297.
338. B. Sun, H. Liu, P. Munroe, H. Ahn and G. Wang, *Nano Res.*, 2012, **5**, 460-469.
339. B. Sun, B. Wang, D. Su, L. Xiao, H. Ahn and G. Wang, *Carbon*, 2012, **50**, 727-733.
340. O. Crowther, B. Meyer, M. Morgan and M. Salomon, *J. Power Sources*, 2011, **196**, 1498-1502.
341. D. Zhang, R. Li, T. Huang and A. Yu, *J. Power Sources*, 2010, **195**, 1202-1206.
342. J. Zhang, W. Xu and W. Liu, *J. Power Sources*, 2010, **195**, 7438-7444.
343. J. Zhang, W. Xu, X. Li and W. Liu, *J. Electrochem. Soc.*, 2010, **157**, A940-A946.
344. W. Xu, J. Xiao, J. Zhang, D. Wang and J.-G. Zhang, *J. Electrochem. Soc.*, 2009, **156**, A773-A779.
345. D. Zhang, Z. Fu, Z. Wei, T. Huang and A. Yu, *J. Electrochem. Soc.*, 2010, **157**, A362-A365.
346. G. Zhao, L. Zhang, T. Pan and K. Sun, *J. Solid. State. Electr.*, 2013, **17**, 1759-1764.
347. Y. Lei, J. Lu, X. Luo, T. Wu, P. Du, X. Zhang, Y. Ren, J. Wen, D. J. Miller, J. T. Miller, Y.-K. Sun, J. W. Elam and K. Amine, *Nano Lett.*, 2013, **13**, 4182-4189.
348. V. Viswanathan, J. K. Nørskov, A. Speidel, R. Scheffler, S. Gowda and A. C. Luntz, *J. Phys. Chem. Lett.*, 2013, **4**, 556-560.
349. G. Wu, N. H. Mack, W. Gao, S. Ma, R. Zhong, J. Han, J. K. Baldwin and P. Zelenay, *ACS Nano*, 2012, **6**, 9764-9776.
350. Y. Li, J. Wang, X. Li, D. Geng, R. Li and X. Sun, *Chem. Commun.*, 2011, **47**, 9438-9440.
351. S. Meini, M. Piana, H. Beyer, J. Schwämmlein and H. A. Gasteiger, *J. Electrochem. Soc.*, 2012, **159**, A2135-A2142.
352. F.-S. Ke, B. C. Solomon, S.-G. Ma and X.-D. Zhou, *Electrochim. Acta*, 2012, **85**, 444-449.
353. Y. Yang, M. Shi, Q.-F. Zhou, Y.-S. Li and Z.-W. Fu, *Electrochem. Commun.*, 2012, **20**, 11-14.
354. J. Li, B. Peng, G. Zhou, Z. Zhang, Y. Lai and M. Jia, *ECS Electrochem. Lett.*, 2013, **2**, A25-A27.
355. T. Zhang and H. Zhou, *Angew. Chem. Int. Edit.*, 2012, **124**, 11224-11229.
356. R. E. Fuentès, H. R. Colón-Mercado and E. B. Fox, *J. Power Sources*, 2014, **255**, 219-222.
357. A. K. Geim and K. S. Novoselov, *Nat. Mater.*, 2007, **6**, 183-191.
358. M. D. Stoller, S. Park, Y. Zhu, J. An and R. S. Ruoff, *Nano Lett.*, 2008, **8**, 3498-3502.
359. A. K. Geim, *Science*, 2009, **324**, 1530-1534.
360. K. S. Novoselov, A. K. Geim, S. V. Morozov, D. Jiang, M. I. Katsnelson, I. V. Grigorieva, S. V. Dubonos and A. A. Firsov, *Nature*, 2005, **438**, 197-200.
361. S. Liu, J. Wang, J. Zeng, J. Ou, Z. Li, X. Liu and S. Yang, *J. Power Sources*, 2010, **195**, 4628-4633.
362. N. Soin, S. S. Roy, T. H. Lim and J. A. D. McLaughlin, *Mater. Chem. Phys.*, 2011, **129**, 1051-1057.
363. Y.-G. Zhou, J.-J. Chen, F.-B. Wang, Z.-H. Sheng and X.-H. Xia, *Chem. Commun.*, 2010, **46**, 5951-5953.
364. B. Seger and P. V. Kamat, *J. Phys. Chem. C*, 2009, **113**, 7990-7995.
365. E. Yoo, J. Kim, E. Hosono, H.-s. Zhou, T. Kudo and I. Honma, *Nano Lett.*, 2008, **8**, 2277-2282.
366. X. Huang, X. Qi, F. Boey and H. Zhang, *Chem. Soc. Rev.*, 2012, **41**, 666-686.
367. Y. Li, J. Wang, X. Li, J. Liu, D. Geng, J. Yang, R. Li and X. Sun, *Electrochem. Commun.*, 2011, **13**, 668-672.
368. H.-G. Jung, Y. S. Jeong, J.-B. Park, Y.-K. Sun, B. Scrosati and Y. J. Lee, *ACS Nano*, 2013, **7**, 3532-3539.
369. H. Kim, H.-D. Lim, J. Kim and K. Kang, *J. Mater. Chem. A*, 2014, **2**, 33-47.
370. L. Wang, M. Ara, K. Wadumesthrige, S. Salley and K. Y. S. Ng, *J. Power Sources*, 2013, **234**, 8-15.
371. S. Liu, Y. Zhu, J. Xie, Y. Huo, H. Y. Yang, T. Zhu, G. Cao, X. Zhao and S. Zhang, *Adv. Energy Mater.*, 2014, **4**, 1301960.
372. J. Lee, J. Kim and T. Hyeon, *Adv. Mater.*, 2006, **18**, 2073-2094.
373. J. Lee, S. Yoon, T. Hyeon, S. M. Oh and K. Bum Kim, *Chem. Commun.*, 1999, **0**, 2177-2178.
374. T. Maschmeyer, F. Rey, G. Sankar and J. M. Thomas, *Nature*, 1995, **378**, 159-162.
375. A. B. Fuentès and D. M. Nevskaya, *J. Mater. Chem.*, 2003, **13**, 1843-1846.

376. Z. Guo, D. Zhou, X. Dong, Z. Qiu, Y. Wang and Y. Xia, *Adv. Mater.*, 2013, **25**, 5668-5672.
377. S. Iijima and T. Ichihashi, *Nature*, 1993, **363**, 603-605.
378. S. Iijima, *Nature*, 1991, **354**, 56-58.
379. T. Yoon and Y. Park, *Nanoscale Res. Lett.*, 2012, **7**, 1-4.
380. Y. Shen, D. Sun, L. Yu, W. Zhang, Y. Shang, H. Tang, J. Wu, A. Cao and Y. Huang, *Carbon*, 2013, **62**, 288-295.
381. R. Mi, H. Liu, H. Wang, K.-W. Wong, J. Mei, Y. Chen, W.-M. Lau and H. Yan, *Carbon*, 2014, **67**, 744-752.
382. H. Wang, K. Xie, L. Wang and Y. Han, *RSC Adv.*, 2013, **3**, 8236-8241.
383. H.-D. Lim, K.-Y. Park, H. Song, E. Y. Jang, H. Gwon, J. Kim, Y. H. Kim, M. D. Lima, R. O. Robles, X. Lepró, R. H. Baughman and K. Kang, *Adv. Mater.*, 2013, **25**, 1348-1352.
384. S. Nakanishi, F. Mizuno, K. Nobuhara, T. Abe and H. Iba, *Carbon*, 2012, **50**, 4794-4803.
385. Y. Chen, F. Li, D.-M. Tang, Z. Jian, C. Liu, D. Golberg, A. Yamada and H. Zhou, *J. Mater. Chem. A*, 2013, **1**, 13076-13081.
386. C. S. Park, K. S. Kim and Y. J. Park, *J. Power Sources*, 2013, **244**, 72-79.
387. J. Kang, O. L. Li and N. Saito, *J. Power Sources*, 2014, **261**, 156-161.
388. F. Soavi, S. Monaco and M. Mastragostino, *J. Power Sources*, 2013, **224**, 115-119.
389. Y. Yang, Q. Sun, Y.-S. Li, H. Li and Z.-W. Fu, *J. Electrochem. Soc.*, 2011, **158**, B1211-B1216.
390. D. Geng, H. Liu, Y. Chen, R. Li, X. Sun, S. Ye and S. Knights, *J. Power Sources*, 2011, **196**, 1795-1801.
391. Y. Chen, J. Wang, H. Liu, M. N. Banis, R. Li, X. Sun, T.-K. Sham, S. Ye and S. Knights, *J. Phys. Chem. C*, 2011, **115**, 3769-3776.
392. H. Liu, Y. Zhang, R. Li, X. Sun, S. Désilets, H. Abou-Rachid, M. Jaidann and L.-S. Lussier, *Carbon*, 2010, **48**, 1498-1507.
393. L. Qu, Y. Liu, J.-B. Baek and L. Dai, *ACS Nano*, 2010, **4**, 1321-1326.
394. Y. Shao, S. Zhang, M. H. Engelhard, G. Li, G. Shao, Y. Wang, J. Liu, I. A. Aksay and Y. Lin, *J. Mater. Chem.*, 2010, **20**, 7491-7496.
395. K. R. Lee, K. U. Lee, J. W. Lee, B. T. Ahn and S. I. Woo, *Electrochem. Commun.*, 2010, **12**, 1052-1055.
396. D. Geng, Y. Chen, Y. Chen, Y. Li, R. Li, X. Sun, S. Ye and S. Knights, *Energy Environ. Sci.*, 2011, **4**, 760-764.
397. D. Higgins, Z. Chen, D. U. Lee and Z. Chen, *J. Mater. Chem. A*, 2013, **1**, 2639-2645.
398. M. Inagaki, H. Konno and O. Tanaike, *J. Power Sources*, 2010, **195**, 7880-7903.
399. R. Bashyam and P. Zelenay, *Nature*, 2006, **443**, 63-66.
400. R. Jasinski, *J. Electrochem. Soc.*, 1965, **112**, 526-528.
401. Y. Wang, Y. Shao, D. W. Matson, J. Li and Y. Lin, *ACS Nano*, 2010, **4**, 1790-1798.
402. H. Wang, T. Maiyalagan and X. Wang, *ACS Catal.*, 2012, **2**, 781-794.
403. D. Usachov, O. Vilkov, A. Grüneis, D. Haberer, A. Fedorov, V. K. Adamchuk, A. B. Preobrajenski, P. Dudin, A. Barinov, M. Oehzelt, C. Laubschat and D. V. Vyalikh, *Nano Lett.*, 2011, **11**, 5401-5407.
404. G. Imamura and K. Saiki, *J. Phys. Chem. C*, 2011, **115**, 10000-10005.
405. Z. Sun, Z. Yan, J. Yao, E. Beitler, Y. Zhu and J. M. Tour, *Nature*, 2010, **468**, 549-552.
406. B. Guo, Q. Liu, E. Chen, H. Zhu, L. Fang and J. R. Gong, *Nano Lett.*, 2010, **10**, 4975-4980.
407. C. Zhang, L. Fu, N. Liu, M. Liu, Y. Wang and Z. Liu, *Adv. Mater.*, 2011, **23**, 1020-1024.
408. H. Wang, Q. Wang, Y. Cheng, K. Li, Y. Yao, Q. Zhang, C. Dong, P. Wang, U. Schwingenschlögl, W. Yang and X. X. Zhang, *Nano Lett.*, 2012, **12**, 141-144.
409. Y. Lu, Z. Wen, J. Jin, Y. Cui, M. Wu and S. Sun, *J. Solid. State. Electr.*, 2012, **16**, 1863-1868.
410. H. Wang, X.-Z. Liao, L. Li, H. Chen, Q.-Z. Jiang, Y.-S. He and Z.-F. Ma, *J. Electrochem. Soc.*, 2012, **159**, A1874-A1879.
411. P. Kichambare and S. Rodrigues, *Energy Technology*, 2013, **1**, 209-211.
412. E. Yoo and H. Zhou, *RSC Adv.*, 2014, **4**, 13119-13122.
413. S. Dong, X. Chen, K. Zhang, L. Gu, L. Zhang, X. Zhou, L. Li, Z. Liu, P. Han, H. Xu, J. Yao, C. Zhang, X. Zhang, C. Shang, G. Cui and L. Chen, *Chem. Commun.*, 2011, **47**, 11291-11293.
414. H. Yan, B. Xu, S. Shi and C. Ouyang, *J. Appl. Phys.*, 2012, **112**, 104316.
415. X. Lin, X. Lu, T. Huang, Z. Liu and A. Yu, *J. Power Sources*, 2013, **242**, 855-859.
416. J. Shui, F. Du, C. Xue, Q. Li and L. Dai, *ACS Nano*, 2014, **8**, 3015-3022.
417. H. Nie, H. Zhang, Y. Zhang, T. Liu, J. Li and Q. Lai, *Nanoscale*, 2013, **5**, 8484-8487.
418. J. Yin, B. Fang, J. Luo, B. Wanjala, D. Mott, R. Loukrakpam, M. S. Ng, Z. Li, J. Hong, M. S. Whittingham and C.-J. Zhong, *Nanotechnology*, 2012, **23**, 305404.

419. B. K. Ko, M. K. Kim, S. H. Kim, M. A. Lee, S. E. Shim and S.-H. Baeck, *J. Mol. Catal. A-Chem.*, 2013, **379**, 9-14.
420. J. Zhang, G. Chen, M. An and P. Wang, *Int. J. Electrochem. Sci.*, 2012, **7**, 11957-11965.
421. B. G. Kim, H.-J. Kim, S. Back, K. W. Nam, Y. Jung, Y.-K. Han and J. W. Choi, *Sci. Rep.*, 2014, **4**, 4225.
422. D. Su, H.-S. Kim, W.-S. Kim and G. Wang, *J. Power Sources*, 2013, **244**, 488-493.
423. B. Sun, P. Munroe and G. Wang, *Sci. Rep.*, 2013, **3**, 2247.
424. J.-K. S. Ku-Bong Chung, Tae-Young Jang, Dong-Kyun Noh, Yongsug Tak, Sung-Hyeon Baeck, *Rev. Adv. Mater. Sci.*, 2011, **28**, 54-58.
425. L. Trahey, N. K. Karan, M. K. Y. Chan, J. Lu, Y. Ren, J. Greeley, M. Balasubramanian, A. K. Burrell, L. A. Curtiss and M. M. Thackeray, *Adv. Energy Mater.*, 2013, **3**, 75-84.
426. Y. Yang, M. Shi, Y.-S. Li and Z.-W. Fu, *J. Electrochem. Soc.*, 2012, **159**, A1917-A1921.
427. K.-N. Jung, A. Riaz, S.-B. Lee, T.-H. Lim, S.-J. Park, R.-H. Song, S. Yoon, K.-H. Shin and J.-W. Lee, *J. Power Sources*, 2013, **244**, 328-335.
428. O. Oloniyo, S. Kumar and K. Scott, *J. Electron. Mater.*, 2012, **41**, 921-927.
429. K. Song, J. Jung, Y.-U. Heo, Y. C. Lee, K. Cho and Y.-M. Kang, *Phys. Chem. Chem. Phys.*, 2013, **15**, 20075-20079.
430. T. T. Truong, Y. Liu, Y. Ren, L. Trahey and Y. Sun, *ACS Nano*, 2012, **6**, 8067-8077.
431. J. Zeng, J. R. Nair, C. Francia, S. Bodoardo and N. Penazzi, *Int. J. Electrochem. Sci.*, 2013, **8**, 3912-3927.
432. A. K. Thapa, B. B. Pandit, H. S. Paudel, R. Thapa, S. Ida, J. B. Jasinski, G. U. Sumanasekera and T. Ishihara, *Electrochim. Acta*, 2014, **127**, 410-415.
433. A. Zahoor, H. S. Jang, J. S. Jeong, M. Christy, Y. J. Hwang and K. S. Nahm, *RSC Adv.*, 2014, **4**, 8973-8977.
434. X. Hu, X. Han, Y. Hu, F. Cheng and J. Chen, *Nanoscale*, 2014, **6**, 3522-3525.
435. M. Zhang, Q. Xu, L. Sang, F. Ding, X.-j. Liu and L.-f. Jiao, *T. Nonferr. Metal Soc.*, 2014, **24**, 164-170.
436. D. Oh, J. Qi, Y.-C. Lu, Y. Zhang, Y. Shao-Horn and A. M. Belcher, *Nat. Commun.*, 2013, **4**, 2576.
437. L. Zhang, Z. Wang, D. Xu, J. Xu, X. Zhang and L. Wang, *Chinese. Sci. Bull.*, 2012, **57**, 4210-4214.
438. A. K. Thapa, Y. Hidaka, H. Hagiwara, S. Ida and T. Ishihara, *J. Electrochem. Soc.*, 2011, **158**, A1483-A1489.
439. C. Kavakli, S. Meini, G. Harzer, N. Tsiouvaras, M. Piana, A. Siebel, A. Garsuch, H. A. Gasteiger and J. Herranz, *ChemCatChem*, 2013, **5**, 3358-3373.
440. H. Minowa, M. Hayashi, K. Hayashi, R. Kobayashi and K. Takahashi, *J. Power Sources*, 2013, **244**, 17-22.
441. L. Zhang, X. Zhang, Z. Wang, J. Xu, D. Xu and L. Wang, *Chem. Commun.*, 2012, **48**, 7598-7600.
442. J. Zhang, *PEM fuel cell electrocatalysts and catalyst layers: fundamentals and applications*, Springer, 2008.
443. R. Cao, J.-S. Lee, M. Liu and J. Cho, *Adv. Energy Mater.*, 2012, **2**, 816-829.
444. S. H. Lim, D. H. Kim, J. Y. Byun, B. K. Kim and W. Y. Yoon, *Electrochim. Acta*, 2013, **107**, 681-685.
445. K. Kim and Y. Park, *Nanoscale Res. Lett.*, 2012, **7**, 1-6.
446. A. Riaz, K.-N. Jung, W. Chang, S.-B. Lee, T.-H. Lim, S.-J. Park, R.-H. Song, S. Yoon, K.-H. Shin and J.-W. Lee, *Chem. Commun.*, 2013, **49**, 5984-5986.
447. J. Ming, F. Zhao, Y. Wu, J.-B. Park, Y.-K. Sun and J.-K. Lee, *Nanoscale*, 2013, **5**, 10390-10396.
448. G. Zhao, Z. Xu and K. Sun, *J. Mater. Chem. A*, 2013, **1**, 12862-12867.
449. V. Anandan, R. Kudla, A. Drews, J. Adams and M. Karulkar, *ECS Trans.*, 2012, **41**, 167-174.
450. Y. Li, L. Zou, J. Li, K. Guo, X. Dong, X. Li, X. Xue, H. Zhang and H. Yang, *Electrochim. Acta*, 2014, **129**, 14-20.
451. J. Jung, K. Song, D. R. Bae, S. W. Lee, G. Lee and Y.-M. Kang, *Nanoscale*, 2013, **5**, 11845-11849.
452. D. B. Y. M. Chiang, W. D. Kingery, ed., *Physical Ceramics: Principles for Ceramic Science and Engineering*, John Wiley & Sons, 1997.
453. A. Chroneos, R. V. Vovk, I. L. Goulatis and L. I. Goulatis, *J. Alloy. Compd.*, 2010, **494**, 190-195.
454. F. Tietz, H.-P. Buchkremer and D. Stöver, *J. Electroceram.*, 2006, **17**, 701-707.
455. S. Jiang, *J. Mater. Sci.*, 2008, **43**, 6799-6833.
456. S. P. Jiang, *Int. J. Hydrogen Energ.*, 2012, **37**, 449-470.
457. A. J. Jacobson, *Chem. Mater.*, 2009, **22**, 660-674.
458. R. V. Vovk, M. A. Obolenskii, A. A. Zavgorodniy, A. V. Bondarenko, I. L. Goulatis, A. V. Samoilov and A. Chroneos, *J. Alloy. Compd.*, 2008, **453**, 69-74.
459. K. Larbaoui, A. Tadjer, B. Abbar, H. Aourag, B. Khelifa and C. Mathieu, *J. Alloy. Compd.*, 2005, **403**,

- 1-14.
460. J. W. Fergus, *Sensor Actuat. B-Chem.*, 2007, **123**, 1169-1179.
461. Z. Shao and S. M. Haile, *Nature*, 2004, **431**, 170-173.
462. C. Jin, X. Cao, L. Zhang, C. Zhang and R. Yang, *J. Power Sources*, 2013, **241**, 225-230.
463. X. Wang, P. J. Sebastian, M. A. Smit, H. Yang and S. A. Gamboa, *J. Power Sources*, 2003, **124**, 278-284.
464. S. K. Tiwari, S. P. Singh and R. N. Singh, *J. Electrochem. Soc.*, 1996, **143**, 1505-1510.
465. L. Zhang, J. Zhang, D. P. Wilkinson and H. Wang, *J. Power Sources*, 2006, **156**, 171-182.
466. X. Li, W. Qu, J. Zhang and H. Wang, *J. Electrochem. Soc.*, 2011, **158**, A597-A604.
467. D. B. Meadowcroft, *Nature*, 1970, **226**, 847-848.
468. X. Li, W. Qu, J. Zhang and H. Wang, *ECS Trans.*, 2010, **28**, 45-56.
469. H. Ohkuma, I. Uechi, N. Imanishi, A. Hirano, Y. Takeda and O. Yamamoto, *J. Power Sources*, 2013, **223**, 319-324.
470. W. Yang, J. Salim, S. Li, C. Sun, L. Chen, J. B. Goodenough and Y. Kim, *J. Mater. Chem.*, 2012, **22**, 18902-18907.
471. K.-N. Jung, J.-I. Lee, W. B. Im, S. Yoon, K.-H. Shin and J.-W. Lee, *Chem. Commun.*, 2012, **48**, 9406-9408.
472. Z. Fu, X. Lin, T. Huang and A. Yu, *J. Solid. State. Electr.*, 2012, **16**, 1447-1452.
473. Y. Zhao, L. Xu, L. Mai, C. Han, Q. An, X. Xu, X. Liu and Q. Zhang, *P. Natl. Acad. Sci. USA*, 2012, **109**, 19569-19574.
474. J. Suntivich, K. J. May, H. A. Gasteiger, J. B. Goodenough and Y. Shao-Horn, *Science*, 2011, **334**, 1383-1385.
475. N. Lopez, D. J. Graham, R. McGuire, G. E. Alliger, Y. Shao-Horn, C. C. Cummins and D. G. Nocera, *Science*, 2012, **335**, 450-453.
476. R. S. Kalubarme, G.-E. Park, K.-N. Jung, K.-H. Shin, W.-H. Ryu and C.-J. Park, *J. Electrochem. Soc.*, 2014, **161**, A880-A889.
477. M. Yuasa, T. Matsuyoshi, T. Kida and K. Shimano, *J. Power Sources*, 2013, **242**, 216-221.
478. T. Meng, M. Ara, L. Wang, R. Naik and K. Y. S. Ng, *J. Mater. Sci.*, 2014, **49**, 4058-4066.
479. C. Jin, Z. Yang, X. Cao, F. Lu and R. Yang, *Int. J. Hydrogen Energ.*, 2014, **39**, 2526-2530.
480. X. Han, Y. Hu, J. Yang, F. Cheng and J. Chen, *Chem. Commun.*, 2014, **50**, 1497-1499.
481. T. K. Mandal and J. Gopalakrishnan, *Chem. Mater.*, 2005, **17**, 2310-2316.
482. B. Aurivillius, *Ark. Kemi*, 1949, **1**, 499.
483. R. E. Schaak and T. E. Mallouk, *Chem. Mater.*, 2002, **14**, 1455-1471.
484. S. N. Ruddlesden and P. Popper, *Acta Crystallographica*, 1958, **11**, 54-55.
485. B. Aurivillius, *Ark. Kemi*, 1949, **1**, 463.
486. S. N. Ruddlesden and P. Popper, *Acta Crystallogr.*, 1957, **10**, 538.
487. M. Dion, M. Ganne and M. Tournoux, *Mater. Res. Bull.*, 1981, **16**, 1429.
488. M. Dion, M. Ganne, M. Tournoux and J. Revez, *Rev. Chim. Miner.*, 1984, **21**, 92.
489. Z. Ma, X. Yuan, L. Li and Z.-F. Ma, *Chem. Commun.*, 2014, **50**, 14855-14858.
490. R. S. Kalubarme, M.-S. Cho, J.-K. Kim and C.-J. Park, *Nanotechnology*, 2012, **23**, 435703.
491. H. Wang, Y. Yang, Y. Liang, G. Zheng, Y. Li, Y. Cui and H. Dai, *Energy Environ. Sci.*, 2012, **5**, 7931-7935.
492. L. Wang, X. Zhao, Y. Lu, M. Xu, D. Zhang, R. S. Ruoff, K. J. Stevenson and J. B. Goodenough, *J. Electrochem. Soc.*, 2011, **158**, A1379-A1382.
493. Y. Cao, Z. Wei, J. He, J. Zang, Q. Zhang, M. Zheng and Q. Dong, *Energy Environ. Sci.*, 2012, **5**, 9765-9768.
494. R. S. Kalubarme, C.-H. Ahn and C.-J. Park, *Scripta Mater.*, 2013, **68**, 619-622.
495. W.-H. Ryu, T.-H. Yoon, S. H. Song, S. Jeon, Y.-J. Park and I.-D. Kim, *Nano Lett.*, 2013, **13**, 4190-4197.
496. W. Zhang, Y. Zeng, C. Xu, H. Tan, W. Liu, J. Zhu, N. Xiao, H. H. Hng, J. Ma, H. E. Hoster, R. Yazami and Q. Yan, *RSC Adv.*, 2012, **2**, 8508-8514.
497. C.-H. Ahn, R. S. Kalubarme, Y.-H. Kim, K.-N. Jung, K.-H. Shin and C.-J. Park, *Electrochim. Acta*, 2014, **117**, 18-25.
498. C. Selvaraj, S. Kumar, N. Munichandraiah and L. G. Scanlon, *J. Electrochem. Soc.*, 2014, **161**, A554-A560.
499. C. H. San and C. W. Hong, *J. Electrochem. Soc.*, 2012, **159**, K116-K121.
500. F. Li, Y. Chen, D.-M. Tang, L. Z. Jian, C. Liu, D. Golberg, A. Yamada and H. Zhou, *Energy Environ. Sci.*, 2014, **7**, 1648-1652.

501. E. Yilmaz, C. Yogi, K. Yamanaka, T. Ohta and H. R. Byon, *Nano Lett.*, 2013, **13**, 4679-4684.
502. Z. Jian, P. Liu, F. Li, P. He, X. Guo, M. Chen and H. Zhou, *Angew. Chem. Int. Edit.*, 2014, **53**, 442-446.
503. H. R. Eom, M. K. Kim, M. S. Kim, G.-P. Kim and S.-H. Baeck, *J. Nanosci Nanotechnol.*, 2013, **13**, 1780-1783.
504. B.-W. Huang, X.-Z. Liao, H. Wang, C.-N. Wang, Y.-S. He and Z.-F. Ma, *J. Electrochem. Soc.*, 2013, **160**, A1112-A1117.
505. C. Park, J. Kim and Y. Park, *J. Electroceram.*, 2013, **31**, 224-230.
506. J. Lu, Y. Qin, P. Du, X. Luo, T. Wu, Y. Ren, J. Wen, D. J. Miller, J. T. Miller and K. Amine, *RSC Adv.*, 2013, **3**, 8276-8285.
507. J. Wu, H. W. Park, A. Yu, D. Higgins and Z. Chen, *J. Phys. Chem. C*, 2012, **116**, 9427-9432.
508. A. K. Thapa and T. Ishihara, *J. Power Sources*, 2011, **196**, 7016-7020.
509. W. Yang, J. Salim, C. Ma, Z. Ma, C. Sun, J. Li, L. Chen and Y. Kim, *Electrochem. Commun.*, 2013, **28**, 13-16.
510. J. Gomez, E. E. Kalu, R. Nelson, M. H. Weatherspoon and J. P. Zheng, *J. Mater. Chem. A*, 2013, **1**, 3287-3294.
511. K. Guo, Y. Li, J. Yang, Z. Zou, X. Xue, X. Li and H. Yang, *J. Mater. Chem. A*, 2014, **2**, 1509-1514.
512. T. Ishihara, A. K. Thapa, Y. Hidaka and S. Ida, *Electrochemistry*, 2012, **80**, 731-733.
513. R. Choi, J. Jung, G. Kim, K. Song, Y.-I. Kim, S. C. Jung, Y.-K. Han, H. Song and Y.-M. Kang, *Energy Environ. Sci.*, 2014, **7**, 1362-1368.
514. K. Liao, T. Zhang, Y. Wang, F. Li, Z. Jian, H. Yu and H. Zhou, *ChemSusChem*, 2015, **8**, 1429-1434.
515. M. Wu, J. Suk, J. Y. Jo, Y. Kim, S. Choi, D. W. Kim, Y. Kang and H.-K. Jung, *ECS Electrochem. Lett.*, 2015, **4**, A59-A61.
516. X. Lin, Y. Shang, L. Li and A. Yu, *ACS Sustainable Chemistry & Engineering*, 2015, **3**, 903-908.
517. J. Cao, S. Liu, J. Xie, S. Zhang, G. Cao and X. Zhao, *ACS Catal.*, 2015, **5**, 241-245.
518. F. Li, D.-M. Tang, Y. Chen, D. Golberg, H. Kitaura, T. Zhang, A. Yamada and H. Zhou, *Nano Lett.*, 2013, **13**, 4702-4707.
519. G. Zhao, J. Lv, Z. Xu, L. Zhang and K. Sun, *J. Power Sources*, 2014, **248**, 1270-1274.
520. X. Yuan, X. Zeng, H.-J. Zhang, Z.-F. Ma and C.-Y. Wang, *J. Am. Chem. Soc.*, 2010, **132**, 1754-1755.
521. G. Wu, K. L. More, C. M. Johnston and P. Zelenay, *Science*, 2011, **332**, 443-447.
522. J.-L. Shui, N. K. Karan, M. Balasubramanian, S.-Y. Li and D.-J. Liu, *J. Am. Chem. Soc.*, 2012, **134**, 16654-16661.
523. L. Yu, Y. Shen and Y. Huang, *J. Alloy. Compd.*, 2014, **595**, 185-191.
524. Q. Li, P. Xu, W. Gao, S. Ma, G. Zhang, R. Cao, J. Cho, H.-L. Wang and G. Wu, *Adv. Mater.*, 2014, **26**, 1378-1386.
525. H. Wang, X. Liao, Q. Jiang, X. Yang, Y. He and Z. Ma, *Chinese. Sci. Bull.*, 2012, **57**, 1959-1963.
526. Z. Zhang, L. Su, M. Yang, M. Hu, J. Bao, J. Wei and Z. Zhou, *Chem. Commun.*, 2014, **50**, 776-778.
527. H. W. Park, D. U. Lee, L. F. Nazar and Z. Chen, *J. Electrochem. Soc.*, 2012, **160**, A344-A350.
528. Y. Li, J. Wang, X. Li, D. Geng, M. N. Banis, Y. Tang, D. Wang, R. Li, T.-K. Sham and X. Sun, *J. Mater. Chem.*, 2012, **22**, 20170-20174.
529. Y. Tian, H. Yue, Z. Gong and Y. Yang, *Electrochim. Acta*, 2013, **90**, 186-193.
530. S. Dong, X. Chen, S. Wang, L. Gu, L. Zhang, X. Wang, X. Zhou, Z. Liu, P. Han, Y. Duan, H. Xu, J. Yao, C. Zhang, K. Zhang, G. Cui and L. Chen, *ChemSusChem*, 2012, **5**, 1712-1715.
531. M. A. Careem, Y. Velmurugu, S. Skaarup and K. West, *J. Power Sources*, 2006, **159**, 210-214.
532. V. G. Khomenko, V. Z. Barsukov and A. S. Katashinskii, *Electrochim. Acta*, 2005, **50**, 1675-1683.
533. N. Alonso-Vante, S. Cattarin and M. Musiani, *J. Electroanal. Chem.*, 2000, **481**, 200-207.
534. X. Yuan, X.-L. Ding, C.-Y. Wang and Z.-F. Ma, *Energy Environ. Sci.*, 2013, **6**, 1105-1124.
535. E. K. W. Lai, P. D. Beattie and S. Holdcroft, *Synthetic. Met.*, 1997, **84**, 87-88.
536. K. Gurunathan, A. V. Murugan, R. Marimuthu, U. P. Mulik and D. P. Amalnerkar, *Mater. Chem. Phys.*, 1999, **61**, 173-191.
537. J. W. Schultze and H. Karabulut, *Electrochim. Acta*, 2005, **50**, 1739-1745.
538. J. Zhang, B. Sun, H.-J. Ahn, C. Wang and G. Wang, *Mater. Res. Bull.*, 2013, **48**, 4979-4983.
539. E. Nasybulin, W. Xu, M. H. Engelhard, X. S. Li, M. Gu, D. Hu and J.-G. Zhang, *Electrochem. Commun.*, 2013, **29**, 63-66.
540. Q. Lu, Q. Zhao, H. Zhang, J. Li, X. Wang and F. Wang, *ACS Macro Lett.*, 2013, **2**, 92-95.
541. Y. Cui, Z. Wen, Y. Lu, M. Wu, X. Liang and J. Jin, *J. Power Sources*, 2013, **244**, 614-619.
542. D. Zheng, H.-S. Lee, X.-Q. Yang and D. Qu, *Electrochem. Commun.*, 2013, **28**, 17-19.
543. T. H. Yoon and Y. J. Park, *RSC Adv.*, 2014, **4**, 17434-17442.
544. W.-J. Kwak, D. Hirshberg, D. Sharon, H.-J. Shin, M. Afri, J.-B. Park, A. Garsuch, F. F. Chesneau, A.

- A. Frimer, D. Aurbach and Y.-K. Sun, *J. Mater. Chem. A*, 2015, **3**, 8855-8864.
545. M. J. Lacey, J. T. Frith and J. R. Owen, *Electrochem. Commun.*, 2013, **26**, 74-76.
546. M. D. Hager, P. Greil, C. Leyens, S. van der Zwaag and U. S. Schubert, *Adv. Mater.*, 2010, **22**, 5424-5430.
547. N. Holten-Andersen, M. J. Harrington, H. Birkedal, B. P. Lee, P. B. Messersmith, K. Y. C. Lee and J. H. Waite, *Proceedings of the National Academy of Sciences*, 2011, **108**, 2651-2655.
548. D. Wu, Z. Guo, X. Yin, Q. Pang, B. Tu, L. Zhang, Y.-G. Wang and Q. Li, *Adv. Mater.*, 2014, **26**, 3258-3262.
549. W. Weng, C. J. Barile, P. Du, A. Abouimrane, R. S. Assary, A. A. Gewirth, L. A. Curtiss and K. Amine, *Electrochim. Acta*, 2014, **119**, 138-143.
550. L. Xu, J. Ma, B. Li and F. Kang, *J. Power Sources*, 2014, **255**, 187-196.
551. N. Garcia-Araez and P. Novák, *J. Solid. State. Electr.*, 2013, **17**, 1793-1807.
552. C. Tran, X.-Q. Yang and D. Qu, *J. Power Sources*, 2010, **195**, 2057-2063.
553. S.-W. Eom, C.-W. Lee, M.-S. Yun and Y.-K. Sun, *Electrochim. Acta*, 2006, **52**, 1592-1595.
554. C. H. Hamann, A. Hamnett and W. Vielstich, *Electrochemistry*, Wiley, 1998.
555. S. R. Younesi, S. Urbonaite, F. Björefors and K. Edström, *J. Power Sources*, 2011, **196**, 9835-9838.
556. S. B. Ma, D. J. Lee, V. Roev, D. Im and S.-G. Doo, *J. Power Sources*, 2013, **244**, 494-498.
557. G. O. Shitta-Bey, M. Mirzaeian and P. J. Hall, *J. Electrochem. Soc.*, 2012, **159**, A315-A320.
558. R. Younesi, N. Singh, S. Urbonaite and K. Edstrom, *ECS Trans.*, 2010, **25**, 121-127.
559. M. Balaish, A. Kraysberg and Y. Ein-Eli, *ChemElectroChem*, 2014, **1**, 90-94.
560. C. Xia, C. L. Bender, B. Bergner, K. Pepller and J. Janek, *Electrochem. Commun.*, 2013, **26**, 93-96.
561. H.-D. Lim, H. Song, H. Gwon, K.-Y. Park, J. Kim, Y. Bae, H. Kim, S.-K. Jung, T. Kim, Y. H. Kim, X. Lepro, R. Ovalle-Robles, R. H. Baughman and K. Kang, *Energy Environ. Sci.*, 2013, **6**, 3570-3575.
562. S. Liu, Z. Wang, C. Yu, Z. Zhao, X. Fan, Z. Ling and J. Qiu, *J. Mater. Chem. A*, 2013, **1**, 12033-12037.
563. H. Cheng and K. Scott, *J. Power Sources*, 2013, **235**, 226-233.
564. J. Li, N. Wang, Y. Zhao, Y. Ding and L. Guan, *Electrochem. Commun.*, 2011, **13**, 698-700.
565. X. Liu, D. Wang and S. Shi, *Electrochim. Acta*, 2013, **87**, 865-871.
566. G. M. Veith and N. J. Dudney, *J. Electrochem. Soc.*, 2011, **158**, A658-A663.
567. T. H. Yoon and Y. J. Park, *J. Power Sources*, 2013, **244**, 344-353.
568. R. Nelson, M. H. Weatherspoon, J. Gomez, E. E. Kalu and J. P. Zheng, *Electrochem. Commun.*, 2013, **34**, 77-80.
569. Y. Wang and H. Zhou, *Energy Environ. Sci.*, 2011, **4**, 1704-1707.
570. L. Zhang, F. Zhang, G. Huang, J. Wang, X. Du, Y. Qin and L. Wang, *J. Power Sources*, 2014, **261**, 311-316.
571. C. Tran, J. Kafle, X.-Q. Yang and D. Qu, *Carbon*, 2011, **49**, 1266-1271.
572. H. Zhou, *Energy Environ. Sci.*, 2013, **6**, 2256-2256.
573. F. Li, T. Zhang and H. Zhou, *Energy Environ. Sci.*, 2013, **6**, 1125-1141.
574. M. Park, H. Sun, H. Lee, J. Lee and J. Cho, *Adv. Energy Mater.*, 2012, **2**, 780-800.
575. J. Adams, M. Karulkar and V. Anandan, *J. Power Sources*, 2013, **239**, 132-143.
576. L. Grande, E. Paillard, J. Hassoun, J.-B. Park, Y.-J. Lee, Y.-K. Sun, S. Passerini and B. Scrosati, *Adv. Mater.*, 2015, **27**, 784-800.
577. D. Sun, Y. Shen, W. Zhang, L. Yu, Z. Yi, W. Yin, D. Wang, Y. Huang, J. Wang, D. Wang and J. B. Goodenough, *J. Am. Chem. Soc.*, 2014, **136**, 8941-8946.
578. F. S. Gittleston, R. C. Sekol, G. Doubek, M. Linardi and A. D. Taylor, *Phys. Chem. Chem. Phys.*, 2014, **16**, 3230-3237.
579. S. J. Kang, T. Mori, S. Narizuka, W. Wilcke and H.-C. Kim, *Nat. Commun.*, 2014, **5**, 3937.
580. S. T. Kim, N.-S. Choi, S. Park and J. Cho, *Adv. Energy Mater.*, 2015, **5**, 1401030.
581. J. Yuan, J.-S. Yu and B. Sundén, *J. Power Sources*, 2015, **278**, 352-369.
582. L. Ye, W. Lv, K. H. L. Zhang, X. Wang, P. Yan, J. H. Dickerson and W. He, *Energy*, 2015, **83**, 669-673.
583. X. Wang, K. Wen, Y. Song, L. Ye, K. H. L. Zhang, Y. Pan, W. Lv, Y. Liao and W. He, *J. Power Sources*, 2015, **274**, 762-767.
584. I. Landa-Medrano, I. Ruiz de Larramendi, N. Ortiz-Vitoriano, R. Pinedo, J. Ignacio Ruiz de Larramendi and T. Rojo, *J. Power Sources*, 2014, **249**, 110-117.
585. L.-L. Zhang, Z.-L. Wang, D. Xu, X.-B. Zhang and L.-M. Wang, *Int. J. Smart Nano Mater.*, 2013, **4**, 27-46.
586. S. Kang, Y. Mo, S. P. Ong and G. Ceder, *Chem. Mater.*, 2013, **25**, 3328-3336.

Table Captions

- Table 1 Physical properties of solvents commonly used in electrolyte for non-aqueous Li-air batteries
- Table 2 Reported capacities of commercial carbon materials in non-aqueous Li-air batteries
- Table 3 Summary of the composition, size, phase properties, charge-discharge voltages and discharge capacities of the carbon-supported bimetallic gold-platinum nanoparticles with different alloyed phase structure. Reprinted from [ref. 418]
- Table 4 Discharge capacity of cycles 1 and 5 based on various metal oxides. Reprinted from [ref. 193]

Figure Captions

- Fig. 1 Specific energy densities (Wh kg^{-1}) for various types of rechargeable batteries compared to gasoline. For Li-air, the practical value is just an estimate. For gasoline, the practical value includes the average tank-to-wheel efficiency of cars.
- Fig. 2 Schematic of the four different architectures of Li-air battery.
- Fig. 3 Schematic of the nanostructured cathode architecture (a); voltage profile during discharge-charge of cells (to $1000 \text{ mA h g}_{\text{carbon+catalyst}}^{-1}$) based on Super P carbon, Super P carbon coated with Al_2O_3 (Super P carbon+3c ALD Al_2O_3) and Al_2O_3 -coated Super P carbon further coated with Pd nanoparticles (Super P carbon+3c ALD Al_2O_3 +3c ALD Pd) (b); voltage profile during cell discharge-charge (to $500 \text{ mA h g}_{\text{carbon+catalyst}}^{-1}$) based on Al_2O_3 -coated Super P carbon further coated with Pd nanoparticles (c). Reprinted from [ref. 113].
- Fig. 4 Voltages of Li anode and air cathode in Li-air battery at a current density of 0.2 mA cm^{-2} . Reprinted from [ref. 91].
- Fig. 5 Cyclic voltammograms of Li_2O - (a), Li_2O_2 - (b), and Li_2CO_3 - (c) on supported MnO_2 catalyst electrodes for Li-air battery in an O_2 atmosphere at 25°C . Scan rate was 10 mV s^{-1} . Reprinted from [ref. 193].
- Fig. 6 SEM images of various morphologies of lithium peroxide in discharged cathode. Toroidal-shaped (a) [ref. 198], spherical particles (b) [ref. 285], elongated particles (c) [ref. 288], close-packed nanosheets (d), [ref. 290] rough thin films (e) [ref. 291], and porous ball-like (f) [ref. 293].
- Fig. 7 TEM images of different parts of the oxygen electrode discharged at $10000 \text{ mAh g}_{\text{carbon}}^{-1}$ (0.5 mA cm^{-2} current, 1 mg cm^{-2} carbon loading). Image (a) shows the

electrode morphology characterized by a mixture of amorphous solid Li_2O_2 particles combined with perfect spherical hollow particles having wall thickness of about 50 nm; Image (b) shows a Li_2O_2 particle covered by 10 nm size crystalline primary nanoparticles; Inset images of (a and b) show selected area electron diffraction patterns of the particles; the high-resolution TEM image (c) shows the crystalline nature of the primary particles. Reprinted from [ref. 282].

Fig. 8 Morphologic growth process of discharge products at different discharge capacities of pristine (a, b), 150 (c), 200 (d), 250 (e), 300 (f), 400 (g), 500 (h), 600 (i), 800 (j), 1000 (k), and 1300 $\text{mA h g}_{\text{carbon}}^{-1}$ (l). Reprinted from [ref. 177].

Fig. 9 SEM images showing spatial distribution of Li_2O_2 toroids on the surface of different catalyst-containing electrodes as a function of where the image is collected, area (1) represents the periphery of the electrode, (2) the intermediate region, and (3) represents the central area as shown in the accompanying diagram; for (a) pristine $\text{Na}_{0.44}\text{MnO}_2/\text{carbon}$, (b) carbon with no catalyst, and (c) acid-leached $\text{Na}_{0.44}\text{MnO}_2/\text{carbon}$. The center image is the schematic showing the electrode region sampled. The scale bar of 1 mm refers to all of the micrographs shown. Reprinted from [ref. 196].

Fig. 10 Morphologic decomposition process of discharge products at different charge capacities after a discharge capacity of 1000 $\text{mA h g}_{\text{carbon}}^{-1}$: 200 (a), 400(b), 600 (c), 750 (d), 900 (e) and 1000 $\text{mA h g}_{\text{carbon}}^{-1}$ (f). Voltage profile during reversible charge after discharge and the red dots represent different charged capacity (g). Reprinted from [ref. 177].

Fig. 11 Approaches to build up an ideal cathode for non-aqueous Li-air battery.

Fig. 12 Charge-discharge performance of Li-air battery with GNSs, BP-2000 and Vulcan

XC-72 cathodes at a current density of 75 mA g^{-1} (a); SEM and TEM images of GNS electrodes before (b and c) and after (d and e) discharge. Reprinted from [ref. 350].

Fig. 13 Schematic graphs of Super P carbon black (a) and MCF-C (b) after discharge, the discharge curves of MCF-C (solid) and Super P carbon black (dash) at various current densities (c). Reprinted from [ref. 175].

Fig. 14 FESEM images of HCC-400 (a, b) and HCC-100 (c, d); TEM images of HCC-100 (e, f); discharge characteristic of Li-air battery at the current density of 0.05 mA cm^{-2} (g) and various current densities (h). Reprinted from [ref. 204].

Fig. 15 TEM images of GNSs (a) and N-doped GNSs (b); XPS spectra of GNSs and N-doped GNSs, the inset is N 1s spectra of two samples (c); Voltage profiles of GNSs and N-doped GNSs electrodes at various current densities (d). Reprinted from [ref. 299].

Fig. 16 First charge/discharge profiles of carbon at $85 \text{ mA g}_{\text{carbon}}^{-1}$ and of Au/C, Pt/C, and PtAu/C at $100 \text{ mA g}_{\text{carbon}}^{-1}$ (a); Charge/discharge profiles of carbon (black, $85 \text{ mA g}_{\text{carbon}}^{-1}$) and PtAu/C (red, $100 \text{ mA g}_{\text{carbon}}^{-1}$) in the third cycle at $0.04 \text{ mA cm}^{-2}_{\text{electrode}}$ (b). Reprinted from [ref. 110].

Fig. 17 Schematic illustration of the synthesis process of Ru-carbon (a); TEM image and crystal size distribution of Ru nanocrystals (b); Charge-discharge curves of the first two cycles for Ru-carbon (solid line) and carbon electrode (dash line) (c); Cycling performance of the Li-air battery with Ru-carbon catalyst at $200 \text{ mA g}_{\text{carbon}}^{-1}$ with a curtaining capacity of $1000 \text{ mAh g}_{\text{carbon}}^{-1}$ (d). Reprinted from [ref. 423].

Fig. 18 TEM/SEM images of bulk and nanowire forms of α - and β - MnO_2 polymorphs showing their morphologies and surface areas (a); Variation of discharge capacity

with cycle number for several porous electrodes containing various manganese oxides as catalysts at a current density of $70 \text{ mA g}_{\text{carbon}}^{-1}$ in 1 atm of O_2 (b); the 2nd, 3th and 5th cycle discharge-charge curves of $\alpha\text{-MnO}_2$ nanowires electrode at a rate of $70 \text{ mA g}_{\text{carbon}}^{-1}$ (c). Reprinted from [ref. 94].

Fig. 19 SEM (a) and TEM (b) image, SAED pattern (inset b) of MNWs; Charge/discharge curves with a restricting capacity at a current density of 100 mA g^{-1} (c); Discharge capacities at different current densities (d); Variation of discharge capacity with cycle number at a current density of 0.05 mA cm^{-2} (e). Reprinted from [ref. 441].

Fig. 20 SEM micrographs of nanosheet (a-c), nanoneedle (d-f) and nanoflower (g-i) Co_3O_4 ; Charge-discharge profiles of the carbon-free Co_3O_4 cathodes at a current density of $20 \text{ mA g}_{\text{catalyst}}^{-1}$ (j); Plots of capacity vs. cycle number for the Co_3O_4 -only cathodes (k). Reprinted from [ref. 446].

Fig. 21 Cubic perovskite structure (a) Reprinted from [ref. 453], Double perovskite structure (b) Reprinted from [ref. 481], and layered perovskite structure (c) Reprinted from [ref. 483].

Fig. 22 FESEM (a, b) and TEM (c, d) images of PNT-LSM catalyst; Cyclic performance, charge/discharge specific capacity and coulombic efficiency of Li-air battery with (e,f) and without (g,h) PNT-LSM catalyst at a current density of 0.025 mA cm^{-2} ; Voltage of the terminal discharge vs. the cycle number for Li-air battery with and without PNT-LSM catalyst at a current density of 0.15 mA cm^{-2} (i). Reprinted from [ref. 312].

Fig. 23 Microstructural analysis of Ru-rGO and $\text{RuO}_2 \cdot 0.64\text{H}_2\text{O}$ -rGO hybrids: SEM image and SEM-EDX (inset) of porous Ru-rGO hybrid (a); TEM images of Ru-rGO hybrid (inset: HRTEM image) (b); particle size distribution of Ru-rGO hybrid (c); SEM

image and SEM-EDX (inset) of porous $\text{RuO}_2 \cdot 0.64\text{H}_2\text{O}$ -rGO hybrid (d); TEM images of $\text{RuO}_2 \cdot 0.64\text{H}_2\text{O}$ -rGO hybrid (inset: HRTEM) (e); and particle size distribution of $\text{RuO}_2 \cdot 0.64\text{H}_2\text{O}$ -rGO hybrid (f); Charge-discharge cycles of Li-air cells using rGO, Ru-rGO hybrid, and $\text{RuO}_2 \cdot 0.64\text{H}_2\text{O}$ -rGO hybrid under a limited specific capacity of 5000 mAh g^{-1} at a current density of 500 mA g^{-1} : Voltage profiles of fifth cycle (g) and following cycles of Ru-rGO hybrid (h) and $\text{RuO}_2 \cdot 0.64\text{H}_2\text{O}$ -rGO hybrid (i). Reprinted from [ref. 368].

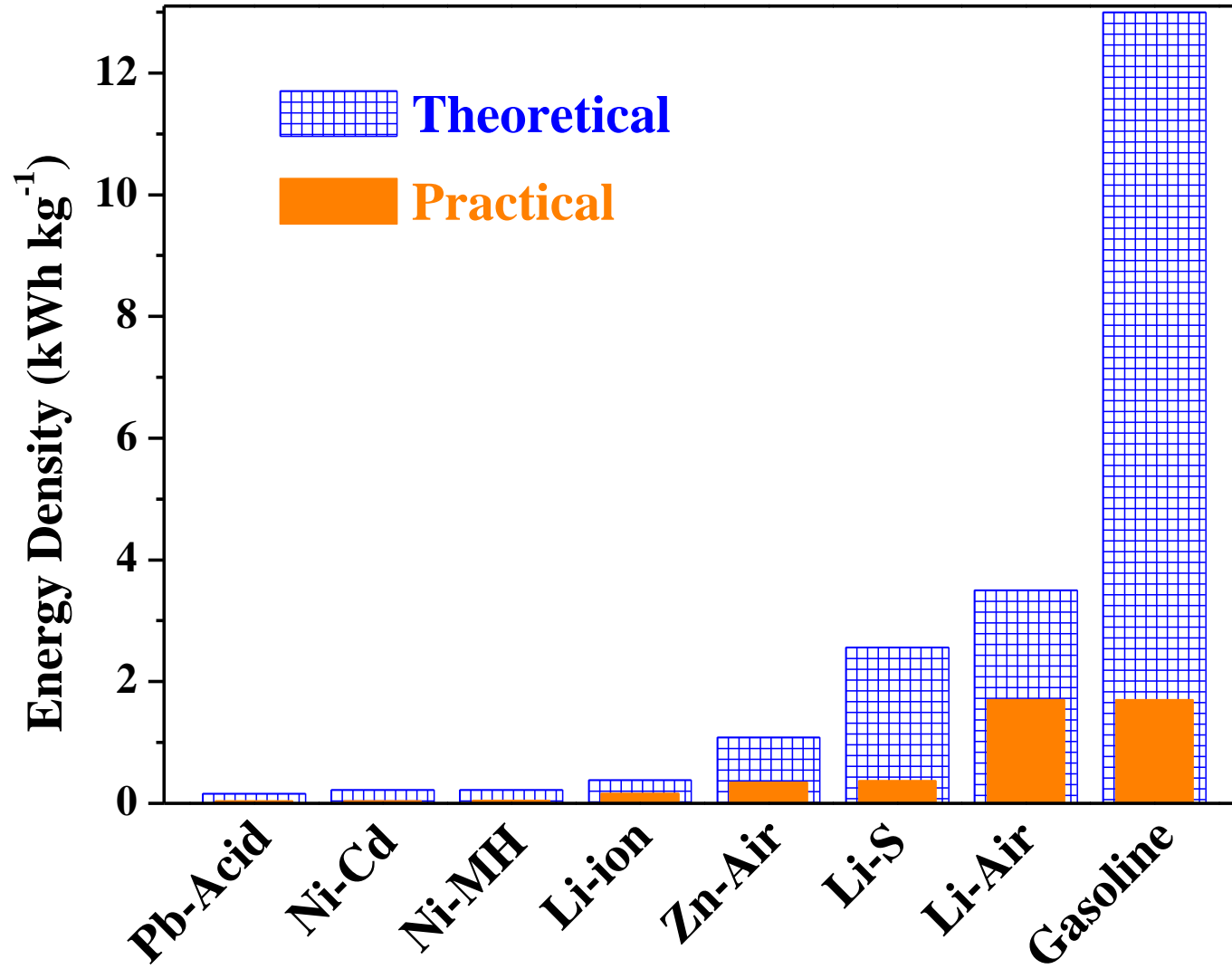
Fig. 24 SEM (a) and TEM (b) images of the N-Fe-MOF catalysts; Initial discharge performance for various catalysts in Li-air battery tests at a current density of $50 \text{ mA g}_{\text{catalyst}}^{-1}$ (c); Cycling test of the N-Fe-MOF catalyst at a current density of $400 \text{ mA g}_{\text{catalyst}}^{-1}$ with voltage cutoff at 2.5 V (discharge) and 4.1 V (charge) (d). Reprinted from [ref. 524].

Fig. 25 SEM (a) and TEM (b) images of Co-C composite; the initial discharge curves of Co-C and pure KB electrodes at a current density of $300 \text{ mA g}_{\text{carbon}}^{-1}$ (c); Curtailing capacity of $600 \text{ mAh g}_{\text{carbon}}^{-1}$ at a current density of $200 \text{ mA g}_{\text{carbon}}^{-1}$ (d). Reprinted from [ref. 526].

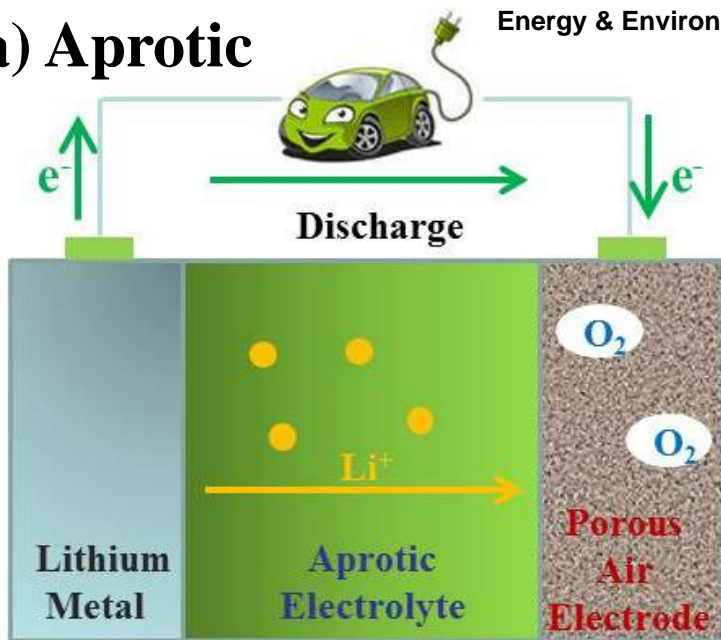
Fig. 26 SEM images of TPPy (a) and GPPy (b); Charge/discharge curves of AB, GPPy and TPPy supported Li-air battery at 0.1 mA cm^{-2} in oxygen (c), at 0.1 mA cm^{-2} in argon (d) and at 0.5 mA cm^{-2} in oxygen (e); Cycling performance of AB, GPPy and TPPy supported Li-air battery at current densities of 0.1 and 0.5 mA cm^{-2} , respectively, (f). Reprinted from [ref. 311].

Fig. 27 Schematic mechanism of the dissociation of Li_2O_2 (a) using an air electrode composed of carbon and oxide catalyst and (b) using an air electrode and an additionally dissolved catalyst (LiI) as redox mediator. Reprinted from [ref. 259].

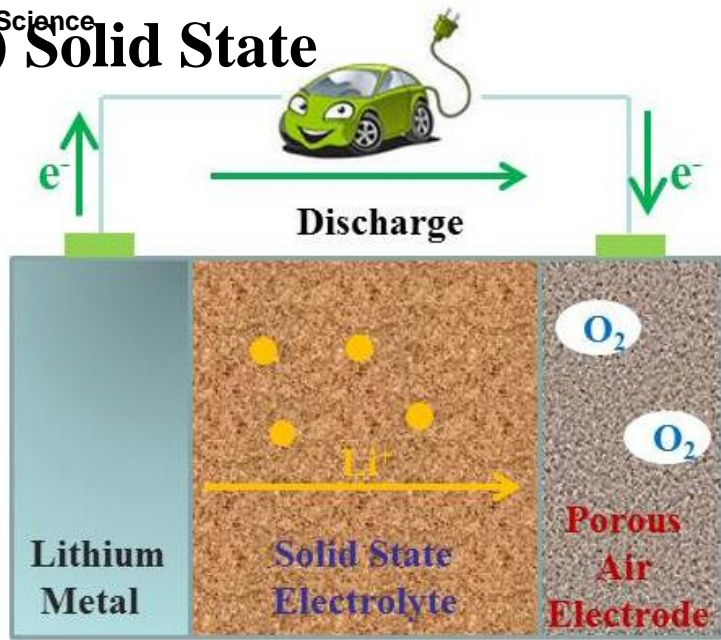
- Fig. 28 Schematic illustration of a Li-air battery using MOF-Super P composite as the air electrode, where oxygen molecules relative sizes are reduced for clarity (a); Discharge profiles of the Li-air battery using MOF-Super P composites or Super P only under O_2 atmosphere with a current of $50 \text{ mA g}_{\text{catalyst+carbon}}^{-1}$ at room temperature (b). Reprinted from [ref. 548].
- Fig. 29 Maximum specific capacity of a porous carbon air electrode. Reprinted from [ref. 91].
- Fig. 30 Schematic representations comparing the conventional air electrode with the SWNT/[C_2C_{1im}][NTf_2] CNG air electrode. (a) Air electrode using a conventional carbonaceous material such as acetylene black; (b) SWNT/[C_2C_{1im}][NTf_2] CNG; (c) Three dimensional tri-continuous passage of electrons, ions, and oxygen. SWNTs: gold; [C_2C_{1im}]⁺: green; [NTf_2]⁻: purple. Reprinted from [ref. 355].
- Fig. 31 Illustration of the proposed mechanism realizing the formation of an artificial three-phase reaction zone in Li-air cathode: Channels inside the pristine porous carbon (a); Channels are flooded with an organic electrolyte (in blue) thus, only dissolved oxygen is participating in the reduction reaction (b); Different possibilities of two distinct subsystem channels, G_{PFC} (in yellow) and G_{Li-ion} , formed as a result of the PFC treatment (c,d). Reprinted from [ref. 559].

**Fig. 1**

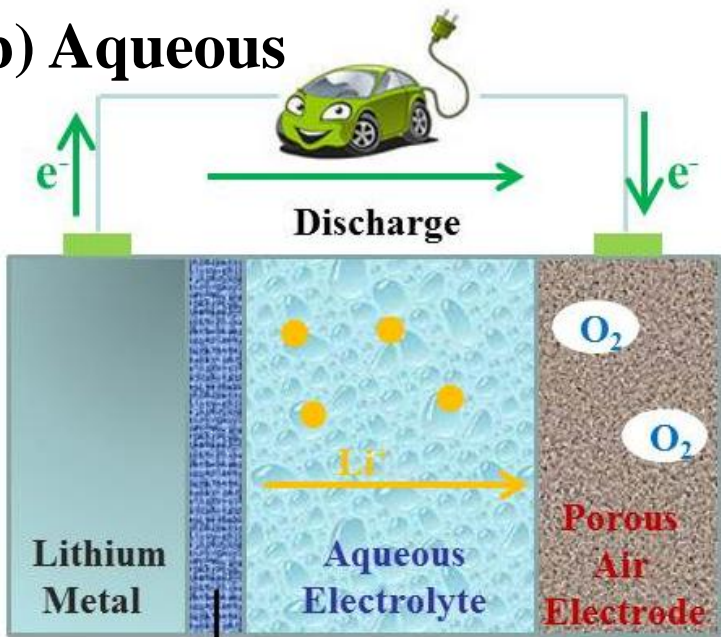
(a) Aprotic



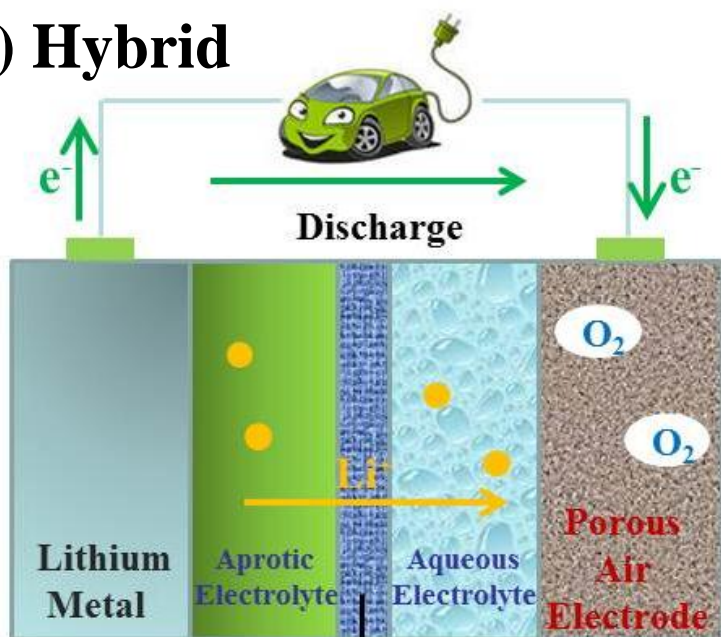
(c) Solid State



(b) Aqueous



(d) Hybrid

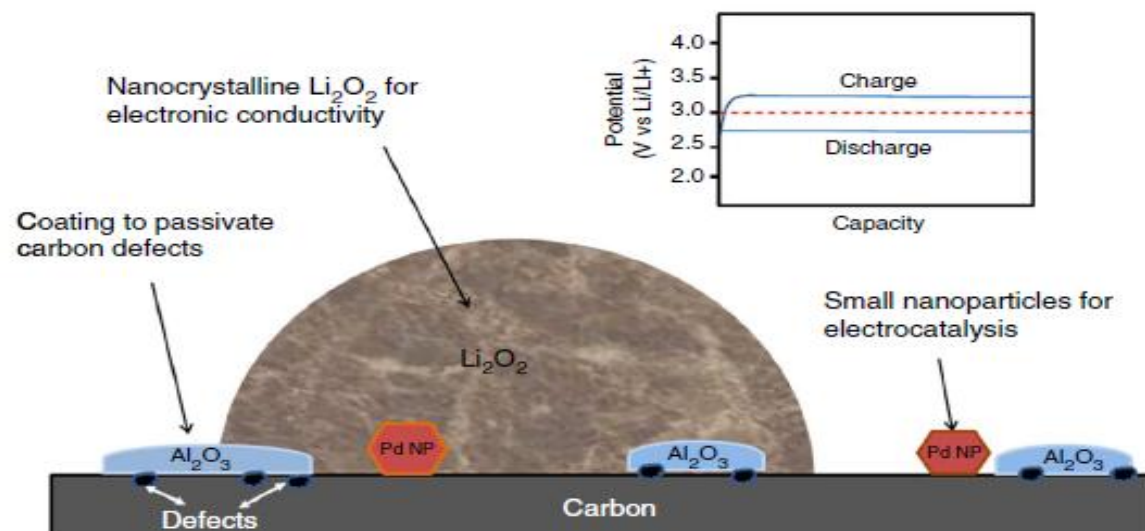


Li⁺ conducting membrane

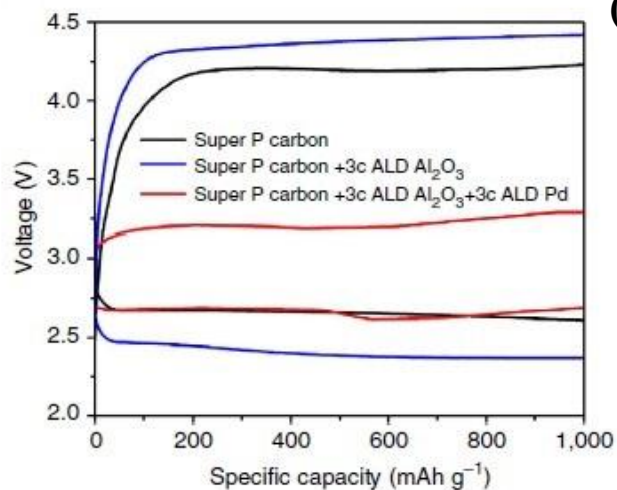
Li⁺ conducting membrane

Fig. 2

(a)



(b)



(c)

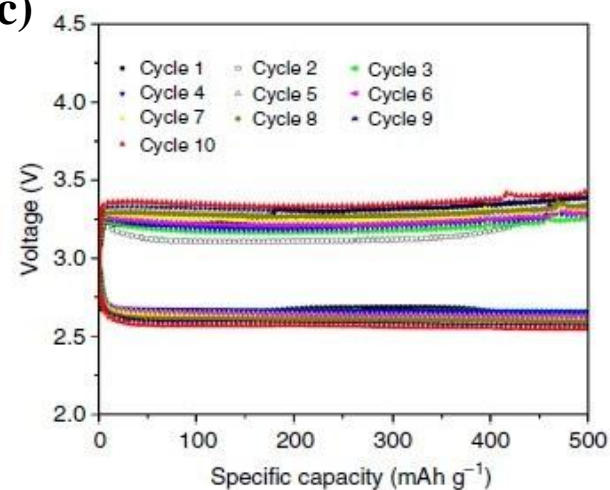


Fig. 3

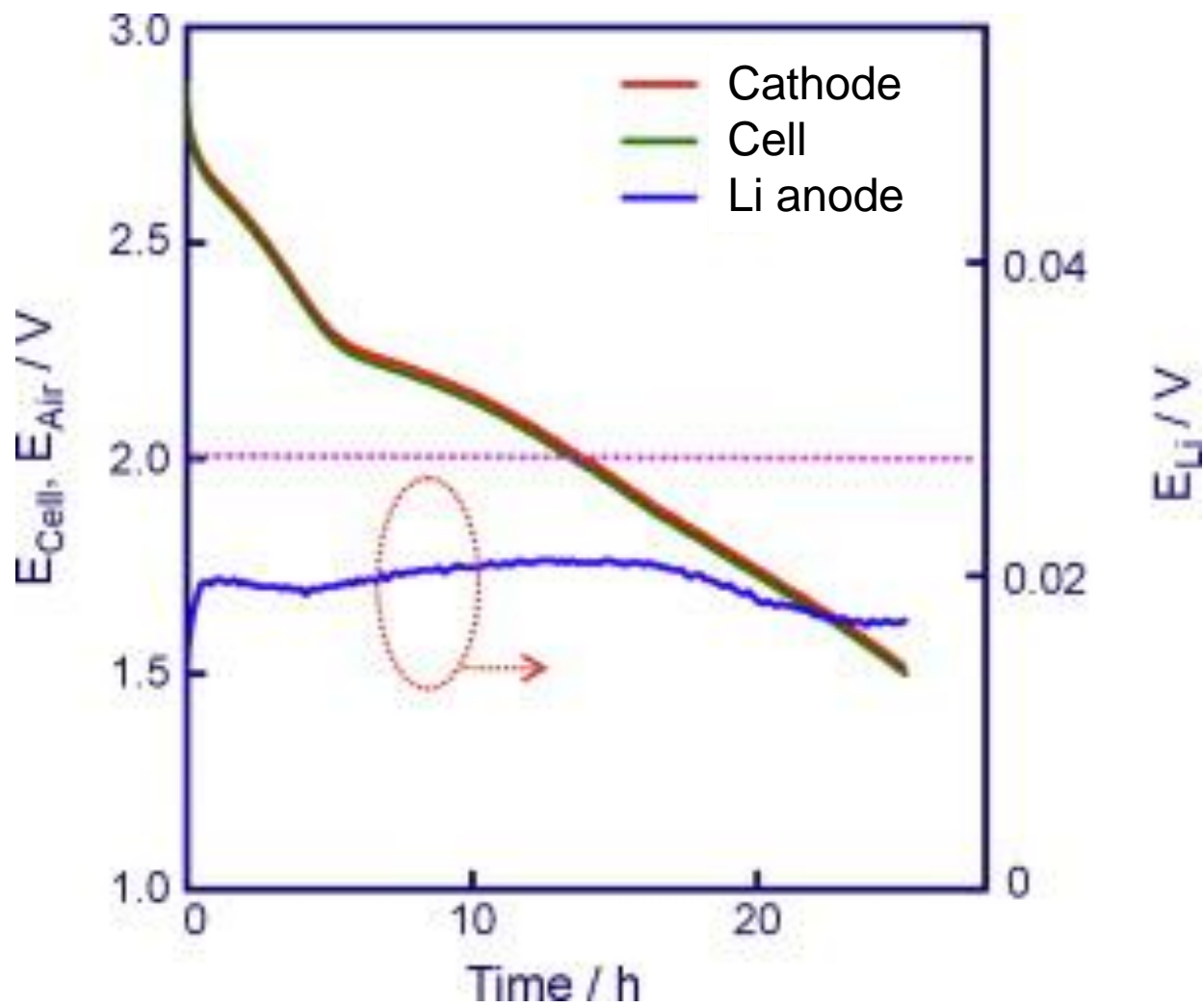


Fig. 4

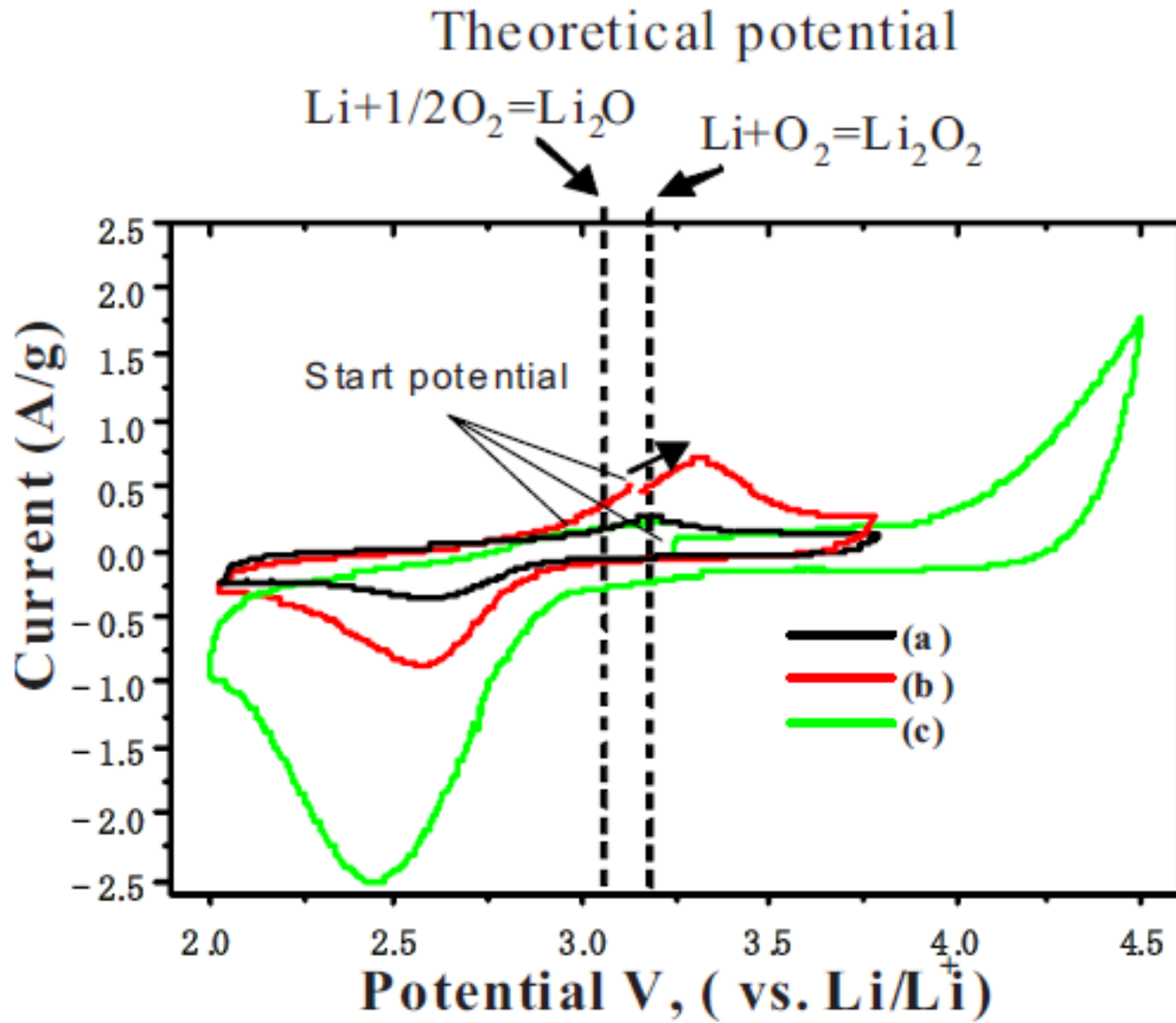


Fig. 5

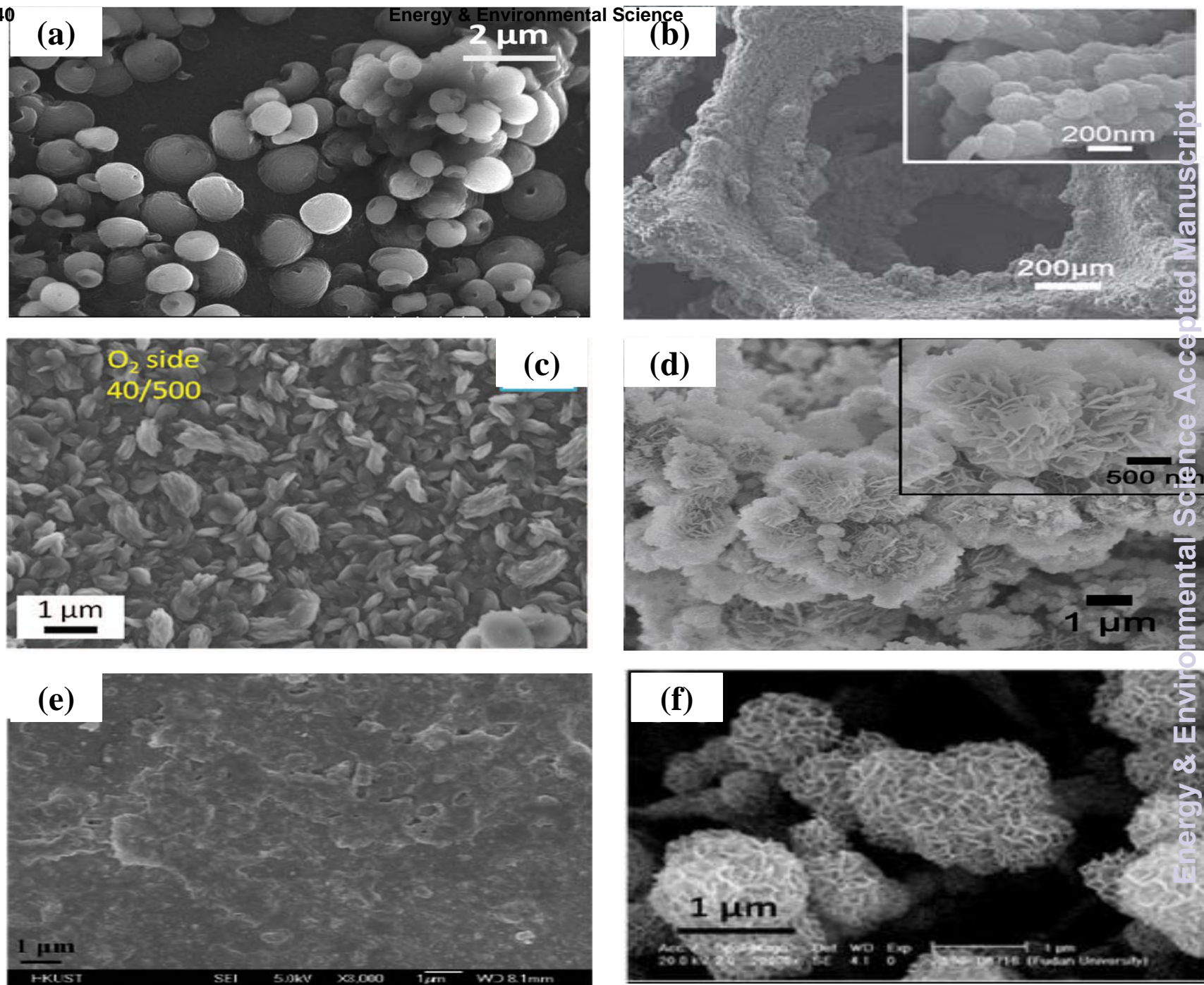


Fig. 6

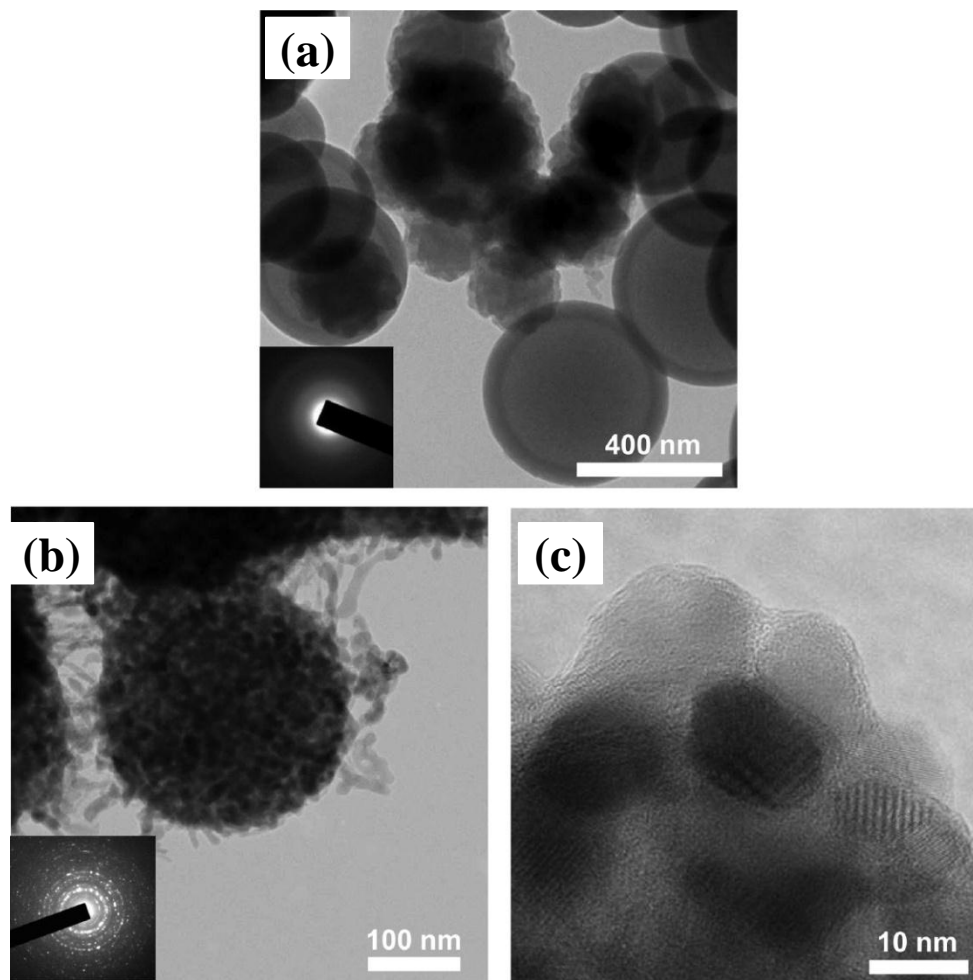


Fig. 7

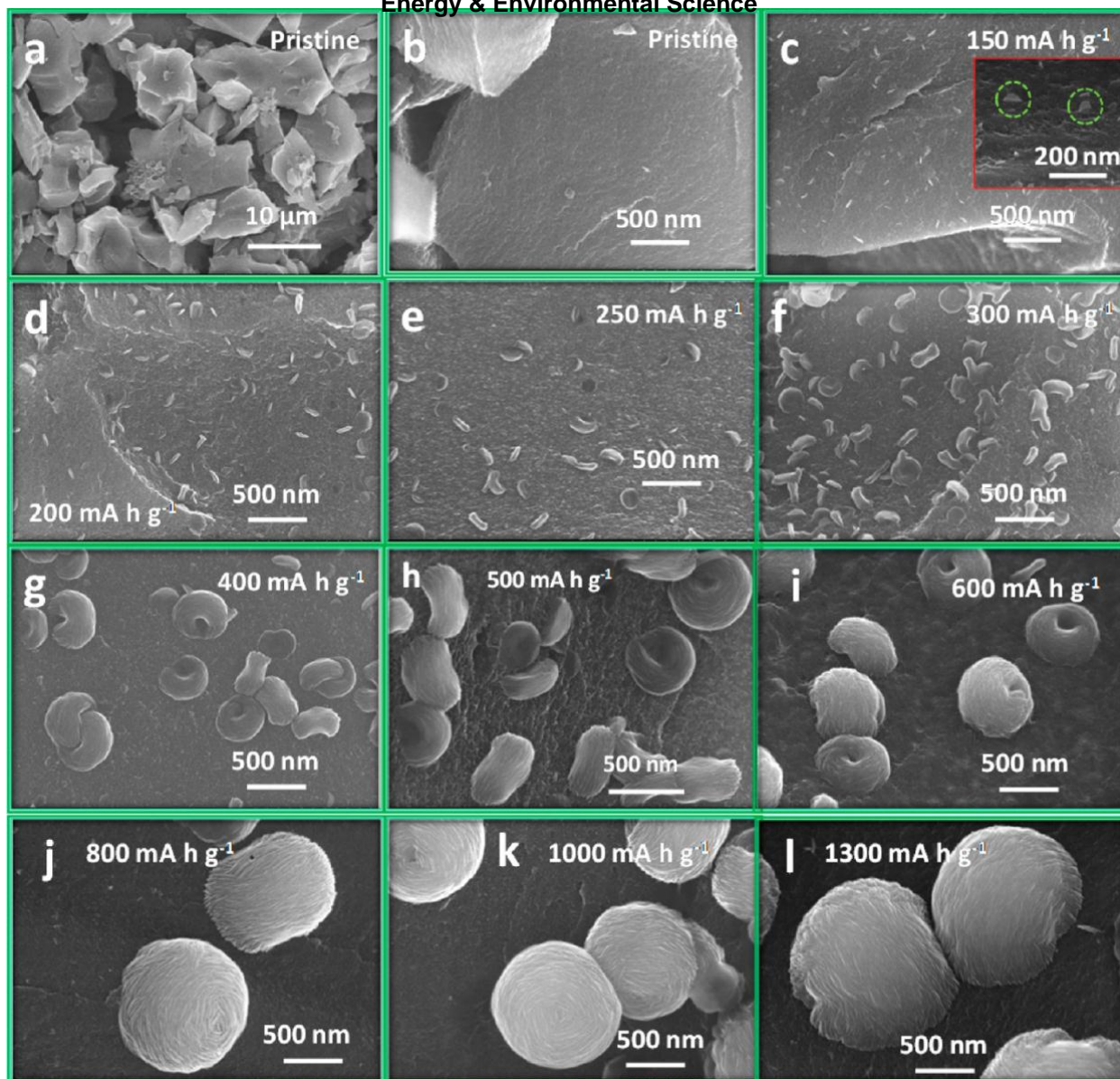


Fig. 8

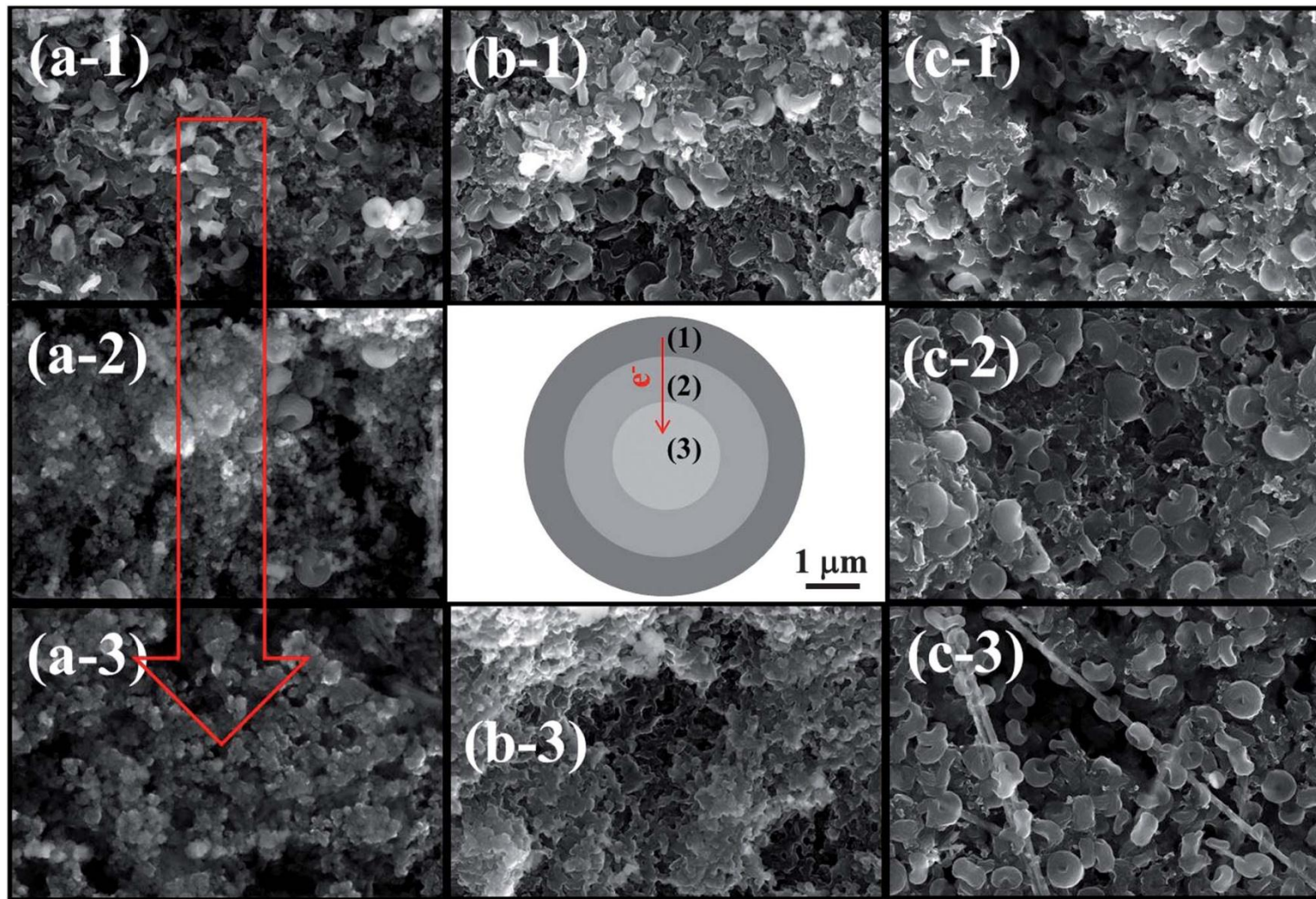


Fig. 9

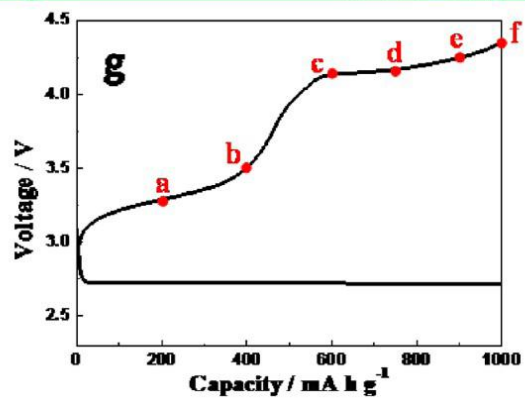
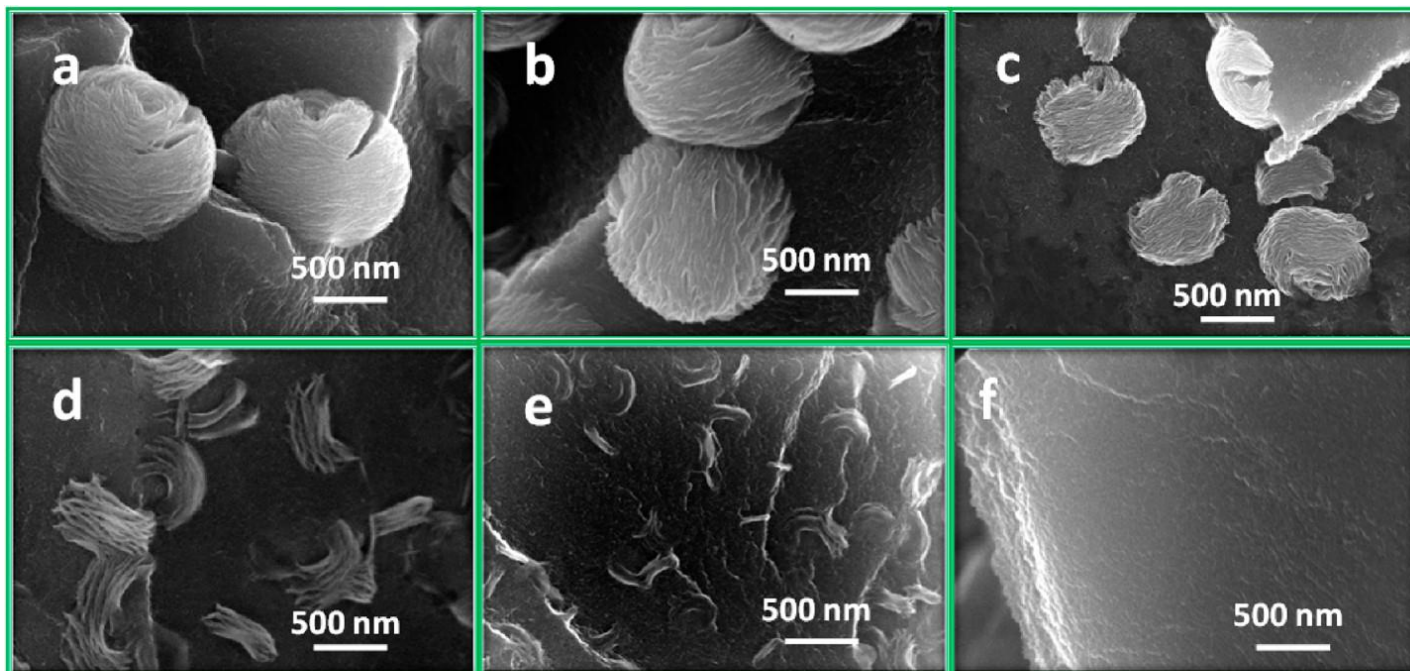
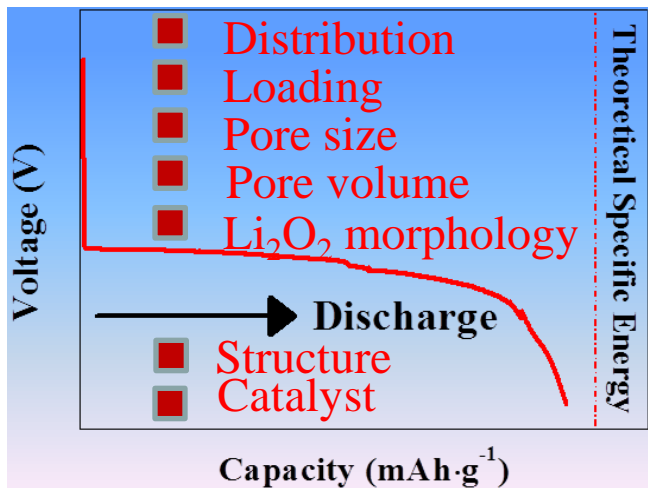


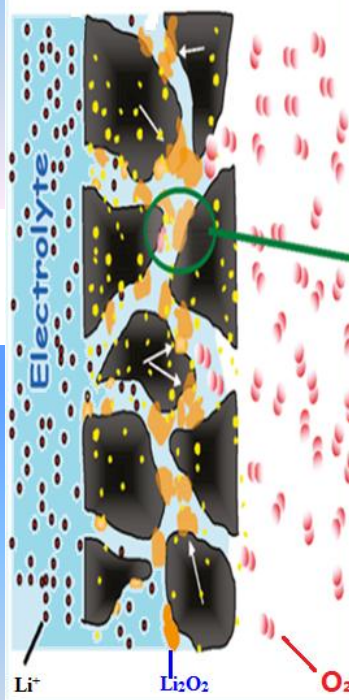
Fig. 10

Specific Capacity



Cathode

Porous Cathode



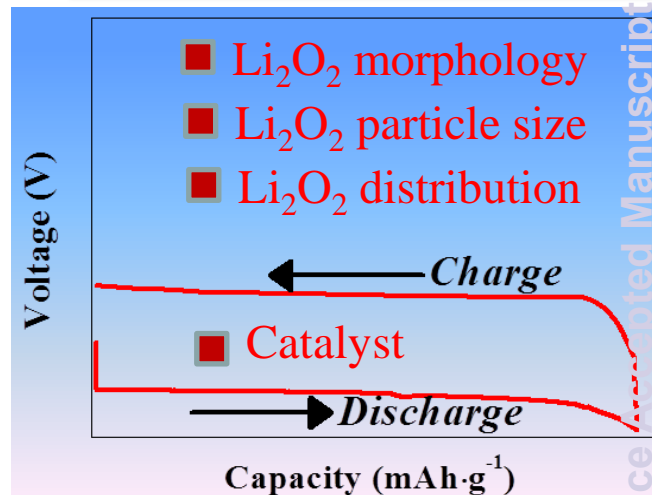
Materials

Process

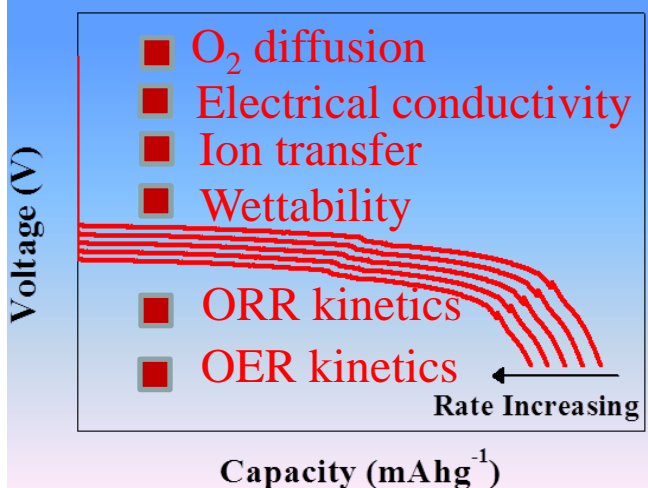
Structure

Catalysis

Round-trip Efficiency



Rate Capability



Cycling Performance

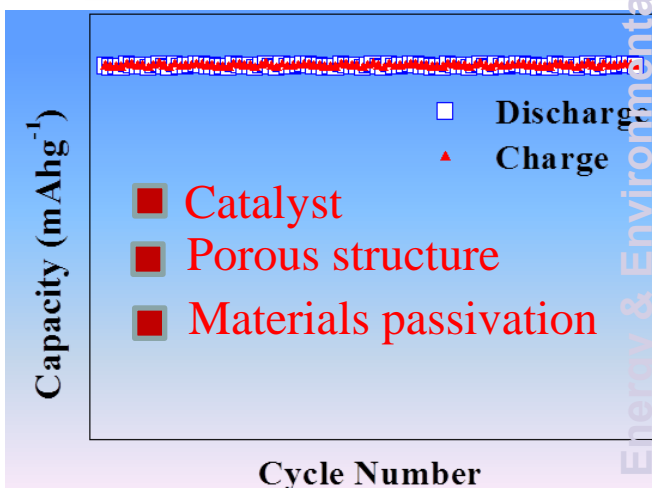


Fig. 11

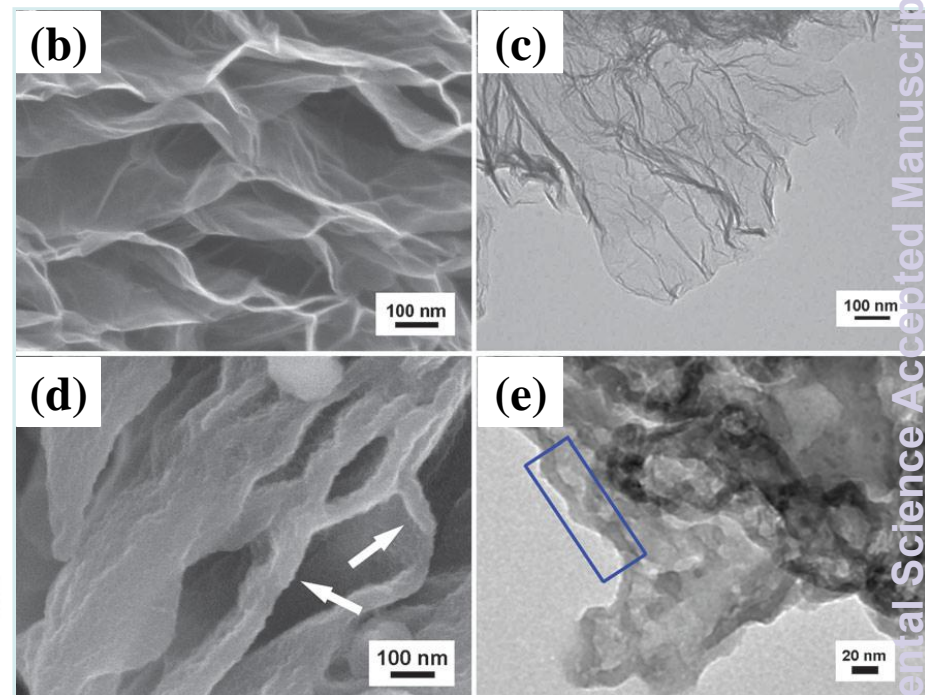
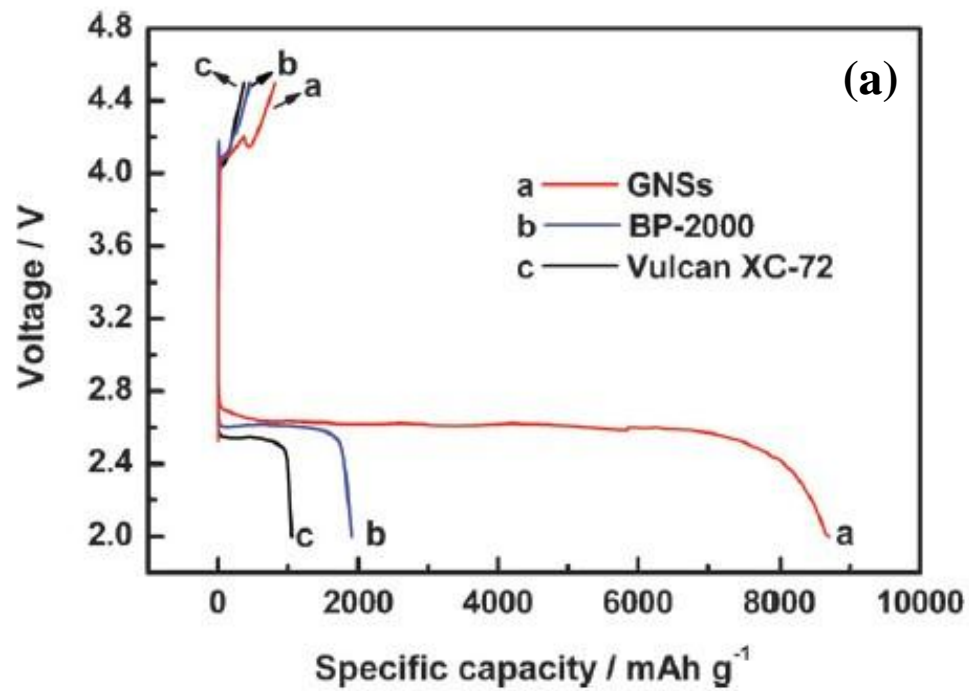


Fig. 12

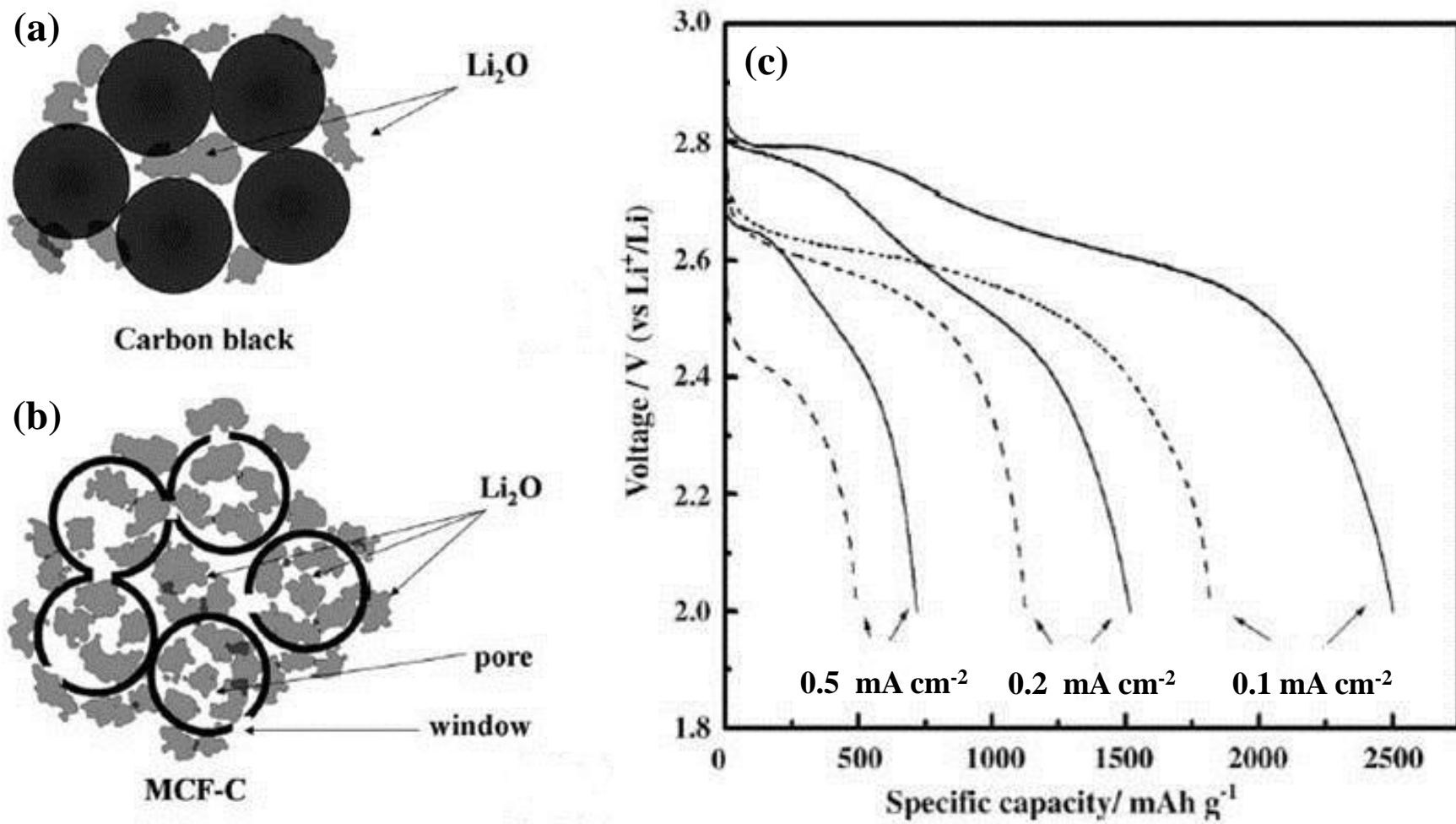


Fig. 13

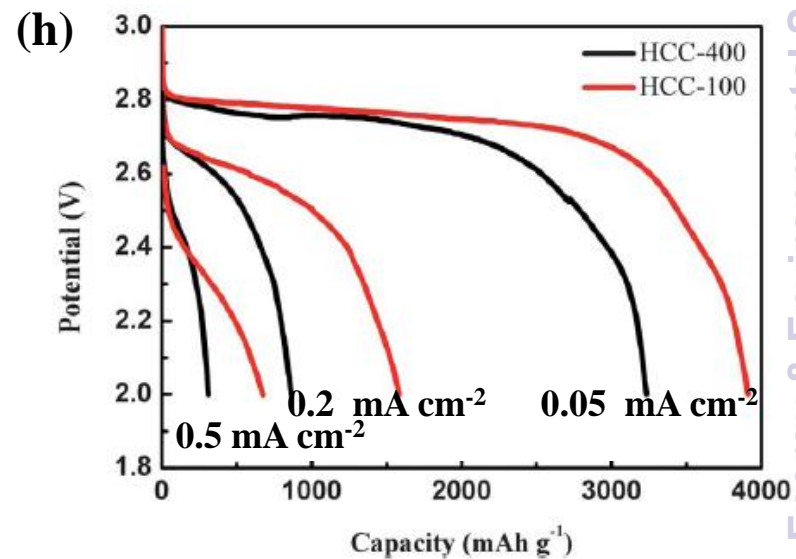
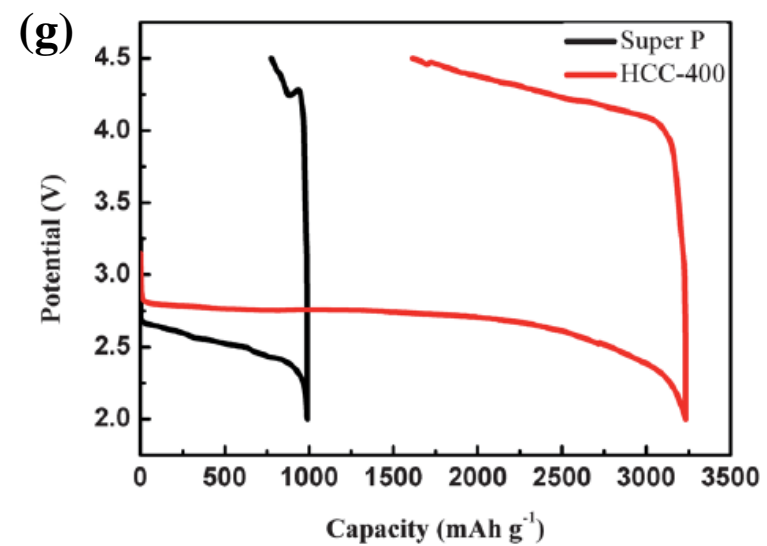
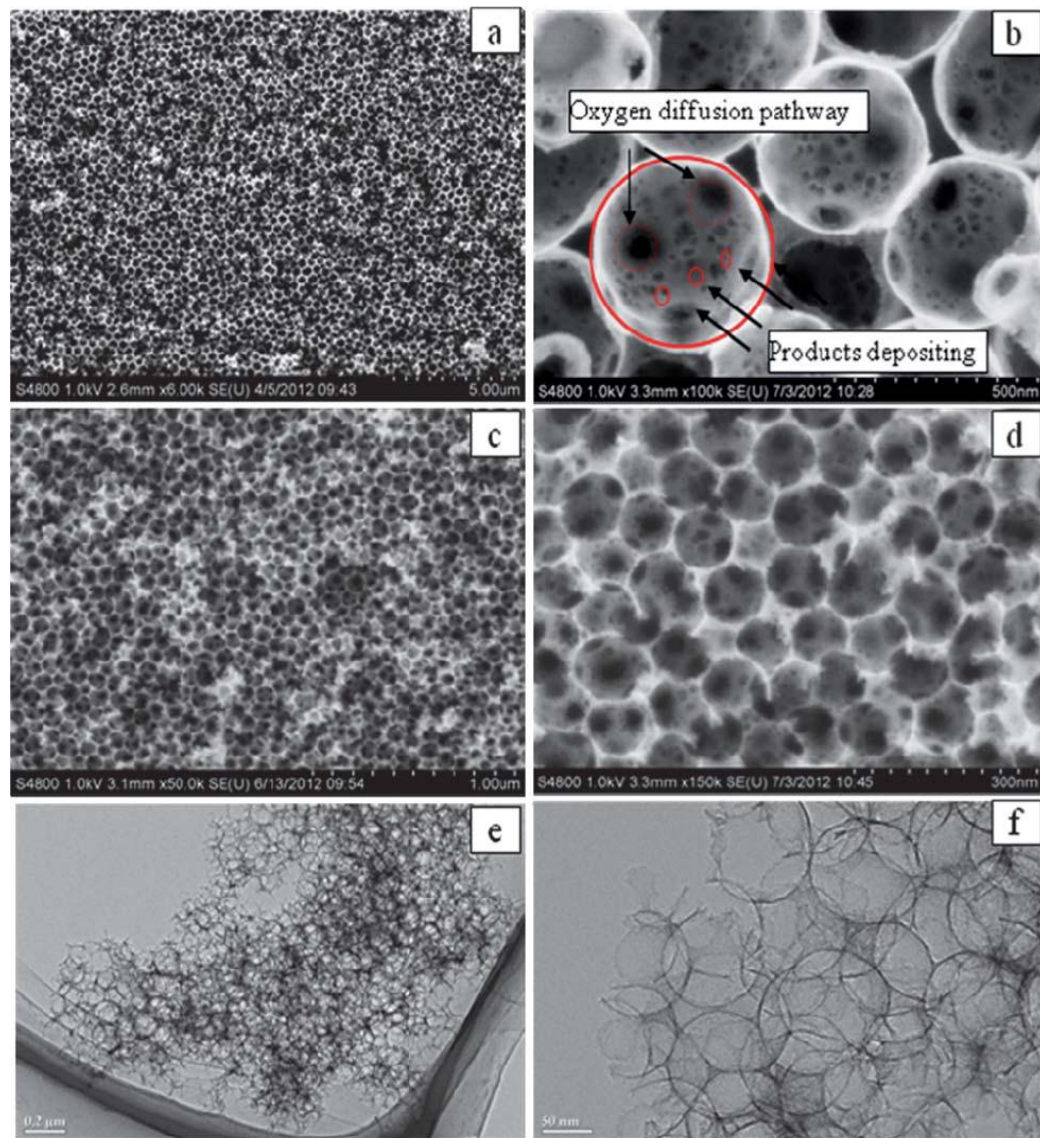


Fig. 14

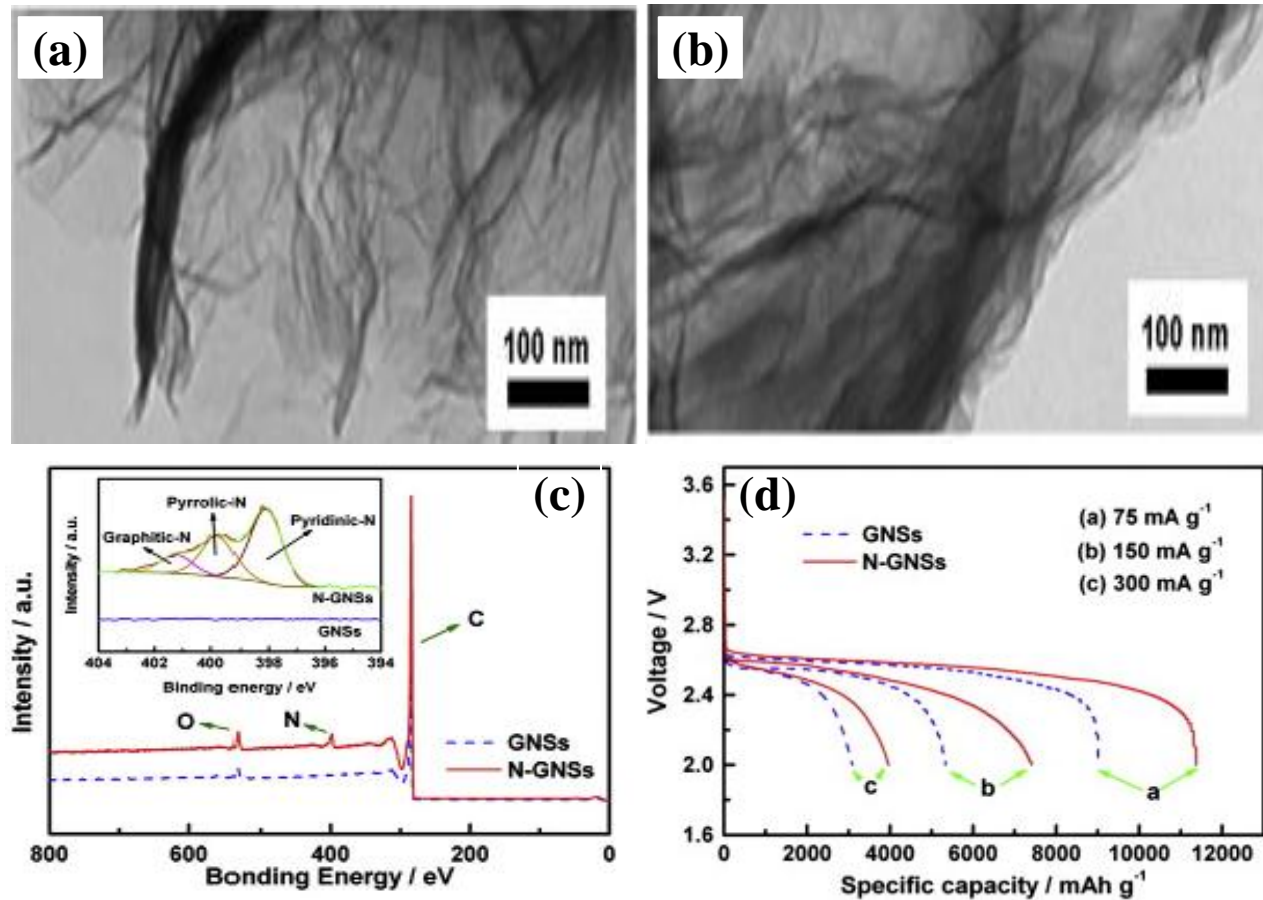


Fig. 15

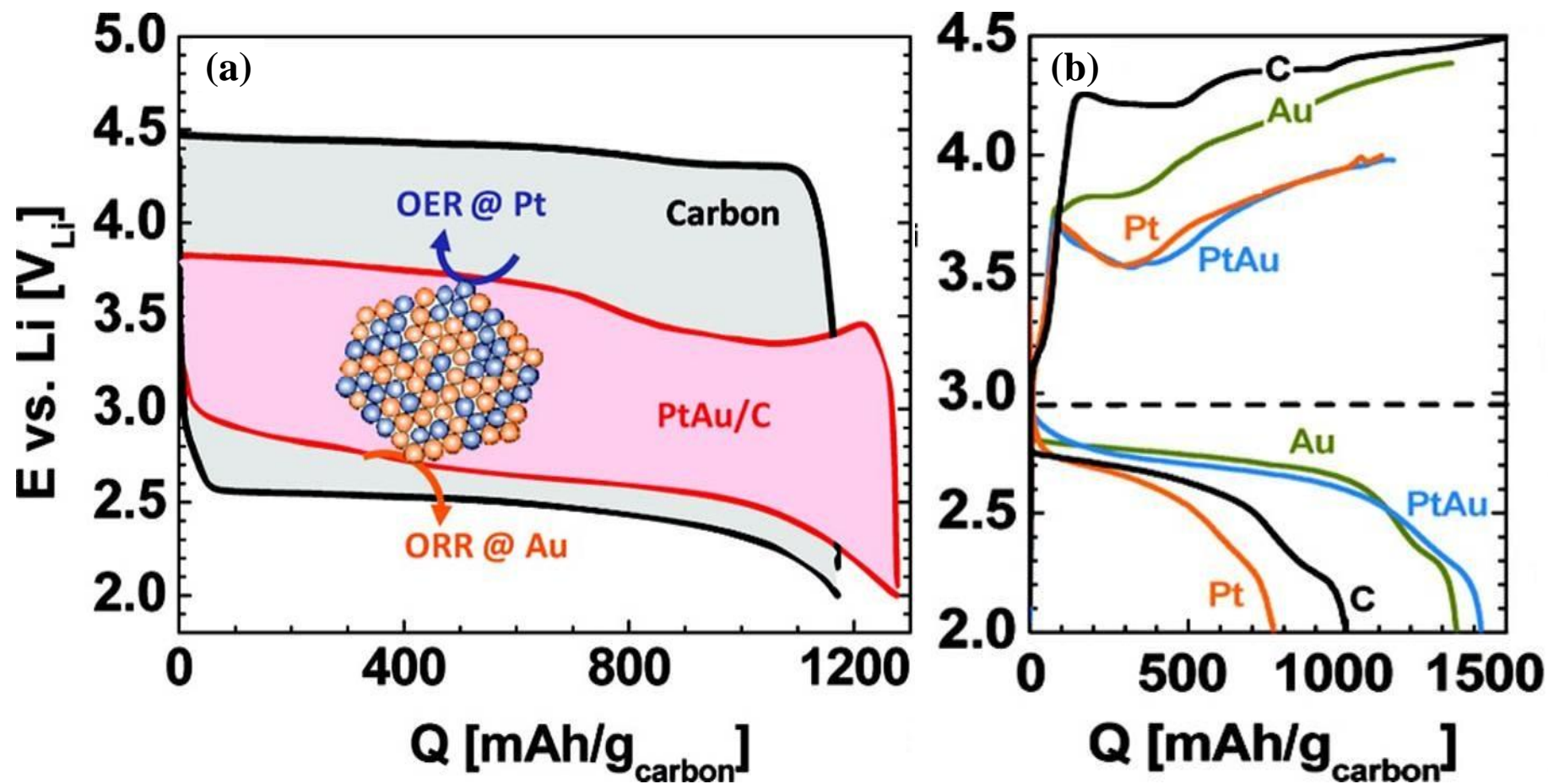


Fig. 16

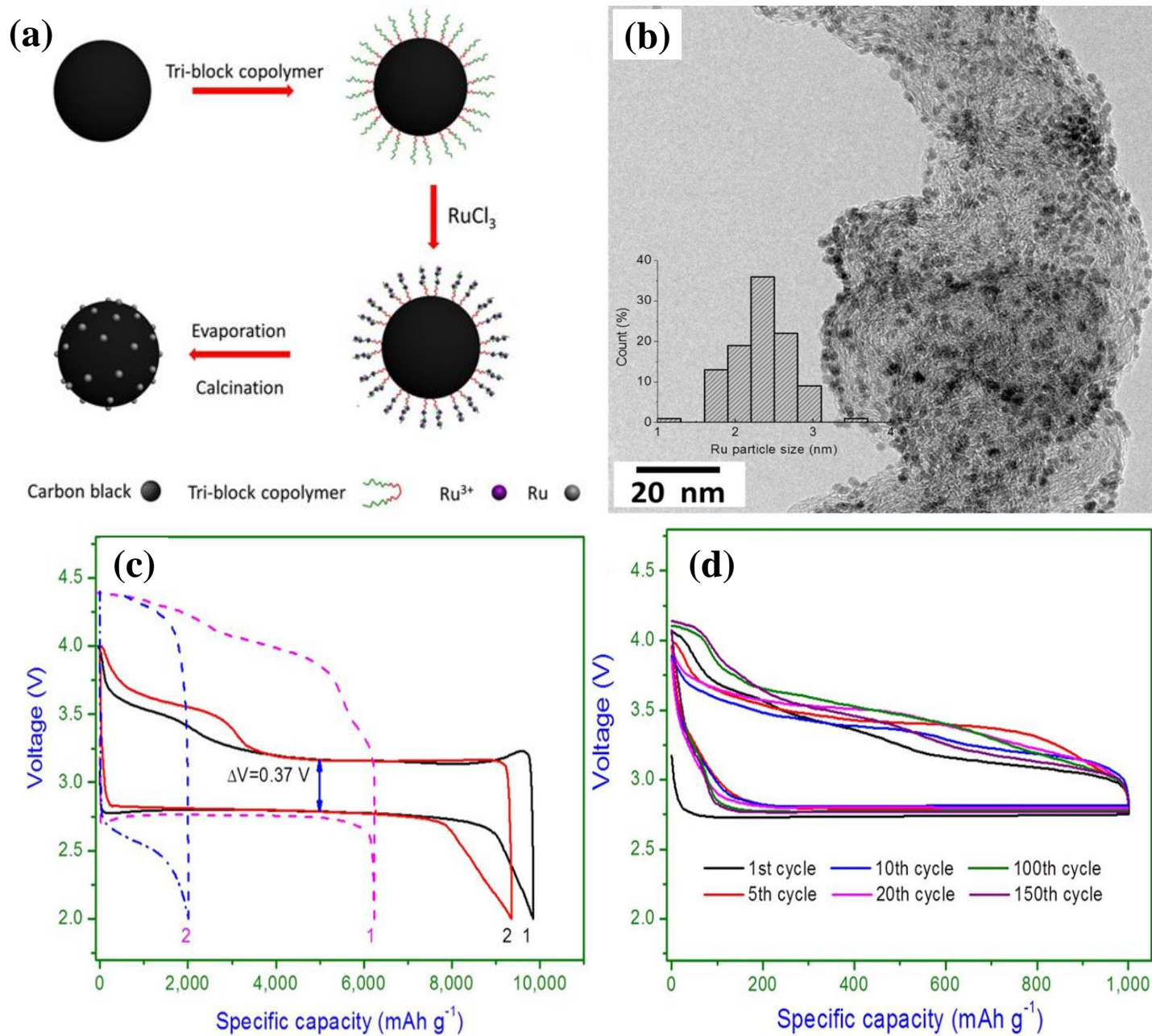


Fig. 17

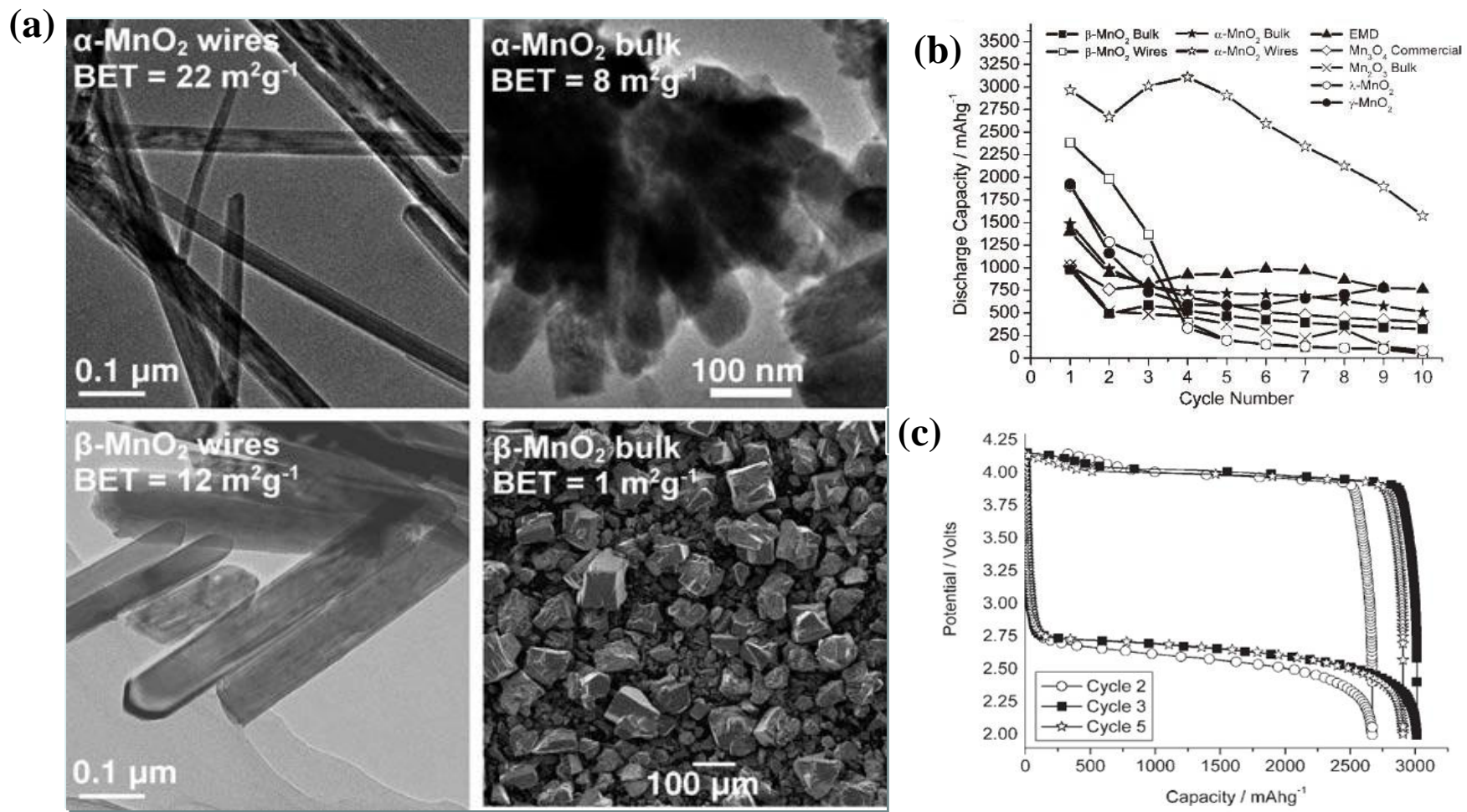


Fig. 18

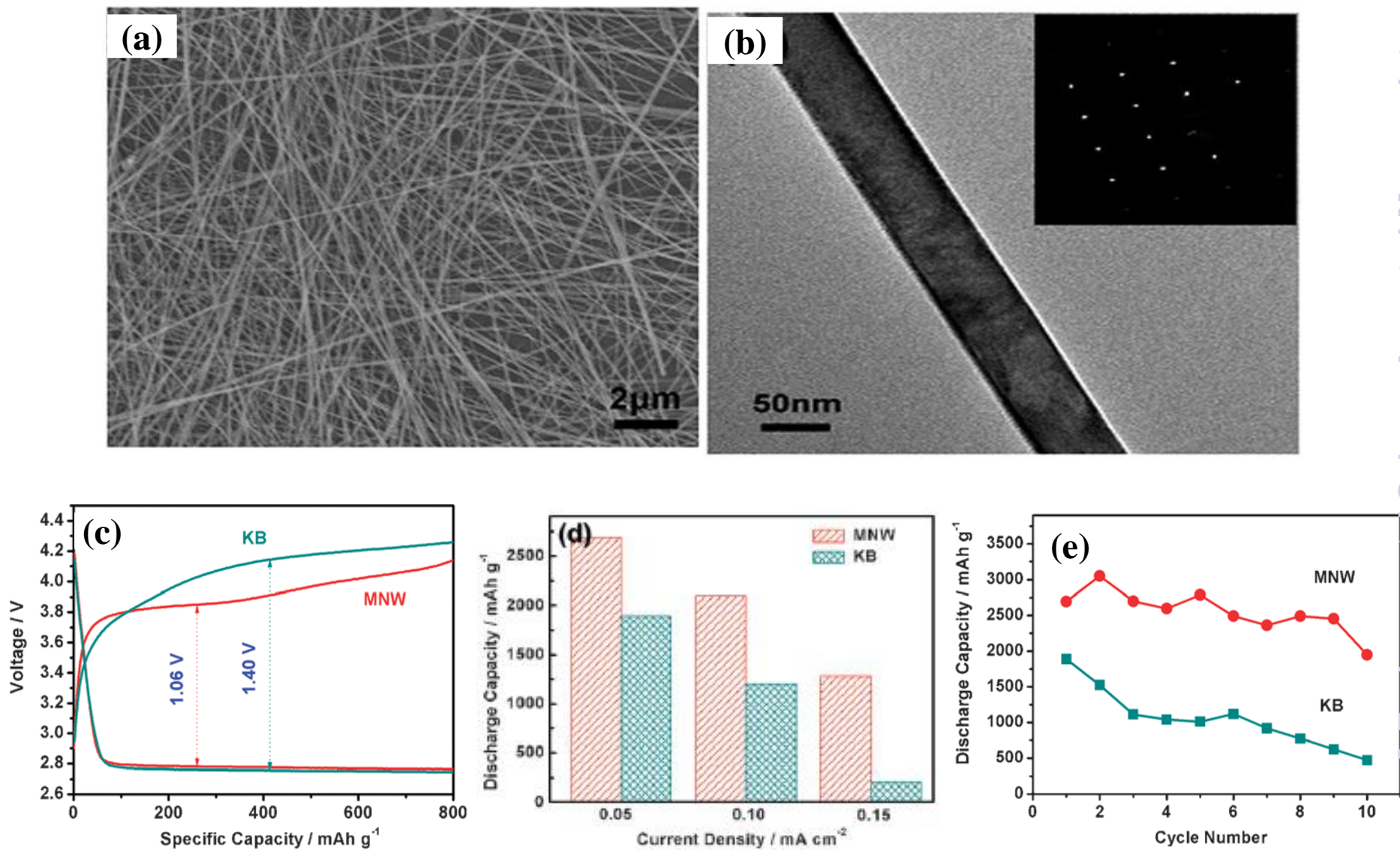


Fig. 19

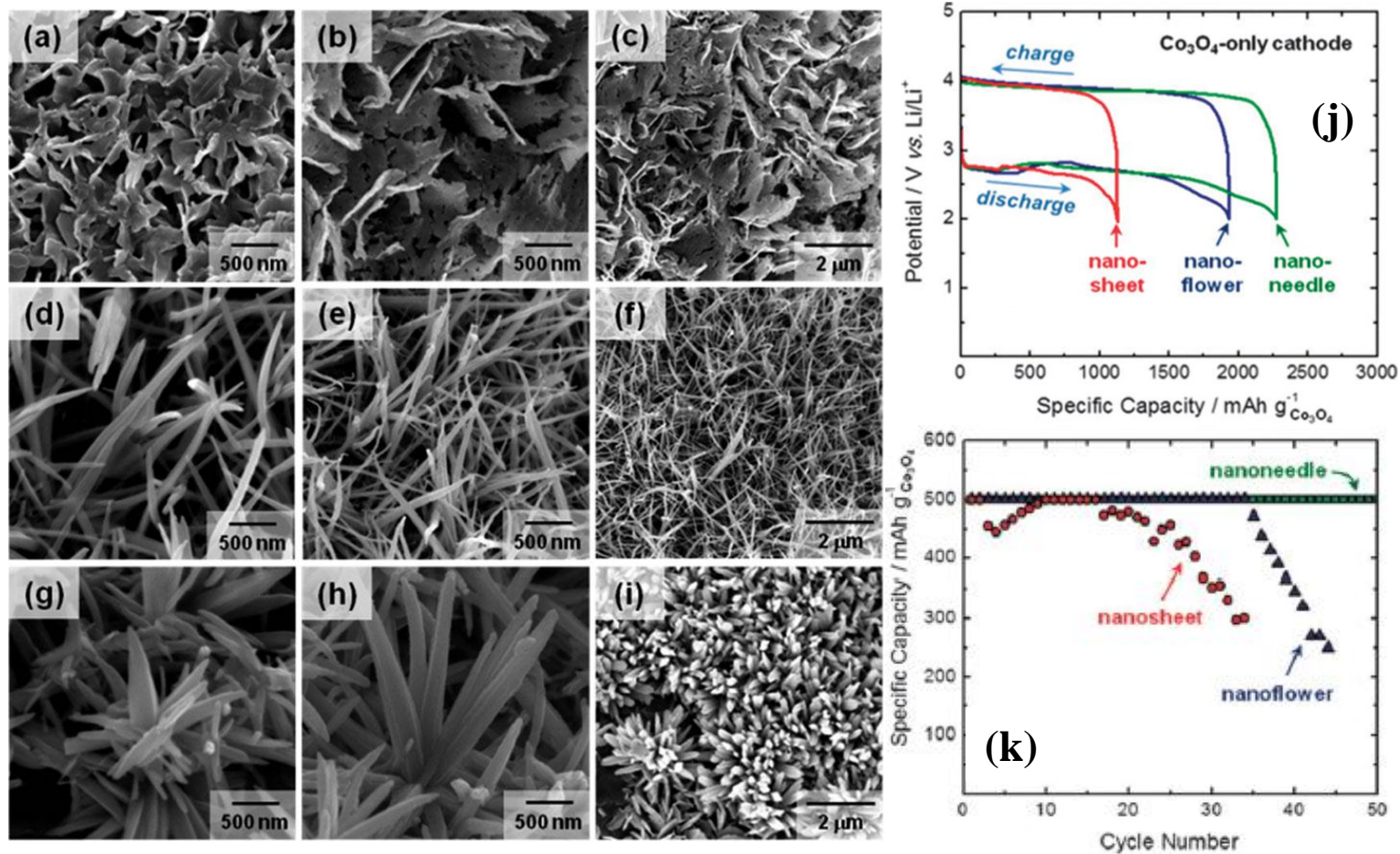


Fig. 20

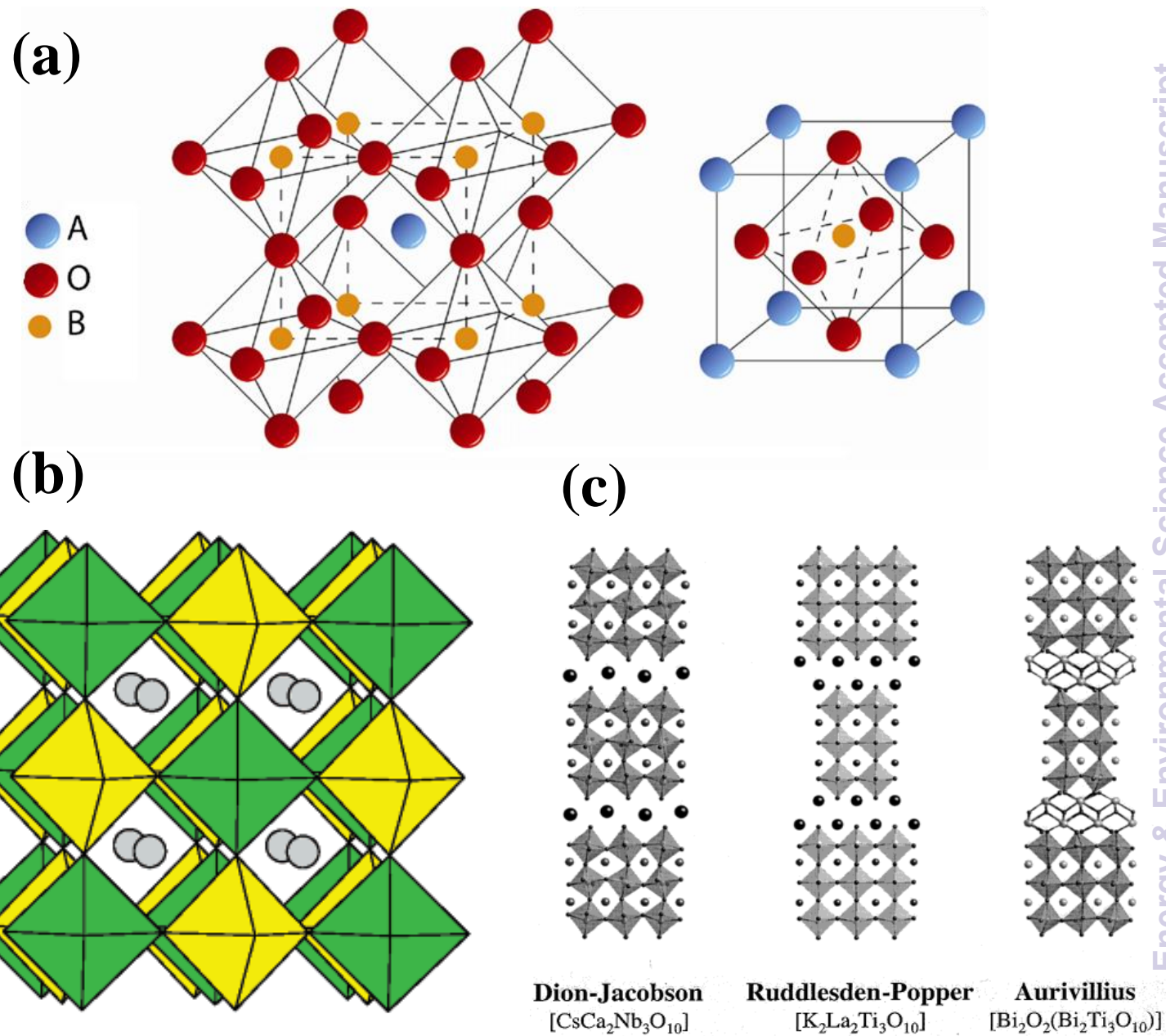


Fig. 21

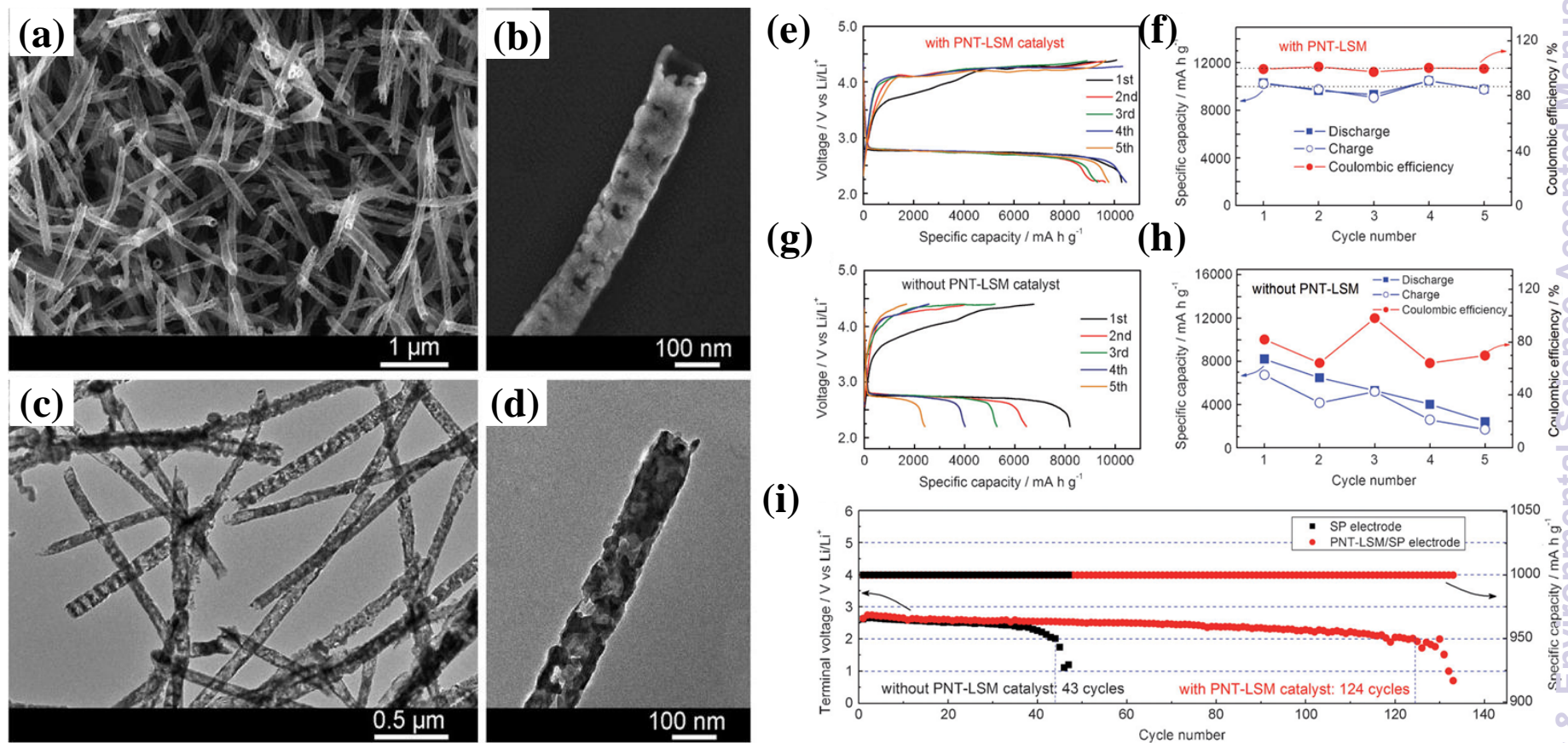


Fig. 22

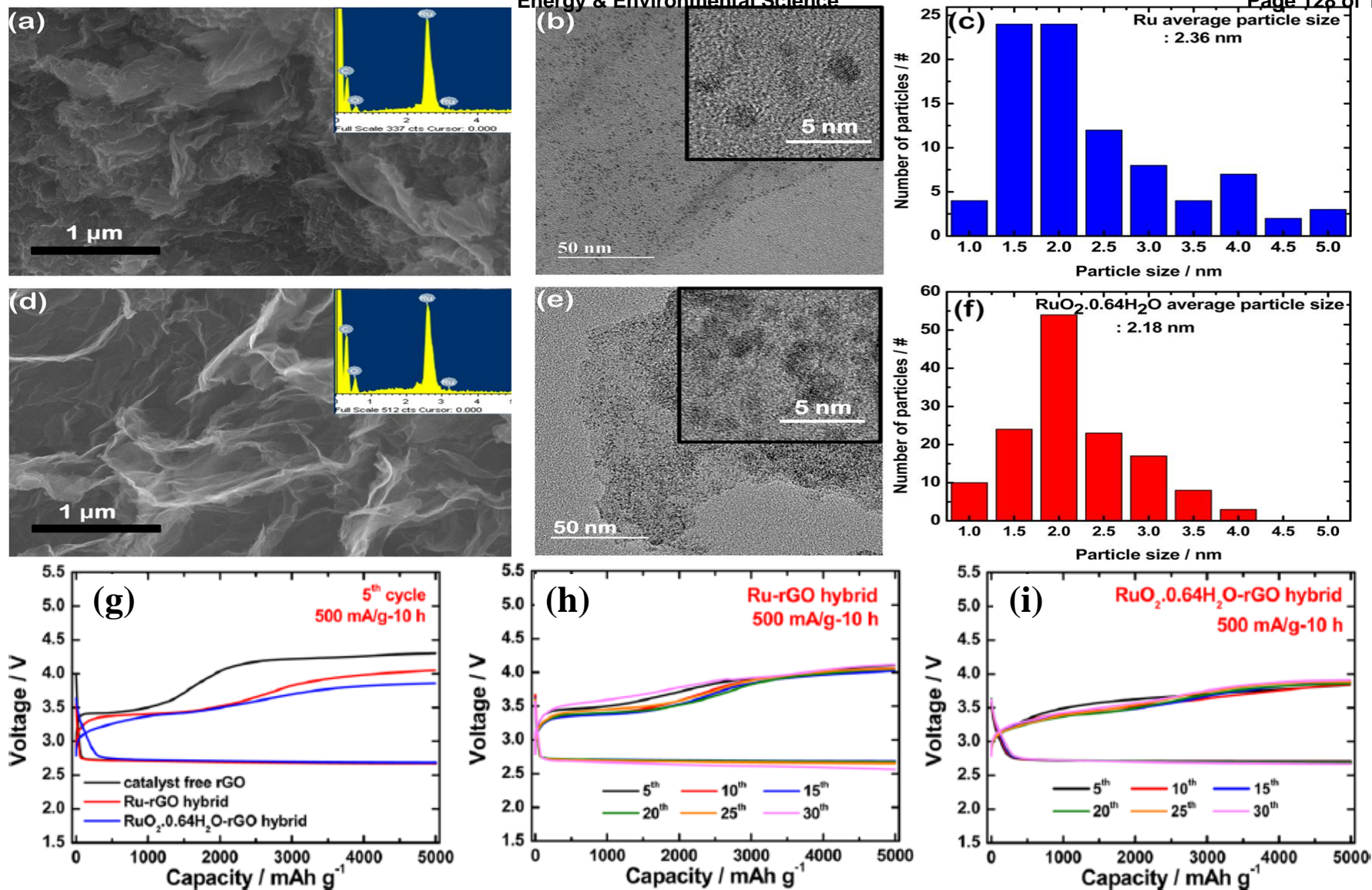


Fig. 23

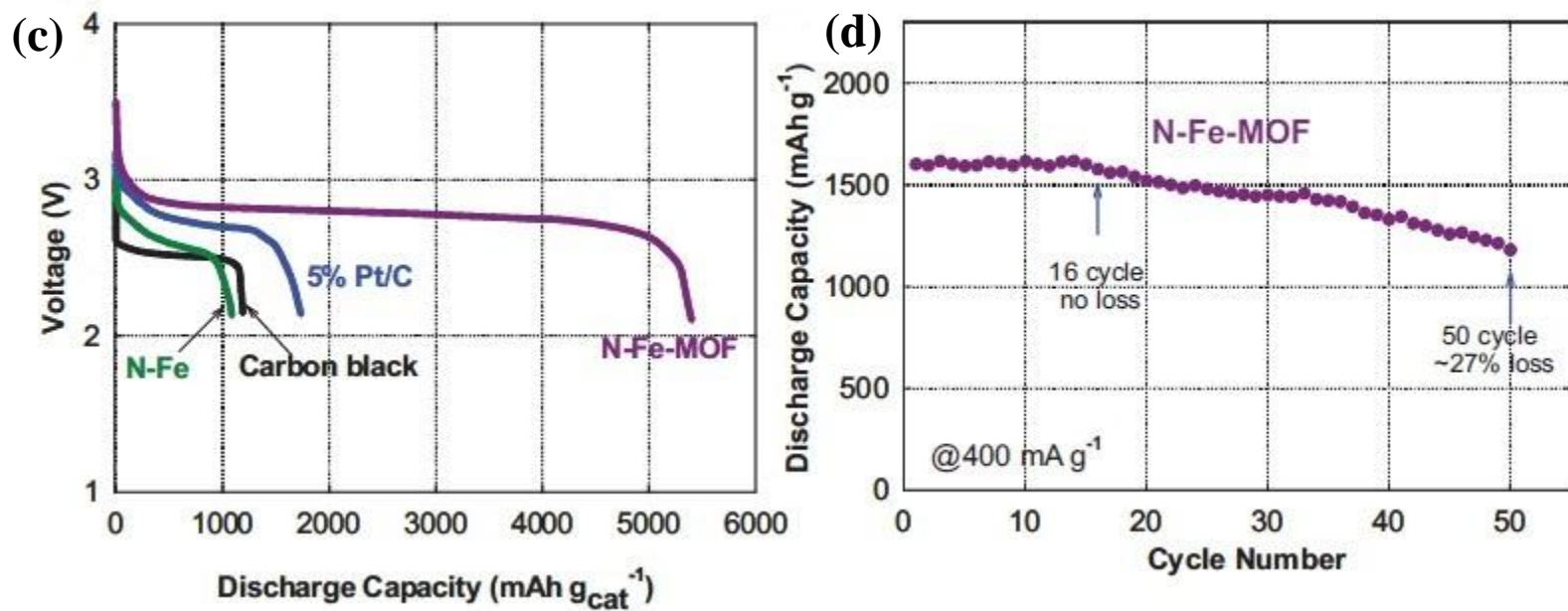
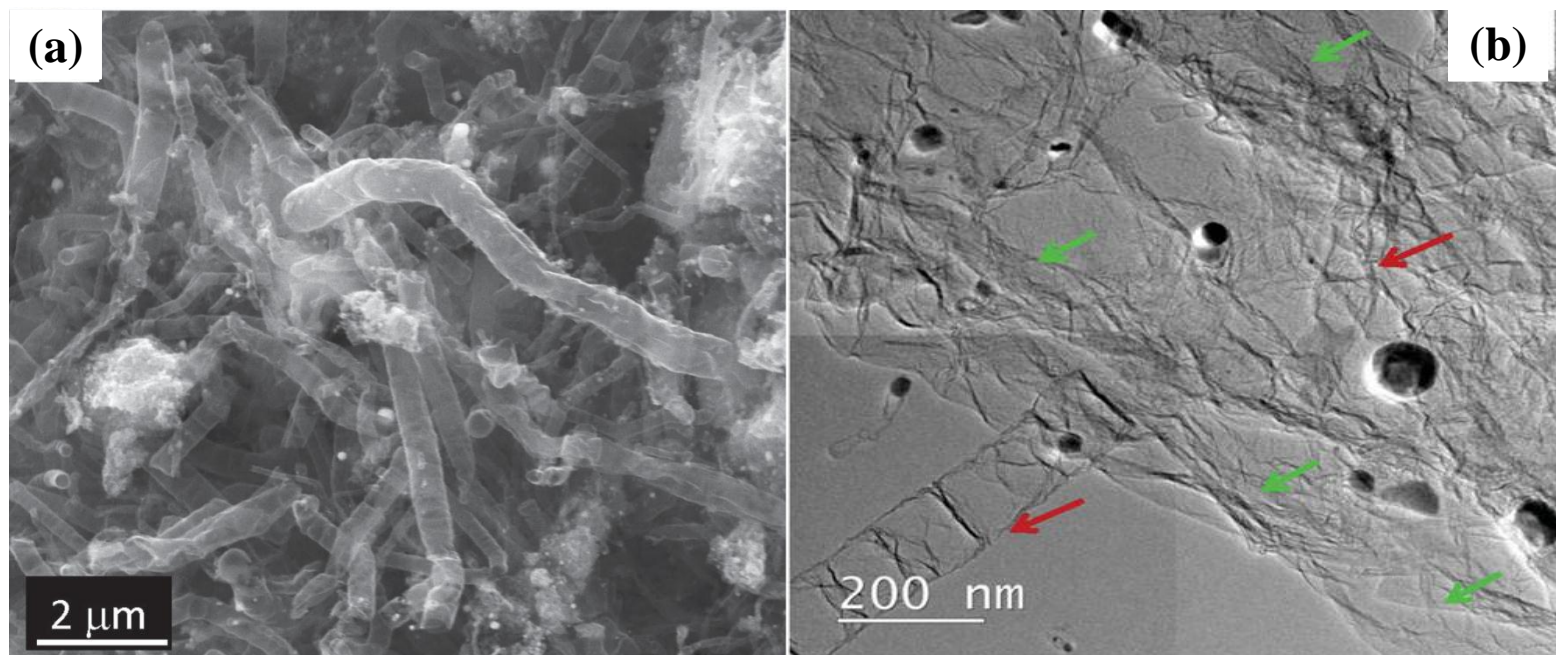


Fig. 24

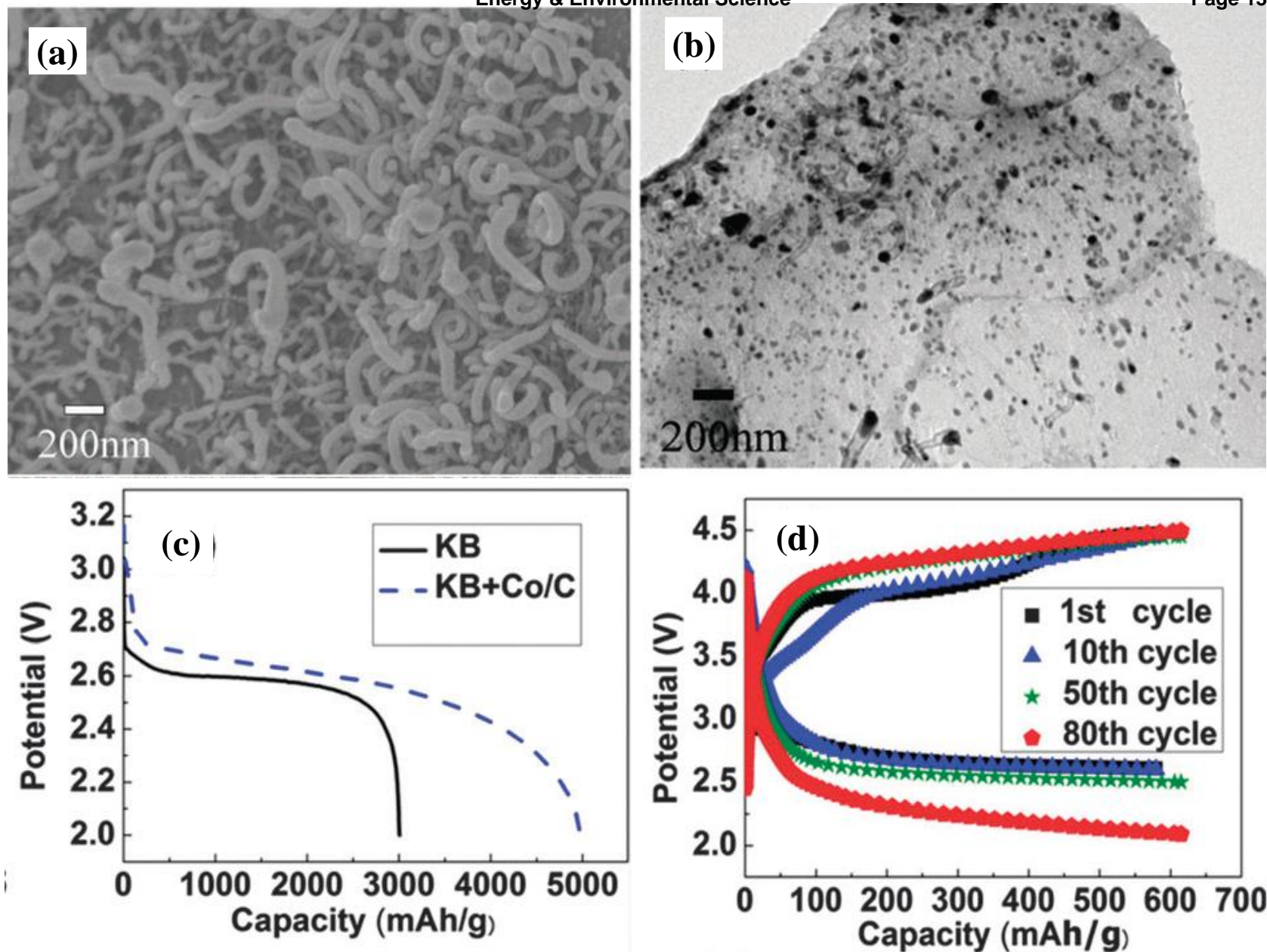


Fig. 25

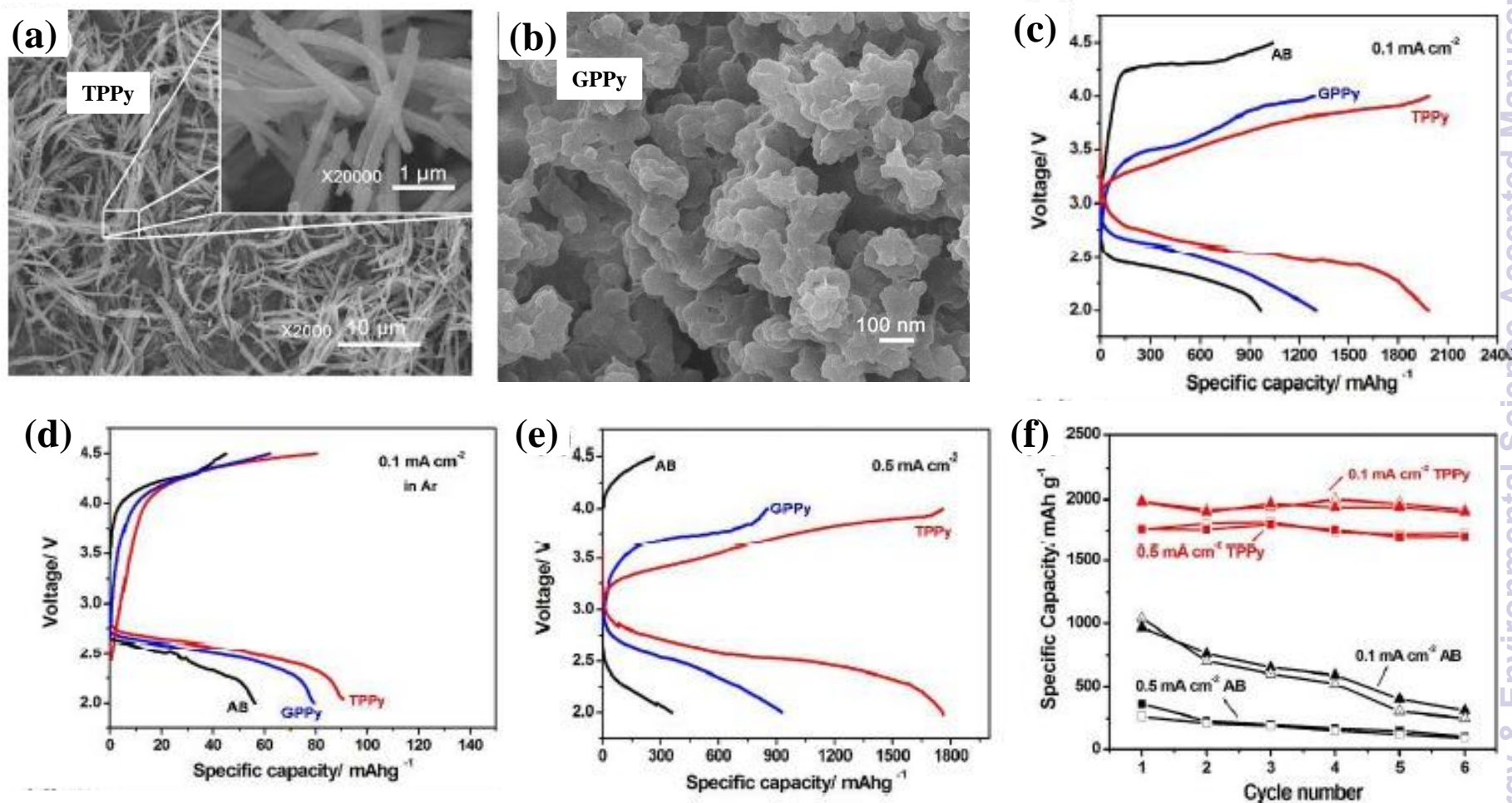


Fig. 26

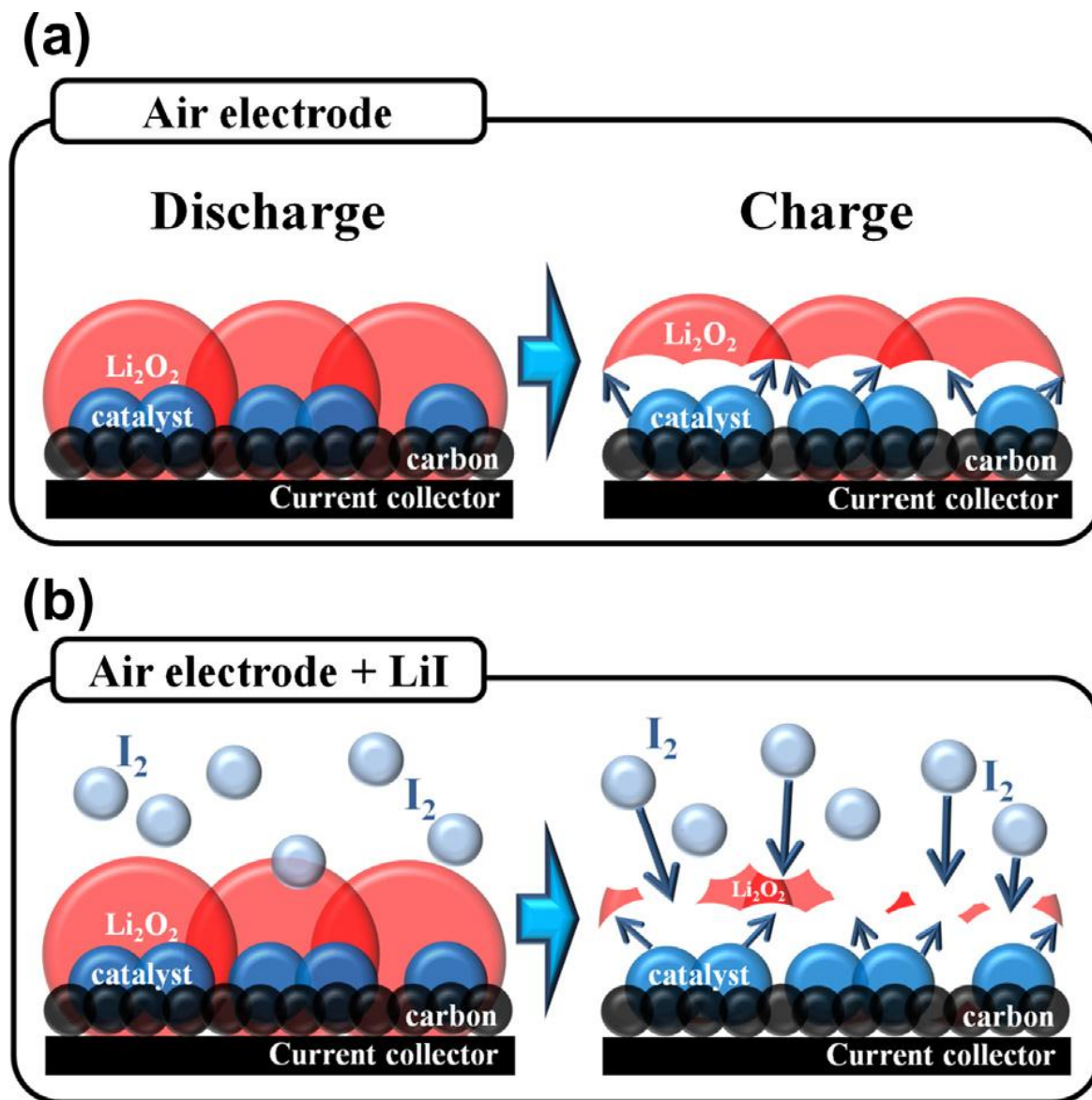
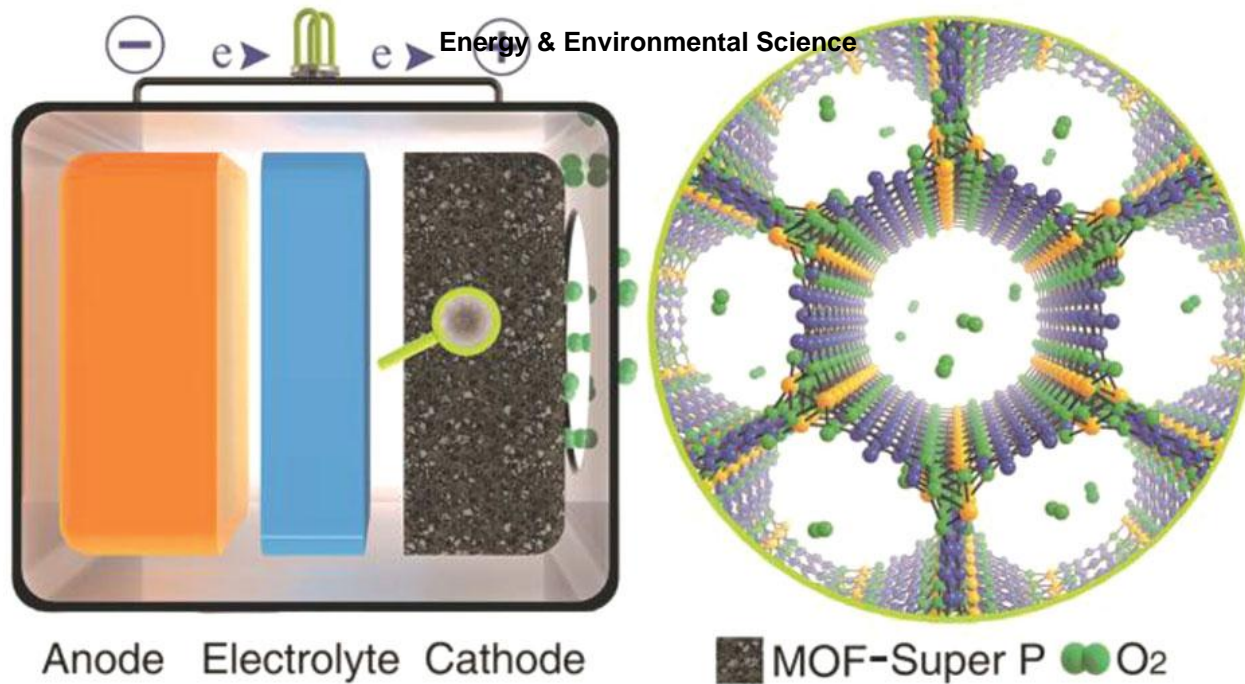


Fig. 27

a)



b)

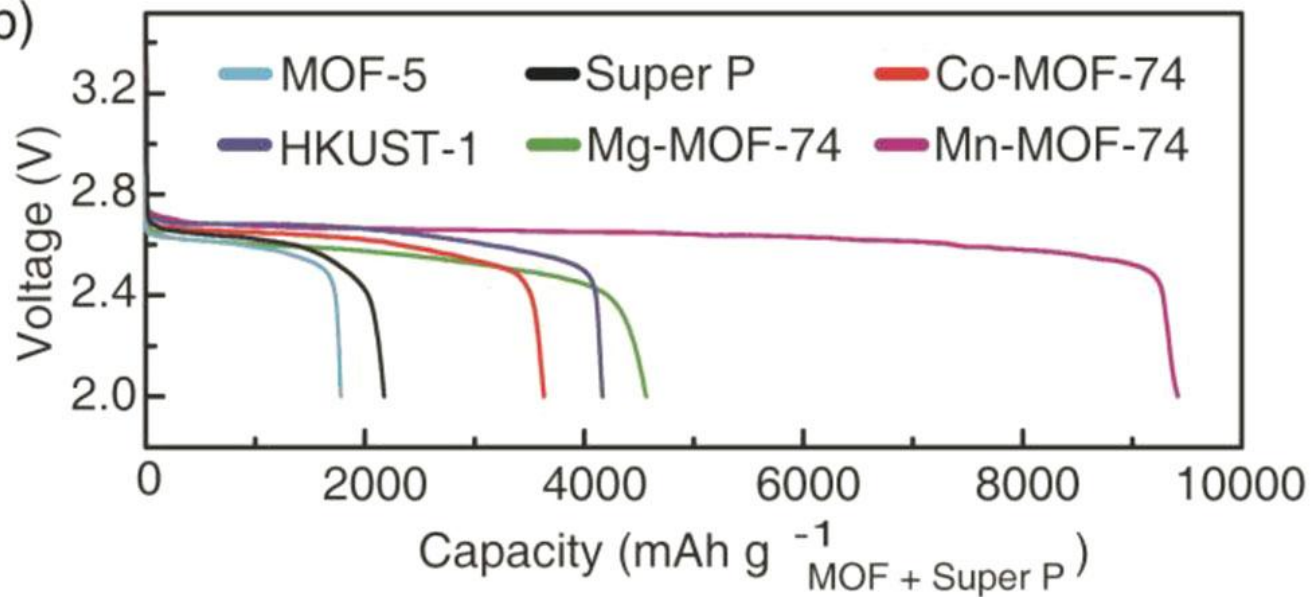


Fig. 28

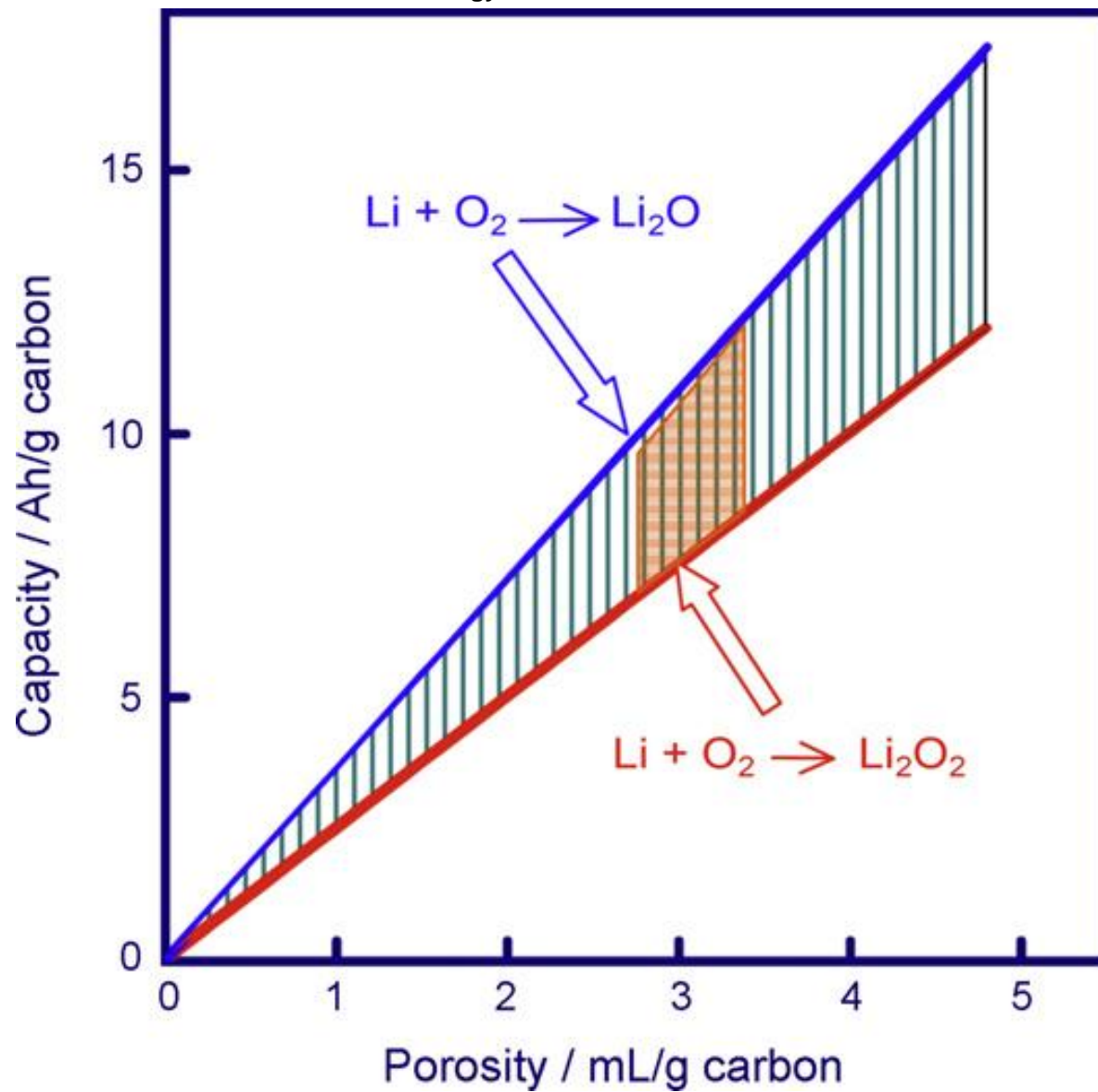


Fig. 29

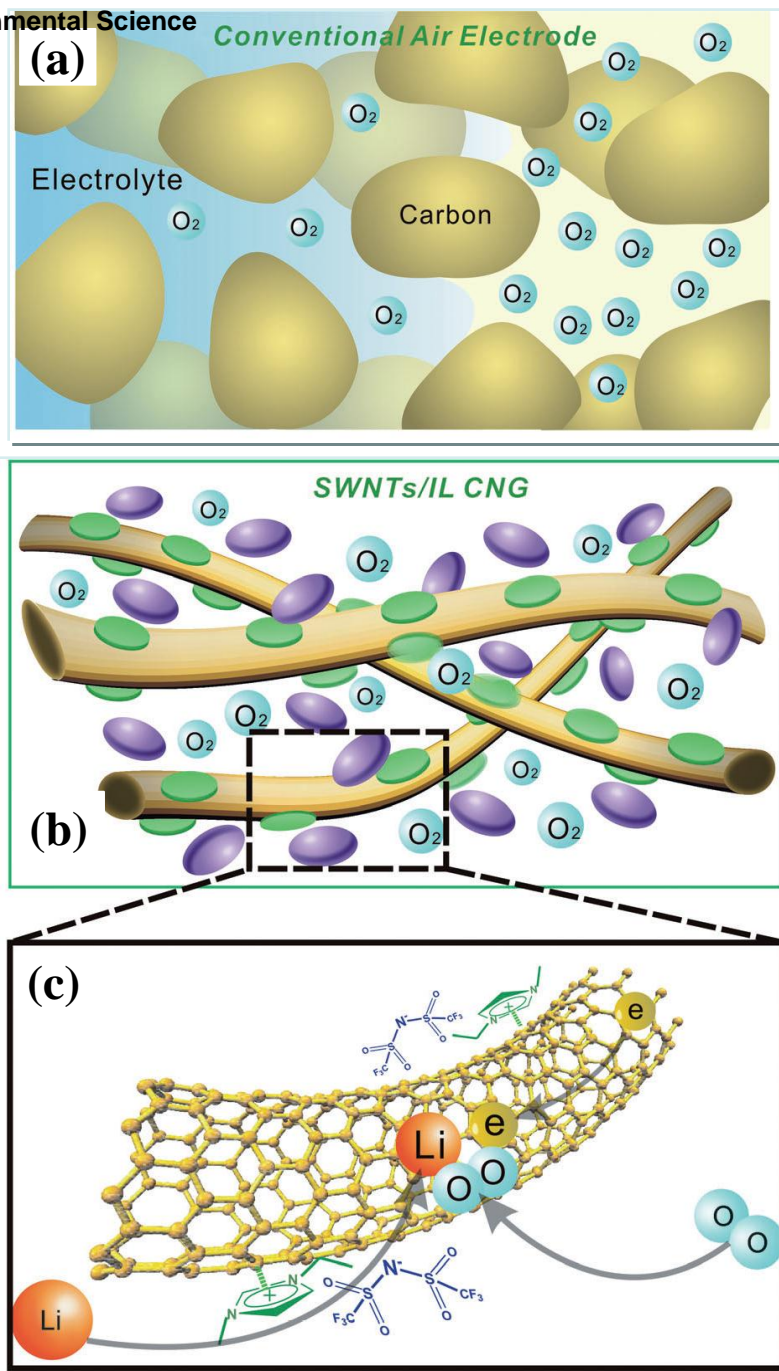


Fig. 30

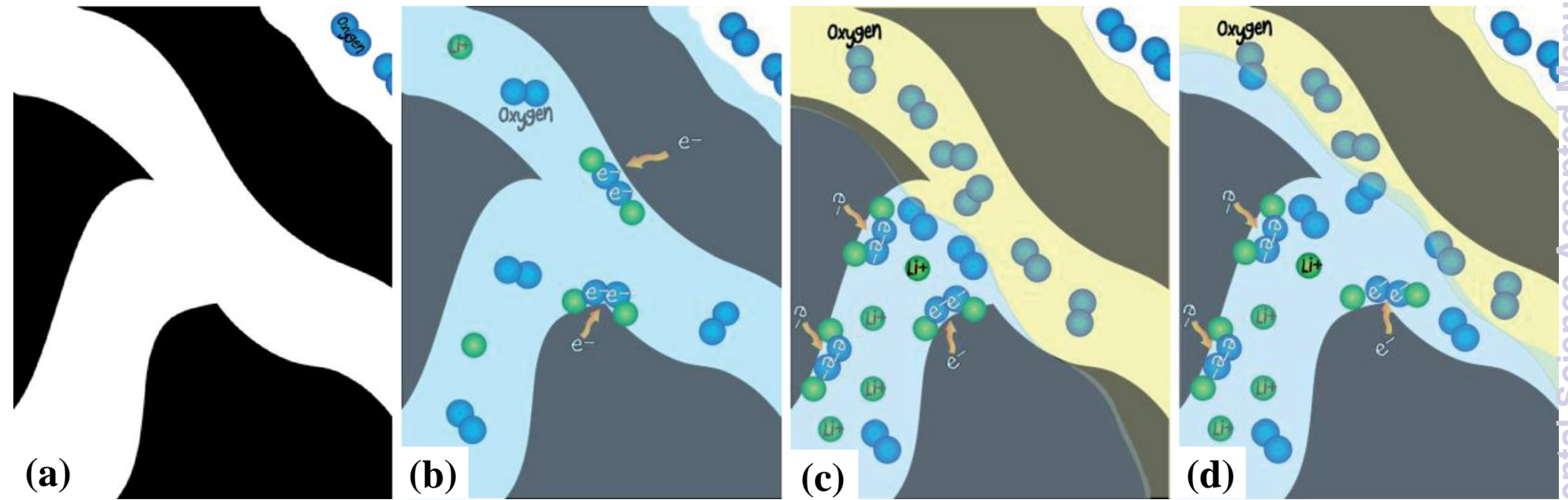
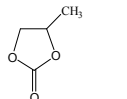
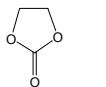
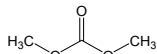
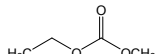
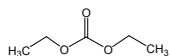
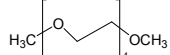
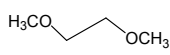
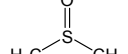
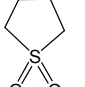
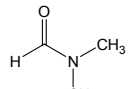
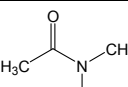


Fig. 31

Table 1 Physical properties of solvents mostly used in electrolyte for non-aqueous Li-air batteries

Solvent	Molecular weight	Structure	Dielectric Constant ϵ (25°C)	Dipole moment (μ)	Donor number (kcal mol ⁻¹)	Viscosity η (cP) (25 °C)	Oxygen solubility (mM cm ⁻³)	Boiling/melting point (°C)	Vapor pressure (kPa, 25°C)	Density (g cm ⁻³ , 25°C)
Carbonate	PC		64.92	4.94 (18°C)	15.1	2.53	3.2	241.7/-48.8	0.160 (55°C)	1.1951
	EC		89.78 (40°C)	4.87 (25°C)	16.4	1.930 (40°C)	1.71	248.2/36.4	3.371 (95.21°C)	1.3383
	DMC		3.107		17.2	0.59 (20°C)	7.29	91/4.6	2160	1.063
	EMC		2.958			0.65	7.95	110/-53	0.89	1.006
	DEC		2.820 (20°C)	0.90 (25°C)	16	0.748	7.92	126.8/-74.3	1.3 (23.8°C)	0.96926
Ether	TEGDME		7.79		16.6	4.05	4.43	275/-30	<1.33	1.009
	DME		7.2	1.71 (25°C)	20	0.455	9.57	84.5/-58	6.4 (20°C)	0.86370
Sulfone	DMSO		46.45	4.06 (25°C)	29.8	1.991	2.1	189/18	56	1.1
	TMS						1.59	285/28	1.33	1.261
Amide	DMF		36.71	3.24 (25°C)	26.6	0.802		153/-61	0.49	0.94387
	DMA		37.78	3.71 (30°C)	27.8	0.927		166.1/-20	0.17	0.93633 7

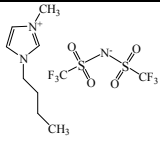
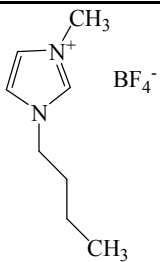
Ionic liquid	[C4mim][Ntf2]	419.36					44			/-1		1.429
	[C4mim][BF4]	226.02					92			/-71		1.26

Table 2 Reported capacities of commercial carbon materials in non-aqueous Li-air batteries

Carbon materials	Capacity(mAh g ⁻¹)/Current density(mA cm ⁻²)	Refs.
Super P	2120/0.05	84
	2825/0.05	85
	989/0.05, 528/0.2, 248/0.5	204
	>4000/0.02, 1400/0.05	341
	1800/0.1	133
	1736/0.1	175
	1000/0.1	214
	4254.7/0.1, 6587/0.15	334
	2300/0.1	345
	~1000/0.2	88
	400/0.2	90
	3400/70 mA g ⁻¹	308
	1500/100 mA g ⁻¹	347
KB EC600JD	2700/0.025	346
	850/0.05	336

	800/0.05	342
	1000/0.05	343
	5813/0.1 (1.9 mg carbon loading), 3378/0.1 (4 mg carbon loading), 404/0.1 (12.2 mg carbon loading)	28
	2600/0.1	214
	3374.4/0.1	334
	400/0.1	337
	800/0.2	90
	3000/0.2	340
	3214/30 mA g ⁻¹	289
Vulcan XC-72	1200/0.04	110
	762/0.1	175
	1705.7/0.1	334
	1645/0.1	339
	1053.8/75 mA g ⁻¹	350
Super S	1000/50	83
	850/70	95
Black Pearls 2000	50/0.05	336
	1909.1/75 mA g ⁻¹	350
KB EC300JD	2200/0.1	214
Graphite	560/0.1	19
	250/0.1	175
Darco G-60	210/0.05	150
	280/0.05	342
	170/0.05	343
	180/0.05	344
Norit carbon black	4400/70 mA g ⁻¹	308
Calgon activated black	80/0.05	336
Ensaco 250G	550/0.1	214
Chevron activated black	1410/0.1	19
Activated Carbon SY TC-03	2310.9/0.1	334
Activated carbon M-30	2120/0.05	91
Denka	750/0.1	214

	25/0.05	336
--	---------	-----

Table 3 Summary of the composition, size, phase properties, charge-discharge voltages and discharge capacities of the carbon-supported bimetallic gold-platinum nanoparticles with different alloyed phase structure. Reprinted from [ref. 418]

Catalyst	Treatment temp. (°C)	Particle size (nm)	Lattice parameter (a) extracted from XRD data (nm)	Comments	D _s charge			Charge V _{charge} (V _{Li})	Difference ΔV(V _c -V _d) (V)
					V _{onset} (V _{Li})	V _{discharge} (V _{Li})	Capacity (mAh g _{carbon} ⁻¹)		
C	—	—	—	—	2.7	2.6	1022	4.5	1.9
Pt/C	—	2-3	a(Pt)=0.392	(E-tek catalyst)	2.7	2.5	605	3.9	1.4
Au ₂₂ Pt ₇₈ /C(a)	300	4.2±0.4	a(AuPt)=0.397	Partial alloy	2.8	2.7	1104	4.0	1.3
Au ₂₂ Pt ₇₈ /C(b)	500	5.6±0.8	a(AuPt)=0.397	Alloy	2.8	2.7	1093	3.9	1.2
Au ₂₂ Pt ₇₈ /C(c)	700	6.5±1.0	a(Au)=0.406 a(AuPt)=0.396	Au-rich shell, alloy core	2.7	2.4	630	4.4	2.0
Au ₄₉ Pt ₅₁ /C	400	4.5±2.2	a(AuPt)=0.395	Alloy	2.8	2.7	1329	4.0	1.3
Au/C	280	3.7±0.6	a(Au)=0.408	—	2.6	2.4	1237	4.0	1.6

Table 4 Discharge capacity of cycles 1 and 5 based on various metal oxides. Reprinted from [ref. 193]

Catalyst	Capacity (mAh g ⁻¹)		Capacity retention per cycle (%)
	1 st cycle	5 th cycle	
MnO ₂	262	653	248
Co ₃ O ₄	199	304	152
NiO	298	362	121
Fe ₂ O ₃	264	285	108
CuO	292	658	225
V ₂ O ₅	216	829	383
MoO ₃	152	152	100
Y ₂ O ₃	238	213	89

1^a Electrolyte decomposition